TÉCNICO LISBOA

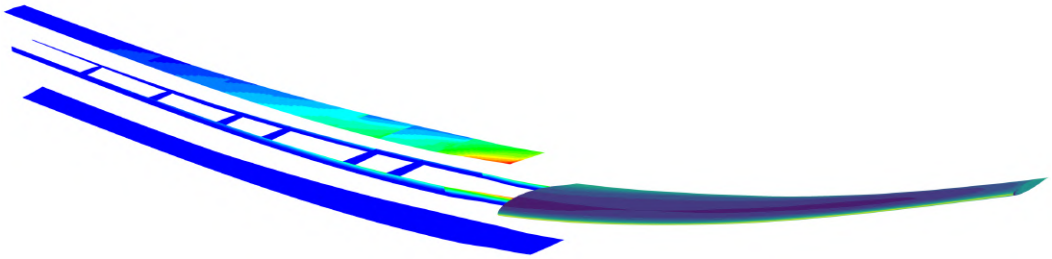

Aerostructural Design of a Medium-Altitude Medium-Endurance UAV Wing

Pedro Marques Cardoso

Thesis to obtain the Master of Science Degree in

Aerospace Engineering

Supervisors: Prof. André Calado Marta
Eng. Nuno Miguel Bento de Matos

Examination Committee

Chairperson: Prof. Filipe Szolnoky Ramos Pinto Cunha
Supervisor: Prof. André Calado Marta
Member of the Committee: Prof. José Manuel Da Silva Chaves Ribeiro Pereira

December 2024

Dedicated to my parents

Declaration

I declare that this document is an original work of my own authorship and that it fulfills all the requirements of the Code of Conduct and Good Practices of the Universidade de Lisboa.

Acknowledgments

I would like to express my sincere gratitude to my supervisors, Professor Andre Marta and Eng. Nuno Matos. I am grateful to Professor Andre Marta for his invaluable guidance, constant availability, and unwavering patience throughout this project. I also thank Eng. Nuno Matos for his support and the significant time he dedicated to assisting me with various challenges along the way.

I would also like to convey my gratitude to TEKEVER UAS for the opportunity to undertake this work, their funding and for all the necessary feedback.

I would also like to thank the MDO Lab at the University of Michigan for providing access to all the MACH-Aero framework tools employed in this work, with special mention to Professor Joaquim Martins and Dr. Eirikur Jonsson.

I am incredibly grateful for the unconditional support and encouragement from my parents. Without their efforts, I would not have been able to complete this degree. I also want to give a special thanks to my brother for his unwavering support and confidence in me.

Finally, I would like to recognize the institutions and all those who have been a part of my academic journey. Their support has deepened my knowledge and understanding throughout my college experience. I am especially grateful to the professors and friends I made along the way for their essential collaboration.

Resumo

Num mercado competitivo, os fabricantes concorrem no desempenho dos UAV através de tecnologias de design avançadas. Este estudo maximiza o alcance, através da otimização de uma asa com a ferramenta aeroestrutural de alta fidelidade baseada em gradiente, MACH-Aero. O processo otimiza variáveis aerodinâmico-estruturais como ângulo de ataque, torção, corda, perfil alar, envergadura, espessura e orientação da fibra do compósito, usando o método adjunto para cálculo de derivadas. Os ótimos unidisciplinares estabelecem referencias para o problema aeroestrutural. O impacto dos modelos geométricos de maior fidelidade foi examinado através da análise de asa simplificada, detalhada e grupo asa-fuselagem, revelando ainda aspectos perdidos em análises unidisciplinares, incluindo o impacto da torção estrutural na resposta aerodinâmica. As restrições de fabricação em compósitos multicamadas, a adjacência e a ortogonalidade das camadas, tiveram impacto mínimo. No entanto, a restrição de deformação da asa afetou significativamente o perfil alar e o projeto final. A resposta da asa otimizada em velocidade de mergulho mostrou resultados aeroelásticos promissores. A comparação das otimizações aeroestruturais/disciplina única destacou a intensidade computacional do primeiro mas resultados superiores, incluindo o alcance estendido conseguido pelo redistribuição de espessura estrutural e sustentação. A abordagem simultânea das disciplinas oferece informações valiosas sobre as compensações entre as mesmas. Em comparação com a asa inicial o caso ideal mostrou um aumento de 4,2% no alcance crescendo a eficiência aerodinâmica 10,4% e reduzindo a massa 43,9%, até 9,9% de aumento no alcance se a envergadura fosse uma variável, de mais 32% na eficiência aerodinâmica, apesar de mais 114% no peso da asa.

Palavras-chave: otimização multidisciplinar, interação fluido-estrutura, projeto de aeronaves, método adjunto, deformação de forma livre, materiais compósitos

Abstract

In a competitive market, manufacturers strive to enhance UAV performance through advanced design technologies. This study focuses on maximizing UAV range by optimaly designing the wing with the aerostructural, gradient-based framework, MACH-Aero, integrating high-fidelity computational models. The process optimizes aerodynamic and structural variables like chord, airfoil, span, panel thickness and composite fiber orientation, using the discrete adjoint method for efficient derivative computation. Single-discipline optima were studied to establish a baseline for the aerostructural problem. The impact of higher-fidelity geometry wing models was examined through aerostructural analysis of a simplified wing, a detailed wing, and a wing-fuselage group, revealing aspects missed in single-discipline analyses, including the impact of structural twist in the aerodynamic response. Manufacturing constraints in multilayer composites, including neighboring ply angle adjacency and orthogonality, had minimal impact. However, the tip maximum displacement constraint affected significantly the aerodynamic airfoil variable and final designs. Exploring the response at dive speed for a more flexible wing showed promising results. Comparing aerostructural and single-discipline optimizations, highlighted the computational intensity of the former but superior design outcomes, including extended range achieved by root-heavy and tip-light thickness, and lift distribution. Addressing both aerodynamic and structural disciplines concurrently offers valuable insights into trade-offs among design variables. Compered to baseline wing design final optimal showed from 4.2% increase in range with a 10.4% gain in aerodynamic efficiency and 43.9% reduction in mass, up to 9.9% increase in range if span was a variable, with a 32% improvement in aerodynamic efficiency, despite a 114% increase in wing weight.

Keywords: multidisciplinary optimization, fluid-structure interaction, wing design, adjoint method, free-form deformation, composite materials

Contents

List of Tables

List of Figures

Nomenclature

Greek symbols

α	Angle of attack
γ	Twist angle
Γ	Dihedral angle
ε	Strain
η	Engine efficiency
θ	Ply angle
λ	Adjoint variable
Λ	Sweep angle
μ	Molecular viscosity
ρ	Density
σ	Stress
τ	Viscous shear stress
ν	Poisson's ratio

Roman symbols

a	Sound speed
b	Wingspan
c	Chord
C_D	Drag coefficient
C_f	Friction coeficient
C_L	Lift coefficient
D	Drag

E	Young's modulus
E_t	Total energy
f	Force
G	Shear modulus
g	Gravitational force
H	Enthalpy
h	Altitude
I	Unit
J	Generic function of interest
L	Lift
M	Mach
p	Pressure
q	Heat addition
R	Residuals
r	Vector of minimum distance
R	Range
Δs	Aerodynamic mesh first layer size
S	Wing area
S_A	Aerodynamic surface
sfc	Specific fuel consumption
t	Thickness
t	Time
u	Displacement field
u_A	Aerodynamic displacement
u_r	Structural rotation
u_t	Structural displacement
V	Volume fraction
v	Velocity

W	Work
w_0	Initial weight
w_f	Final weight
w_i	Weight coeficient
x	Design variables
x_0	Global design variables
x_i	Cartesian coordinate system
x_{sA}	State aerodynamic variables
x_{sS}	State structural variables
y_{1-3}	Global siystem response

Subscripts

A	Aerodynamic
f	Fiber
fric	Friction
∞	Free-stream condition
i, j, k	Local components
m	Matrix
proj	Projected
r	Rotations
ref	Reference condition
S	Structural

Glossary

3D	Three-dimensional
AAO	ALL-At-Once
ANK	Approximate Newton Krylov
CAD	Computer Aided Design
CAGR	Compound Annual Growth Rate
CFD	Computational Fluid Dynamics
CFRP	Carbon Fiber Reinforced Polymer
CGNS	CFD General Notation System
CPU	Centra Processing Unit
CSM	Computational Structural Mechanics
DoF	Degrees of Freedom
DV	Design variable
FEM	Finite Element Method
FFD	Free-Form Deformation
IDF	Individual Discipline Feasible
IDW	Inverse Distance Weighting
IGES	International Graphics Exchange Standards
IHC	Implicit Hole Cutting
JST	Jameson Schmidt Turkel
KS	Kreisselmeier-Steinhauser
MAME	Medium Altitude Medium Endurance
MDA	Multidisciplinary Analysis
MDF	Multidisciplinary Feasible
MDO	Multidisciplinary Design Optimization
MTOW	Maximum Take-Off Weight
PDE	Partial differential equation
RANS	Reynolds-Averaged Navier-Stokes
REF	Reference
RLT	Rigid Link Transfer
SA	Spalart-Allmaras turbulence model

SAND Simultaneous Analysis and Design

SLSQP Sequential Least Squares Programming Algorithm

SST Mentrt Shear Stress Transport turbulence model

TACS Toolkit for the Analysis of Composite Structures

UAV Unmanned Aerial Vehicle

XDSM Extended Design Structure Matrix

Chapter 1

Introduction

This chapter introduces the motivation behind studying Unmanned Aerial Vehicles (UAVs), highlighting their historical development and high number of applications. The UAV industry's substantial growth and market projections are showcased, underlining the need for more efficient UAVs. The focus of the work on developing an aerostructural optimization framework for the TEKEVER AR5 is introduced. The chapter concludes with a brief overview of the project's background, objectives, deliverables, and document outline.

1.1 Motivation

The fixed-wing UAVs, as we know then today, were primarily developed during the 20^{th} century for military purposes, being part of most military forces nowadays. In opposition, civilian applications have experienced slower growth due to the limitation imposed by high costs, which are not a major concern in the military sector as the focus is less on the final price and more on achieving the desired results [1]. Nevertheless, the diversity of models due to a vast realm of mission requirements [2] has created an extensive civil market, whose applications include:

- Environmental monitoring: UAVs have been used as platforms to access data concerning meteorology, the state of ecosystems, or geological phenomena. For example, During a volcanic eruption on the island of Fogo, in Cape Verde, the TEKEVER company used small drones to capture images in high definition and with thermal imaging cameras [2];
- Search, Rescue, and Surveillance: Drones can quickly cover large areas to search for missing persons or vessels;
- Wildfire combat: The use of UAVs to monitor and extinguish wildfires is a remarkable step in this front as abilities the monitor and extinguish fire without risking human life [3];
- Medical services: Some UAVs are used in remote places to ensure a steady supply chain when the basic infrastructure is lacking and traditional transport methods are not efficient. They can be also used when the time aspect of the mission is critical like in organ or blood transport [4];

- Agriculture: UAVs are used to pulverize chemicals to aid in the growth of crops. They can also be used for inspection in precision farming [5];

- Delivery of goods, aerial photography, maritime monitoring, and civil infrastructure inspection [3, 6].

After exploring the diverse civilian applications of Unmanned Aerial Vehicles, the subsequent focus will be on elucidating key economic aspects within this market. In 2023, the drone market was estimated at US$ 34 billion [7] with a projected growth rate from 8.3 to 17.2% Compound Annual Growth Rate (CAGR) [8, 9]. From [7], the fixed-wing market corresponds to 21% of the total drone market at the end of 2022. Moreover, the fixed wing market was evaluated in US$ 7.085 billion in 2023 with a forecast of a growth of 17.2% CAGR in contrast to the historical market value of 15.4%. All the reports mentioned were made considering historical data until 2022-2023 and aimed to forecast this market until 2030-2033.

The overall market characteristics of the fixed-wing UAV by region and type are presented in Figure 1.1. It is interesting to remark that the majority of the market is dedicated to the military sector despite the civilian and commercial already accounting for a third of the total. Finally, it is important to notice that geographically the UAV market is most developed in Europe and North America.

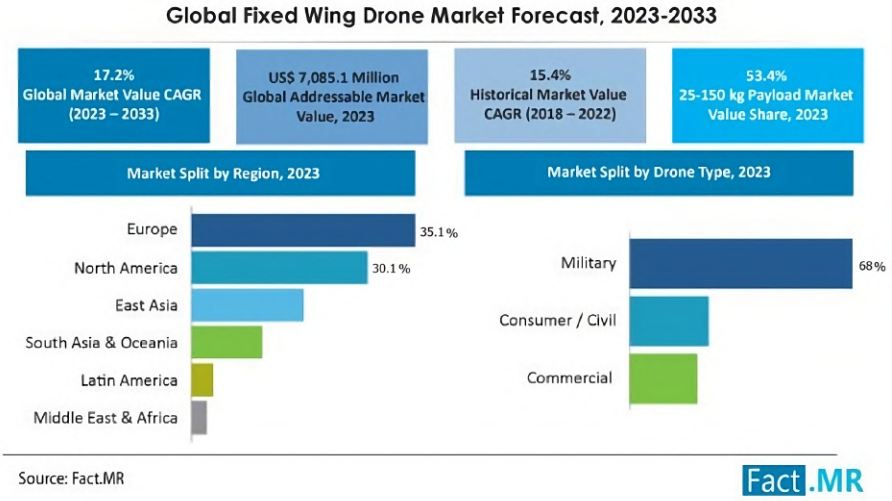

Figure 1.1: Distribution of the UAV fixed-wing market by region and type [7].

Consequently, a vast number of companies are investing in this market and the competition among them is fierce. Therefore, there is the need to develop more efficient UAVs to surpass the capability of today's UAV industry in the sense of fulfilling new mission requirements and contributing to the market value of the company that designed it and supplied [10]. In that sense, the purpose of this work is to assist on the development of a next generation TEKEVER AR5 (Figure 1.2) model by using a high-fidelity aerostrutural design tool. The goal is to re-design the main wing to achieve better aerodynamic and structural performance such that the model increases its value proposition in the current fixed-wing Medium-Altitude Medium-Endurance (MAME).

1.2 Project Overview

This project is a collaboration with the industry that aims to develop a framework to aid in the design of future UAVs. In that regard, this work will serve as a basis for the aerostructural design of a wing. This approach will be applied to the current TEKEVER AR5 UAS platform (Figure 1.2), a system currently on the market, as a first application basis, being expected to be applied in the next new platforms as well.

Figure 1.2: TEKEVER AR5 [11].

The TEKEVER AR5 is an advanced medium-altitude, medium-endurance fixed-wing UAV that can perform multiple missions such as search and rescue, maritime surveillance, and maritime patrol, benefiting from reasonable endurance, and reduced operating costs [11]. Table 1.1 contains the basic characteristics of the TEKEVER AR5.

Table 1.1: Basic characteristics of the TEKEVER AR5 [11].

Cruise speed	100 km/h
Cruise altitude	305 m
Payload	50 kg
Wing span	7.3 m
Wing area	2.17 m^2
Length	4 m
Endurance	20 h
Comms range	Unlimited
Recovery and lunch	Unprepared airstrip

Therefore, this work intendes to develop the coupled optimization, integrating the aerodynamic and structural aspects of the design. Further, it builds on previous work focused on the aerodynamic [12] where a framework for the aerodynamic optimization and analysis was made, encompassing work that will not be renovated here, namely, code validation with experimental data and mesh studies analysis where promising results were achieved. Figure 1.3 represents the last step of the mentioned work [12], the aerodynamic analysis incorporating the optimized wing with the fuselage.

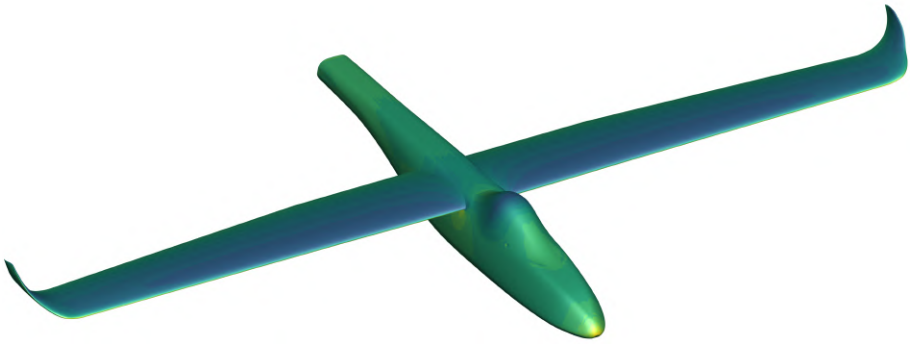

Figure 1.3: CFD analysis of the TEKEVER AR5 [12].

Additionally, the framework to perform the wing structural optimization was also developed [13]. Once again, following validation of the code and the mesh analysis already done, auspicious results were found for the TEKEVER AR5 wing. Figure 1.4 represents the wing structure of the mentioned work [13].

Figure 1.4: Structural representation of the TEKEVER AR5 [13].

To achieve the objective of coupling the aerodynamic and structural disciplines, the open-source software MACH-Aero developed by the Multidisciplinary Design Optimization (MDO) Laboratory of the University of Michigan will be used [14], following the usage of ADFlow in [12] and in [13].

1.3 Objectives and Deliverables

The objective of this work is to work on a framework capable of performing a high fidelity couple aerostructural composite wing design for a new MAME Fixed wing UAV. The framework will be implemented on the open-source optimization software MACH-Aero produced by MDO Laboratory of the University of Michigan. In MACH, the Computational Fluid Dynamic (CFD) solver is the TACS and the Computational Structural Mechanics (CSM) solver is the .

The main milestones are depicted in Figure 1.5. Initially, literature review about aircraft optimal design and iteration fluid-structure interaction will be made. Then, the frameworks developed in previous works will be used to validate their ease of use and to get acquired with the solver, the pre- and post-processing tools, documenting the main point and presenting knew interesting cases, namely, winglet optimization. This will also allow to obtain the aerodynamic and structural baseline of the current TEKEVER AR5.

A demonstration of the aerostructural application using the simplified TEKEVER AR5 wing will determine the best overall options in terms of structural constraint and aerodynamic design variables. Finally, based on the tested coupled optimization framework, promising solutions for different operating conditions of the TEKVER AR5 will be found.

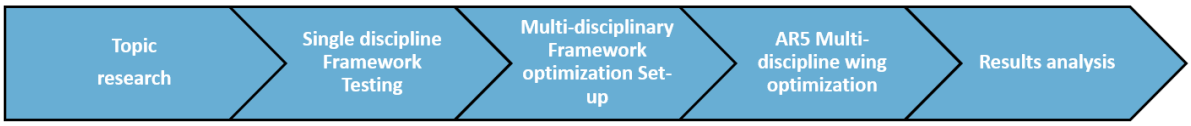

Figure 1.5: Milestones of this work.

1.4 Thesis Outline

This thesis is structured in the following way: Chapter 2 provides an overview of the aircraft design process, optimal design methodologies, and the integration of multidisciplinary optimization for efficient aerostructural design. It discusses the selection of an optimization algorithm and elucidating the application of a multidisciplinary approach.

Chapter 3 describes the aerodynamic model. It will encompass the theoretical foundation and the implementation of the Computational Fluid Dynamics model. To illustrate the capabilities of the analysis and optimization software, a case off the full TEKEVER AR5 wing is included and also explored the solely optimization of the winglet to understand its impact.

Chapter 4 provides an overview of structural analysis. It includes the theoretical foundation and the implementation of the structural analysis FEM model Finite-Element Model (FEM). Moreover, it also showcases the capabilities of the optimization software, including a case is of solely structural optimization.

Chapter 5 discusses the theoretical coupling between the two aerodynamic and structural models presented and the main implementation options to realize the aerostructural analysis. Moreover, the impact of doing an coupled aerostructural analysis itself and not the separate analysis is studied. Furthermore, the impact of manufacturing structural constraints on the optimization is evaluated, as well as of the inclusion of additional aerodynamic design variable.

Chapter 6 presents the main conclusions of the thesis and the main challenges found. Moreover, suggestions for future work is also present.

Chapter 2

Multidisciplinary Aircraft Design

This chapter provides an overview of the aircraft design process, optimal design methodologies, and the integration of multidisciplinary optimization for efficient aerostructural design. It covers the selection of the optimization algorithm and explains the application of the multidisciplinary approach.

2.1 Aircraft Design Process

Every project starts with the design phase. For a UAV, as a system with a high degree of complexity, an iterative process is, often, necessary to achieve an acceptable baseline agreement among requirements, initial concept, and sizing [15]. Prior design trade studies establish the requirements, and concepts are then formulated to fulfill these necessities. Design analyses often uncovers novel concepts and technologies, which can initiate an entirely new design endeavored [15]. The design phases of a new UAV can be divided into:

- **Conceptual Design:** Addresses fundamental questions concerning configuration, arrangement, size, weight, and performance. Conceptual design is a highly dynamic process, with new ideas and challenges emerging as the design is explored in greater depth. With each iteration of analysis and sizing, the design must be updated to incorporate the evolving concept changes;

- **Preliminary Design:** In this phase of the design, the UAV still suffers conceptual changes and the configuration still undergoes minor revisions. Eventually, minor changes are halted and the configuration is frozen. Specialists in various fields like structures, aerodynamics, and control systems work on their respective aircraft components. Testing begins in such areas;

- **Detail Design:** In this phase, the final design of each part and its production planning are developed. Final testing of the entire system is carried out.

As a new aircraft is designed using traditional or optimal design, the same three steps are needed, but, the way they are performed may vary.

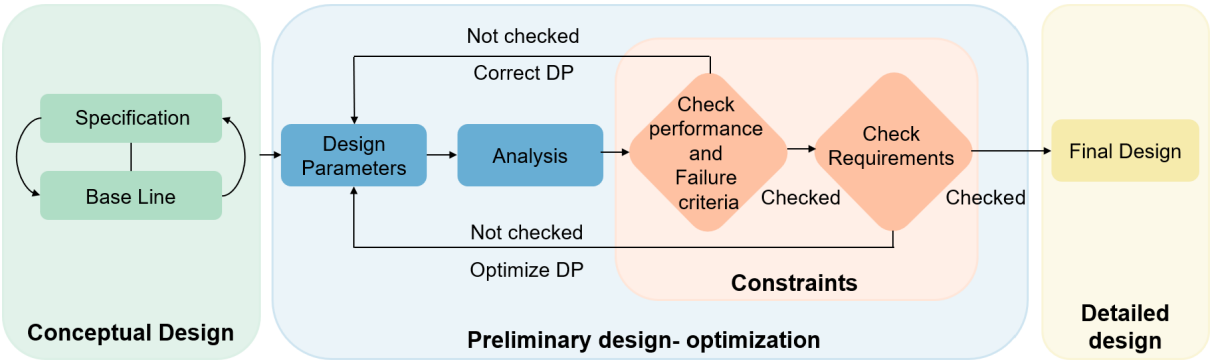

Figure 2.1: Aircraft design flowchart.

In this work, it will be used the optimal approach, which has been showcased in the literature as a good option for dealing with complex systems that require a large number of iterations to be designed [16]. This transition effectively shifts the burden of intricate knowledge requirements from individual disciplines to the optimization tool in phases such as conceptual and initial preliminary where the complexity is manageable. Nevertheless, it is important to emphasize that this shift does not entail a complete disregard for understanding from the human designer, as he plays a crucial role in preventing the optimizer from becoming a black box. Instead, this knowledge remains integral, facilitating a critical evaluation of the results and informed decision-making in the field of engineering [17].

In this project, high-fidelity numerical optimization is employed in the conceptual/preliminary design phase where its ability to consider multiple disciplines at once and find the best solution possible inside its limitations is desirable. The small decisions in the level of each variable are made following an optimizer algorithm and not based on experience as traditional methods, turning the process not subjected to parametric trade studies, an iterative procedure for which convergence is not guaranteed, nor sequential optimization, that could not lead to the sub-optimal of the system [18].

The process for both strategies is showcased in Figure 2.1 with the main difference being the automatic and algorithm nature in the optimization step strategy and the aggregation of the performance, failure criteria and requirements of the design in constraint that the optimizer needs to respect.

Therefore, this technique will be employed to perform the aerostructural design of the TEKEVER AR5 wing. This choice can also be supported by the numerous cases showcased in literature where optimization-based methods have been employed over the past decades. In the academic space, it is possible to find wing optimizations [19], where it was found that for any group subjected to constraints, there was a significant improvement of at least 7% reduction in drag, or turbomachinery applications as in an axial compressor [20]. In industrial applications, this technique can be found in such aircraft as the Boeing 787 Dreamliner [21], where it has been shown that substantial benefits could be realized by including many disciplines within a single Multidisciplinary Design Optimization (MDO) process, rather than optimizing each discipline in isolation, and the Airbus A350 [22].

2.2 Optimal Design

When considering an optimal design methodology, it is of utmost importance to properly define some basic parameters regarding the optimization problem and solution process to be implemented [18]:

- **Objective function**: is the benchmark that enables the comparison between all the designs. As such it must be possible to estimated numerically;
- **Design Variables (DV)**: are the variables that are allowed to change in the design process. Optimization is then the process of choosing the DV values that yield an optimum design. In optimization, the solution is confined to the design space defined by the DVs;
- **Constraints**: Design variables are subject to limitations known as bounds, which are straightforward to impose. Other linear or non-linear functions can be included as equality or inequality constraints. Feasible regions represent portions of the domain where all constraints are satisfied.

Types of Algorithms

To perform the optimization of a given function, an algorithm must be selected. Figure 2.2 showcases the possible types of algorithms.

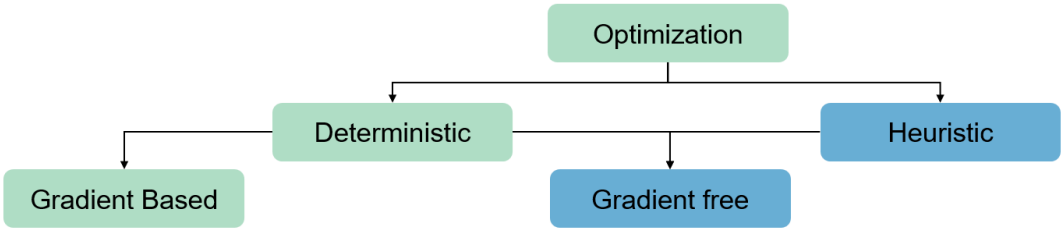

Figure 2.2: Optimization algorithms.

The algorithm used can be heuristic or deterministic. Heuristic algorithms are simple procedures meant to provide good solutions in hard optimization problems such as non-differentiable functions or constraints, discontinuous, discrete or non-linear search space, and for multiple local minima. An example of the use of this type of algorithm can be found in [23] where the particle swarm algorithm was used, since it was expected noise in the solution and the problem had discrete DV. However, these algorithms are computationally too expensive as their base of operation is random, requiring a very large number of iterations to converge with often no guarantee that will happen [18] and for that reason will not be employed in this work.

On the deterministic faction, the algorithms ca be gradient-based and gradient-free. The primary distinction between these two methods, as the name suggests, is the need for the computation of the derivatives and the complexity and relevant efficiency gains arriving from it.

Gradient-based optimizers excel in navigating local minima within large dimensional. They typically work by obeying an iterative two-step model where it first finds the optimal search direction and then the solution along that path for each iteration. This guarantees that minimal computational effort is

required as long as the constraint and objectives function are smooth and continuous in the domain of the problem. However, they struggle with discontinuous functions and can not hand discrete design variables or constraints. Besides that, they present a problem when dealing with solutions with multiple minima [18]. However, work around exist for this type of problems namely, starting from multiple points [24] and DV or constraints aggregation.

In this work, the algorithm used will be gradient-based since this type is very effective when dealing with many design variables [25, 26]. In Figure 2.3, a comparison between different types of algorithms can be found showcasing the effectiveness of the gradient based approach due to its computationally efficiency achieving rapid convergence rates with clear convergence criteria. This efficient is a requirement to do optimization in a large-scale application [27] it is the most suitable for high-fidelity multidisciplinary design optimization of engineering systems and by far the best option. The specific algorithm chosen is the Sequential Least-Squares Programming (SLSQP) a method shown to outperform others [28] and commonly used in aerostructural problems [29].

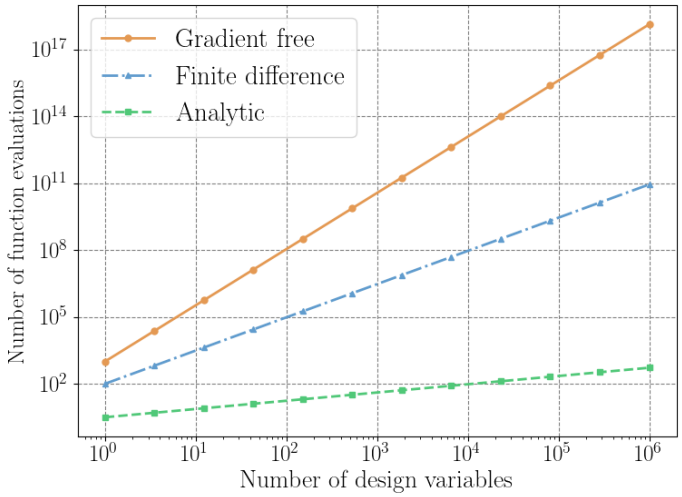

Figure 2.3: Cost of optimization with different methods of sensitive analysis [17].

2.3 Multidisciplinary Optimization

When the topic is optimization in the aerospace sector, the aim is to reduce energy needs to accomplish the mission, by decreasing the weight of the structure and increasing the aerodynamic efficiency of the aircraft (ratio between lift and drag produced by an airplane). Therefore, when the weight of an aircraft is decreased, the necessary lift to maintain the UAV in level flight is reduced. This decrease in lift leads to a reduction in the drag produced by the UAV's wings and energy consumption. Moreover, if the wing is aerodynamically optimized, its efficiency will increase, reducing once again the drag of the aircraft, improving the UAV. In addition to reducing operating costs, and increasing the perceived value of the UAV, this increase in overall efficiency can yield various advantages in terms of performance [10], like increased range, or increased payload capacity and take-off field length.

When the aim is to achieve the best solution possible, it is essential to consider that a wing is a flexible structure, meaning it undergoes bending and twisting under the influence of external forces. The initial, unloaded shape of the wing, as manufactured is different than the one during flight, the wing structure experiences strain until it reaches a balance between elastic and aerodynamic forces [10]. An illustration of that effect can be seen in Figure 2.4, where the wing's bending of the TEKEVER AR5 is shown in jig position and under cruise 1-g flight condition.

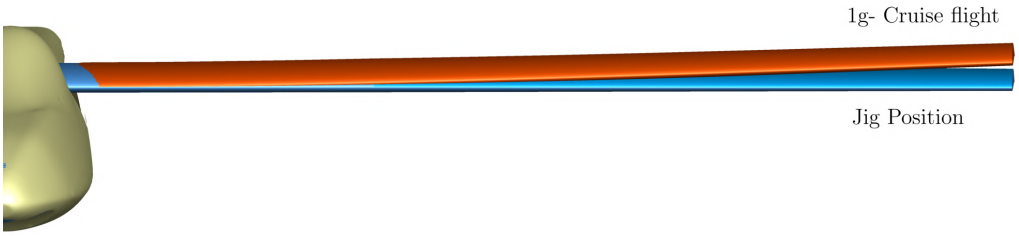

Figure 2.4: TEKEVER AR5 wing shape comparison between jig and cruise flight.

The importance of taking wing bending and twisting into account becomes apparent when comparing the spanwise lift distribution of both a rigid wing and a flexible wing. Due to the twist, the effective angle of attack of a wingspan section changes directly, influencing the pressure distribution and lift distribution as can be seen in Figure 2.5. Therefore, it is important to follow a design model that takes into account the elasticity of the wing using a couple approach between the aerodynamic and structural disciplines.

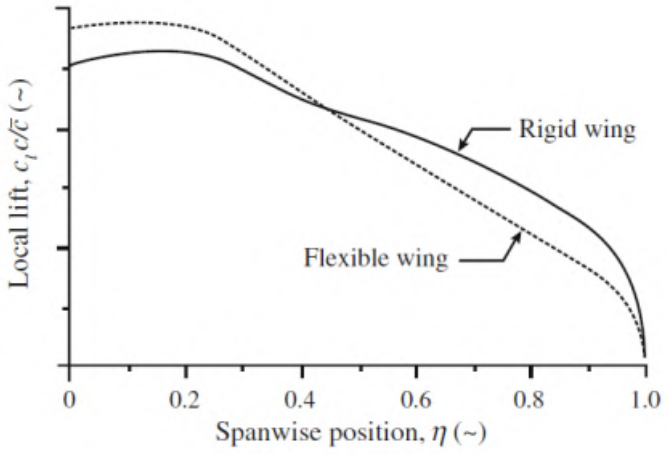

Figure 2.5: Spanwise lift distribution difference between a Boeing B-47 Stratojet flexible and rigid wing [10].

It is also interesting to notice that this kind of framework is not limited to the aerospace industry. In the literature, some examples can be found, MDO was employed to improve the safety of an automobile where pareto front was made with the trade-off between deformation in a crash and mass [30], and in the piping industry, where the aerostructural optimization of a valve produces a 50% reduction in pressure loss while maintaining the minimum structure stability [31].

In summary, multidisciplinary design is a technique that can be relied on whenever there is a strong interaction between two or more disciplines, such that the optimal solution can only be achieved by opti-

mizing both aspects simultaneously. To perform the multidisciplinary optimization a suitable architecture considering the problem in question should be employed.

Multidisciplinary Architectures

In the context of multidisciplinary optimization, a single optimization problem is constructed to address the entirety of the original individual situations. In the form of an monolithic architecture This poses challenges, particularly when dealing with a multitude of variables and constraints. The issue is exacerbated when the coupling between disciplines is weak, as the disadvantages of the approach outperform the advantages since the computational cost increases but the final result barely changes. As already discounted, this is not the case for aerostructural optimization of a wing.

The differences between the differing monolithic architectures are the set of design variables and the constraints that the optimizer is responsible for, which affects how the governing equations are solved. The possibilities are All-At-Once (AAO), Simultaneous Analysis and Design (SAND), Individual Discipline Feasible (IDF), and Multidisciplinary Feasible (MDF), as shown in Figure 2.6.

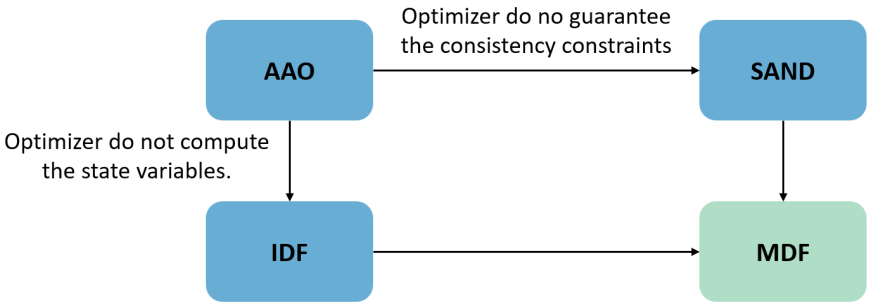

Figure 2.6: Monolithic optimization architectures.

In aerostructural optimization, AAO grants the optimizer control over design variables, ensuring convergence and consistency across disciplines through constraints. While advantageous in influencing the entire vehicle with changes in specific design variables, the complexity of AAO makes it challenging for high-fidelity optimization implementation [16, 32]. SAND, a similar approach to AAO, omits consistency constraints but remains challenging to implement [16]. On the other hand, IDF represents a simpler alternative, allowing discipline convergence without optimizer intervention, especially effective when employing well-established Computational Fluid Dynamics and Computational Structural Mechanics [32].

Finally, the MDF is simplest at the optimizer level as it works comparable to a normal single discipline optimization, where the optimizer only minimizes the solution and the evaluation of the objective function regarding the DV is given by a Multidisciplinary Analysis (MDA) [16, 32]. Besides, this approach has an advantage in case of optimizer failure, as all intermediate solutions are feasible. Also, it is the simplest and most accurate [32]. For all these reasons, this approach is the one employed in the MACH-Aero framework [33] used in this work. Figure 2.7 showcases in a scheme the analysis step of the MDF approach.

For a detailed breakdown of each architecture mentioned here, along with additional models, and an extensive comparative assessment of their simplicity, accuracy, and efficiency, refer to [32].

Multidisciplinary Analysis Technique

As already discounted, an MDF approach is going to be used, therefore, it is necessary the use of a multidisciplinary analysis. This could follow several methods: Jacobi, Gauss-Seidel and Newton. The first two methods are fixed-point methods, when solving a discipline, the data from other disciplines are kept fixed. In contrast, the Newton changes and solves all disciplines in each iteration [18].

In the Jacobi method, the MDA of each analysis is run using the previous iteration output from the other discipline analyses. Since the outputs from the other analyses are kept constant in each iteration, it is possible to run the analyses in parallel [18, 34], which could give this method an advantage. It was observed in [34] that this advantage did not reveal in the final result a reduction in the overall time needed. Besides that, it generally suffers from poorer stability and slower convergence as each solver is working with out-of-date information about the state of the other discipline [35].

The Newton approach involves advancing the response of the complete system simultaneously in each iteration. Unlike fixed-point approaches, the governing equations are not solved in each iteration. Instead, a linear system of equations is used that involves only the residuals and their partial derivatives [18]. However, it is not very appealing as developing a coupled system requires more implementation time than reusing the individual solvers, which is a major concern [35].

Finally, when using Gauss-Seidel iterations to converge the MDA, each analysis is run using the most recent output from the other analyses until a consistent set of state variables is returned. In Figure 2.7, a scheme of this method is presented integrated into an optimization.

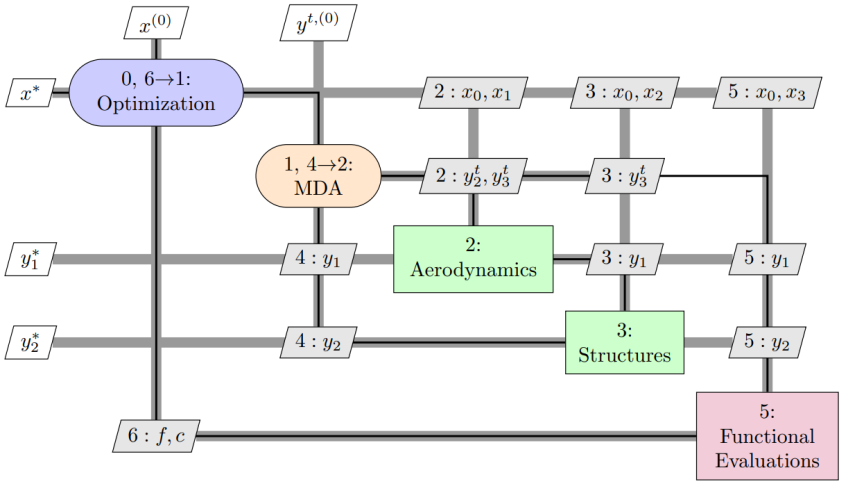

Figure 2.7: Gauss-Seidel MDA procedure [36].

As shown in Figure 2.7, this method considers the global (x_0) and local DV ($x_{1,2,3}$) and outputs the global system response (y_{1-3}) that computes considering the most recent system responses $y_{2,3}^t$. Besides that, the computations appear to be serial. Since each component of the new iterate depends upon all previously computed components, the updates cannot be done simultaneously as in the Ja-

cobi method [18], therefore, having a better stability profile. This method was shown in [34] to be the most efficient when considering conceptual aircraft design. In addition, previous literature where an aerostructural optimization of a wing using the MACH-Aero framework also used the Gauss-Seidel method [35, 37]. For all the reasons stated, the method chosen to perform the MDA convergence is the Gauss-Seidel.

To perform this coupled aerostrutural analysis, there is a need for an efficient way to transfer the quantities of interest between the two disciplines, which is going to be addressed next.

2.4 Fluid-Structure Interaction

As the multidisciplinary analysis takes place, the fluid and structure interactions imply a connection between the fluid and structural domains, achieved by exchanging forces and displacements across a wetted structural wall. The geometrical discretization employs two distinct approaches, tailored to meet the specific demands of solving structural and flow equations. Accurate boundary descriptions are essential for resolving flow issues, whereas structural analyses often simplify the body, using for exemple shell elements. Despite this simplification, the model efficiently captures essential static. Even when structural and flow discretizations aim to represent the same boundary surface, computational nodes for the structure typically differ due to the higher resolution required in flow computations to address smaller scales [18].

The aerodynamic model implemented in ADFlow predicts fluid motion, forces on the structure, the aerodynamic forces and the correlation between fluid flow and pressure on a structure with a fluid-solid interface. The structural model implemented in TACS estimates the surface displacements under the aerodynamic load.

2.4.1 Load and Displacement Transfer

The load-displacement transfer methodology employed in MACH-Aero is the Rigid Link Transfer (RLT) [35, 38], and it was developed in [39]. A scheme of the RLT method for displacement transfer are elucidated in Figure 2.8. The procedure starts by identifying the closest point on the structural mesh for each aerodynamic surface node. Subsequently, the TACS shape function is employed to interpolate the translation and rotation of the link's base, facilitating the computation of the aerodynamic node displacement based on the rigid translation and rotation of the link given by

$$\{u_A\} = \{u_t\} + \{u_r\} \times \{r\} \quad , \tag{2.1}$$

where u_A, u_t, u_r represents the aerodynamic displacement, the structural displacement, the rotations at the structural surface respectively, and r is the vector of minimum distance connecting the points in the structure to the points on the aerodynamic surface.

This approach allows the representation of aerodynamic nodal displacements as a linear function of the structural states. It is imperative to acknowledge, however, that this method exhibits limitations in

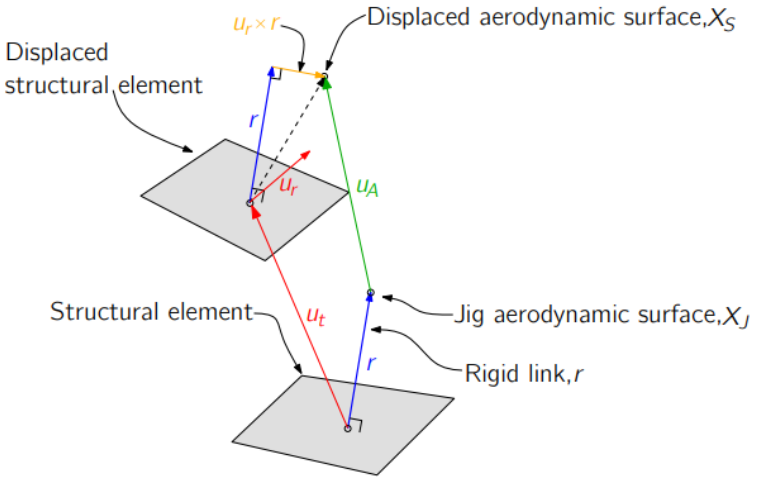

Figure 2.8: Displacement transfer [35].

accuracy when confronted with large rotations. Specifically, the term responsible for computing aerodynamic displacement due to structural rotations is a linearized approximation. The RLT method has been seamlessly integrated into the TACS source code, aligning with TACS capability to compute gradients analytically [35, 40].

Ultimately, the method of virtual work provides a means to ascertain the nodal forces and moments influencing the structure, as outlined in [41]. In this context, the virtual work associated with aerodynamic pressure forces is a pivotal component of the analysis and it is given by,

$$\delta W = \int_{S_A} p\mathbf{n} \cdot \delta \mathbf{u}_A \, dS = \int_{S_A} p\mathbf{n} \cdot \delta \mathbf{u}_t - p\mathbf{n} \cdot (\mathbf{r} \times \delta \mathbf{u}_r) \, dS \tag{2.2}$$

where p is the surface pressure, $\mathbf{n}$ is the normal defined on the aerodynamic surface mesh. Note that the integration is performed on the aerodynamic surface. This expression may be used to determine a consistent and conservative load vector.

A comparative review of numerical fluids/structures interface methods for computations using high-fidelity equations can be found in [42].

2.4.2 Mesh Updating

In the course of performing aerostructural optimization, changes to the external shape of the aircraft arise from both design adjustments and structural deformations. To address these changes in surface geometry, it becomes essential to smoothly modify the volume mesh in Computational Fluid Dynamics, ensuring the integrity of high-quality cells. MACH-Aero employs an Inverse-Distance Weighting method (IDW), proposed in [43] that demonstrated that its ability to maintain satisfactory orthogonality in cells near the wall, a critical consideration for Reynolds-averaged Navier-Stokes (RANS) meshes.

In IDW method, the displacement of a volume vertex is computed as a weighted average of the displacements of the boundary vertices, the weight being the inverse of the distance between the volume point and the boundary ones. In other words, the closer a boundary vertex is to the considered volume

vertex, the stronger its influence on the displacement of the volume vertex is [44].

The displacement field in the volume mesh is defined as

$$u(r) = \frac{\sum w_i(r)u(r)}{\sum w_i(r)} \tag{2.3}$$

where r is the coordinate vector in the original mesh, $u(r)$ is the displacement field, $u_i(r)$ is the nodal displacement field around boundary vertex i, and w_i is a weight coefficient.

This method has been used successfully with the MACH-Aero framework, for example, in a wind turbine optimization [45] or the optimization of ducted hydrokinetic turbines in [46].

2.4.3 Sensitive Analysis

As previously mentioned, the optimization process will employ a gradient-based method. This approach requires the computation of derivatives of bouth objective and constraint functions with respect to the DVs, and the method used to obtain these derivatives significantly influences the speed of the solution, as illustrated in Figure 2.3. The derivatives will be computed using the chain rule and the adjoint method that scales with the number of objective functions and constraints, being theoretically independent of the number of design variables, since they far outnumber them [17]. In problems of this nature, the number of design variables typically exceeds the number of constraints and objective functions. Research has shown that, in such cases, this approach is the fastest [47]. Considering the total derivative of the function of interest, J , is given by

$$\frac{dJ}{dx} = \frac{\partial J}{\partial x} + \begin{bmatrix} \frac{\partial J}{\partial x_{sA}} & \frac{\partial J}{\partial x_{sS}} \end{bmatrix} \begin{bmatrix} \frac{dx_{sA}}{\partial x} \\ \frac{dx_{sS}}{\partial x} \end{bmatrix} \tag{2.4}$$

where the governing set of nonlinear equations are expressed as $R(u, x) = 0$, where x_{sA} and x_{sS} represents either aerodynamics (subscript A) and structures (subscript S) state variables, x the design variables for each discipline. Moreover, knowing that the derivative of the residuals can be given by

$$\begin{bmatrix} \frac{dR_A}{dx} \\ \frac{dR_S}{dx} \end{bmatrix} = \begin{bmatrix} \frac{\partial R_A}{\partial x} \\ \frac{\partial R_S}{\partial x} \end{bmatrix} + \begin{bmatrix} \frac{\partial R_A}{\partial x_{sA}} & \frac{\partial R_A}{\partial x_{sS}} \\ \frac{\partial R_S}{\partial x_{sA}} & \frac{\partial R_S}{\partial x_{sS}} \end{bmatrix} \begin{bmatrix} \frac{dx_{sA}}{dx} \\ \frac{dx_{sS}}{dx} \end{bmatrix} = 0 \tag{2.5}$$

after substituting in equation (2.4)leads to

$$\frac{dJ}{dx} = \frac{\partial J}{\partial x} - \underbrace{\begin{bmatrix} \frac{\partial J}{\partial x_{sA}} & \frac{\partial J}{\partial x_{sS}} \end{bmatrix} \begin{pmatrix} \frac{\partial R_A}{\partial x_{sA}} & \frac{\partial R_A}{\partial x_{sS}} \\ \frac{\partial R_S}{\partial x_{sA}} & \frac{\partial R_S}{\partial x_{sS}} \end{pmatrix}^{-1}}_{\lambda^T} \begin{bmatrix} \frac{\partial R_A}{\partial x} \\ \frac{\partial R_S}{\partial x} \end{bmatrix} \tag{2.6}$$

with partial derivatives that are cheap to calculate. To solve this equation, it is necessary to find λ using the adjoint method, since there are more design variables than metric functions [48]. The coupled system of adjoint equations is treated as a single, unified problem, directly addressing the interdependen-

cies between different disciplines by solving the entire set of coupled adjoint equations simultaneously,

$$\begin{bmatrix} \frac{\partial R_A}{\partial x_{sA}} & \frac{\partial R_A}{\partial x_S} \\ \frac{\partial R_S}{\partial x_{sA}} & \frac{\partial R_S}{\partial x_{sS}} \end{bmatrix} \begin{bmatrix} \lambda_A \\ \lambda_S \end{bmatrix} = \begin{bmatrix} \frac{\partial J}{\partial x_{sA}} \\ \frac{\partial J}{\partial x_{sS}} \end{bmatrix} , \tag{2.7}$$

and λ the adjoint variables. This ensures that all disciplinary interactions are accounted for in a cohesive manner, leading to more accurate sensitivity analysis and faster convergence. For a detailed explanation of the inner working of the method and implementation strategy refer to [38]. The adjoint solver is converged using the Krylov subspace approach. The gradient of the objective (or constraint) function J with respect to the design variables x is then given by

$$\frac{dJ}{dx} = \frac{\partial J}{\partial x} - \lambda_A^T \frac{\partial R_{sA}}{\partial x} - \lambda_S^T \frac{\partial R_{sS}}{\partial x} . \tag{2.8}$$

The partial derivatives are computed using a combination of methods: aerodynamic derivatives are obtained through reverse-mode automatic differentiation with Tapenade, structural derivatives are calculated analytically [40].

Chapter 3

Aerodynamic Analysis and Optimization

This chapter provides an overview of the computational fluid dynamics background and the models selected to address our research problem. The rationale behind choosing these models had been thoroughly justified in a previous work [12] that forms the foundation for the review and update undertaken in this chapter. Additionally, insights are shared about the aerodynamic optimization process of our UAV regarding single-discipline optimization. A test case is displayed to demonstrate the capability of the numerical tools and also the redesign of the TEKEVER AR5 winglet.

3.1 Flow And Turbulence Models

In this section, the basic elements in CFD such as the flow model, equations solved, and turbulence model will be introduced, followed by an outline of the process of conducting a CFD analysis.

The Navier–Stokes equations are partial differential equations that describe the motion of viscous fluids using the conservation laws of mass, momentum and energy. In the differential form, they can be written as [49]

$$\frac{\partial \rho}{\partial \mathrm{t}} + \frac{\partial}{\partial x_i}(\rho v_i) = 0, \tag{3.1a}$$

$$\frac{\partial}{\partial \mathrm{t}}(\rho v_i) + \frac{\partial}{\partial x_j}(\rho v_j v_i) + \frac{\partial p}{\partial x_i} - \frac{\partial \tau_{ji}}{\partial x_j} = 0, \tag{3.1b}$$

$$\frac{\partial}{\partial \mathrm{t}}\left[\rho E_t\right] + \frac{\partial}{\partial x_j}\left[\rho v_j H\right] - \frac{\partial}{\partial v_j}(v_i \tau_{ij}) + \frac{\partial q_j}{\partial x_j} = 0 \tag{3.1c}$$

where v is the velocity, ρ is the density, p is the pressure, τ is the viscous shear stress tensor, E_t is the total energy, H is the enthalpy, q is the flow temperature flux, t is time and x_i are the 3 directions of the cartesian coordinate system. For this work external forces, work heat were not considered. With

the Navier-stokes equations, the full behavior of the flow can be obtained. However, because of the presence of non-linear convection terms, once a critical Reynolds number is surpassed, an inherent instability in the flow emerges. This leads to the generation of fluctuations, resulting in the transition of laminar to turbulent flow. To address this phenomenon, numerous models have been developed, each varying in complexity.

Higher fidelity simulations must use techniques to model the turbulence in the fluid. For engineering purposes the best computationally affordable option for flow modeling is using RANS [12, 16, 50], specifically considering the purpose of doing optimization witch remains a computationally intensive and difficult task [51]. Moreover, during the simulation, it is crucial to develop an appreciation for the implications of the turbulent regime. To achieve this, it is necessary to calculate the corresponding dimensionless parameters, namely the Reynolds number,

$$R_e = \frac{\rho \cdot v_\infty \cdot c}{\mu} \tag{3.2}$$

with v_∞ the free flow velocity, c the average aerodynamic chord and μ the dynamic viscosity. Therefore, the Reynolds $1.1 \cdot 10^6$ can be computed from the basic characteristics of Table 1.1. This suggests that turbulent flow dominates. Therefore, the use of lower fidelity models that do not account for the turbulence effect will produce poor results.

RANS is a flow model where the fluctuations in all the fields are removed, and only the average effect of the flow is considered. The RANS for a compressible flow are akin to the standard Navier-Stokes equations, but the finals are average with respect to density for all variables except density denoted with a and introduce a new term, the Reynolds stresses ($\overline{\rho v_i' v_j'}$), representing apparent stress due to fluctuations in velocity and turbulent energy flux being represented by the follwing system of equations [49]:

$$\frac{\partial}{\partial x_i}(\bar{\rho}\tilde{u}_i) = 0, \tag{3.3a}$$

$$\frac{\partial}{\partial x_j}(\bar{\rho}\tilde{v}_j\tilde{v}_i) = -\frac{\partial \bar{P}}{\partial x_i} + \frac{\partial}{\partial x_j}\left[\tau_{ji} - \overline{\rho v_i' v_j'}\right], \tag{3.3b}$$

$$\frac{\partial}{\partial x_j}(\bar{\rho}\tilde{v_j}H) = \frac{\partial}{\partial x_j}\left[-q + \overline{\tau_j v_i''} - \overline{\rho u_j'' \frac{1}{2} v_i'' v_i''}\right] + \frac{\partial}{\partial x_j}\left[\tilde{v_i}(\tilde{\tau_{ij}} + \overline{\rho v_i' v_j'})\right], \tag{3.3c}$$

with $\bar{P}$ being the pressure obtained by the state equation ρRT.

However, as the connection between these new terms and mean flow properties is unknown, the equation system ends up with more unknowns than equations. To address this, Reynolds stresses are modeled based on theoretical and empirical insights into turbulence structure and its relationship with the averaged flow. The turbulence models appear from the necessity of solving real-world problems with reasonable computation effort promptly, resulting in the implementation of Reynolds Averaged Navier-Stokes, a trade-off between accuracy, effort, and the need to close the equation system.

ADFlow has implemented various turbulence models, namely Spalart-Allmaras, Wilcox k-w, and

Menter Shear Stress Transport (SST) [52]. The Spalart–Allmaras model [53] was designed specifically for aerospace applications involving wall-bounded flows and it uses a one-equation to solve a modeled transport equation for the kinematic eddy turbulent viscosity. The Spalart–Allmaras model has demonstrated good results for boundary layers subjected to adverse pressure gradients and it is effective at the low-Reynolds number. Nevertheless,it cannot be relied on to predict flow separation [54, 55]. This model is the one that will be used with the additional advantage of already been differentiated in ADFlow to allow for faster optimization. Besides that, this model has shown concordance with empirical data of external flow around airfoils with Reynolds number close to the one used in this work [54, 56].

3.2 Implementation

The implementation of the aerodynamic optimization follows the steps shown in Figure 3.1.

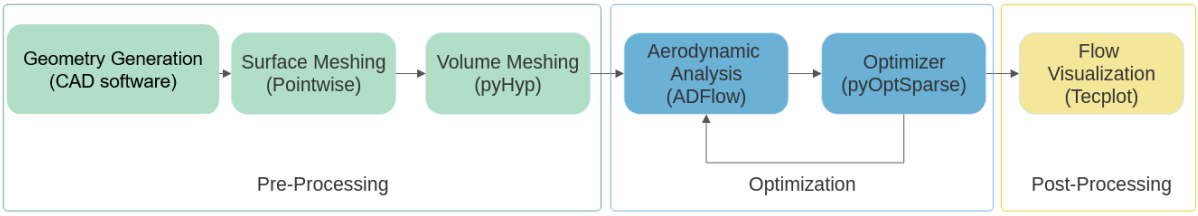

Figure 3.1: Aerodynamic optimization flowchart.

The steps taken are explained in the following sections.

3.2.1 Geometry Definition

The initial stage of creating an aerodynamic analysis is to set up the geometry intended for research. Within the MACH-Aero framework, it is possible to accomplish this by using a dedicated commercial CAD (Computer Aided Design) software or pyGeo, an open source software[57]. The objective of this step is to have the geometry in a file type readable by the mesh generator. Therefore, using the first method, the file has to have a common format in the CAD and meshing software, thus, it must be saved as a standard CAD file (iges).

3.2.2 Mesh Generation

Before conducting the analysis, a surface mesh derived from the geometry description file must be created. This surface mesh is then used for constructing the volume mesh required to carry out the analysis. As the objective of this process is to perform an aerostructural optimization, using ADFlow as the solver, the generated mesh must use structured and with overset capability [52].

Once a surface mesh is created in the appropriate format, the next step involves extruding a hyperbolic volume mesh using pyHyp, a hyperbolic mesh generator. pyHyp offers the convenience of automatically applying the necessary boundary conditions for a wing [58], namely the wall boundary

condition (flow velocity equal to zero) and far field boundary condition (flow velocity equals free stream flow). To generate a volume mesh from a surface mesh using pyHyp, at least the first layer height, the total height of the volume mesh, and the number of layers to extrude must be specified. Moreover, some parameters are present to control the volume extrusion process, however, default ones where used as they generated good quality meshes. A mesh is considered high quality if it has no negative volumes, consists of orthogonal cells, and each cell's edges are of uniform length.

As the Spallart-Allmaras turbulence model will be employed, a y+ value close to unity is required [59]. Using the flat-plate boundary layer theory, by equation

$$\Delta s = \frac{y^+ \mu}{v_{fric} \rho}\,, \tag{3.4}$$

where

$$v_{fric} = \sqrt{\frac{\tau_{wall}}{\rho}}, \quad \tau_{wall} = \frac{C_f \rho v_\infty^2}{2} \quad \text{and} \quad C_f = \frac{0.027}{Re_x^{1/7}}$$

with an initial wall spacing is estimated to be approximately 1.3×10^{-5}m.

The a grid independent result that ensure the physics of the flow is being captured, for the detailed wing of the TEKEVER AR5 UAV, is depicted in Figure 3.2 the structure of the final volume mesh can be seen.

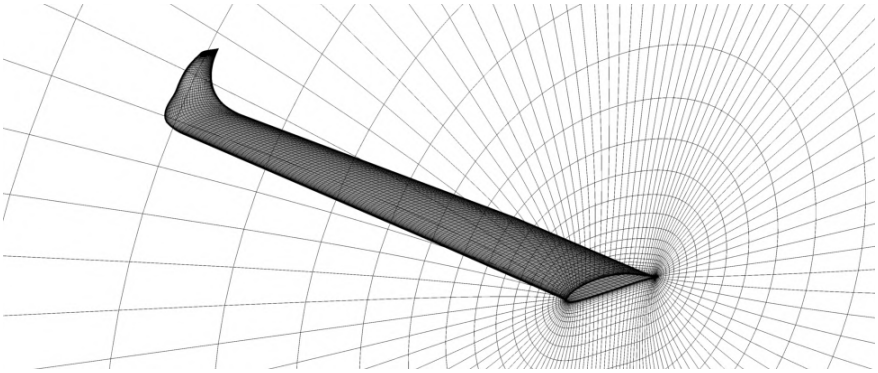

Figure 3.2: Volume mesh of the TEKEVER AR5 wing.

Moreover, the study of fuselage effect over the overall wing performance will be performed. Given the complexity of the geometry, it will be necessary to use a mesh overset to model the different sections of the wing (fuselage, collar and wing). This process involves creating volume grids for each individual component, creating a background grid, and finally assembling all the individual grids. In the first step of the process, overset boundary conditions are used to replace far-field conditions. Consistent cell sizes are crucial in the intersection region to ensure accurate results. In the second step, a refined collar mesh is generated between the wing and fuselage to avoid gaps at intersections. Some considerations should be made in relation to this process. The general suggestion made by the MDO Lab at the University of Michigan needs to be followed, so it is necessary to have overlap between the collar mesh and the two other parts to fulfill its main objective. To achieve this, a surface cut at the fuselage and wing should be made around the intersection zone. After that, the surface obtained should be meshed. The volume mesh should have the same volume growth factor as the remaining parts to achieve similarly sized cells

at the mesh intersections [57]. Moreover, the general parameters for the meshing algorithm used for the wing should be modified to better model the collar volume mesh, as suggested in [12]. Increasing the explicit, implicit, and Kinsey-Barth smoothing parameters will prevent negative volumes from forming at the very tight angles of the collar surface. The volume coefficient should be increased to improve grid quality near the wall, since the far-field case will be handled by another mesh.The final step is to generate a uniform cartesian grid around the nearfield meshes. This grid is extends to the far-field distance with an O-type topology grid. All this is handled by built in pyHyp functions that generate simple uniform orthogonal meshes. All the generated meshes are joined in the same file by cgns utilities also implemented in MACH-Aero.

To perform the analysis, ADflow uses Implicit Hole Cutting (IHC) to automatically assign overset connectivity and define the role of each cell in computations. IHC is based on the assumption that cells are finer near walls, or can follow an user set priority to specify the computed cells, blanked, interpolate ones and achieve the final computational mesh. The compute cells represent active ones where the partial differential equations are enforced; blanked cells are inactive, that are inside bodies or overlapped by better quality cells; and interpolated cells that inherit state variables from donor cells belonging to more than one meshes.

The overset mesh described in this section is illustrated in Figure 3.3, where the surface differentiated by wing mesh is blue, collar mesh orange and fuselage mesh yellow, and the expansion at symmetric zone, from the detailed near field to the coarsen far field can be seen.

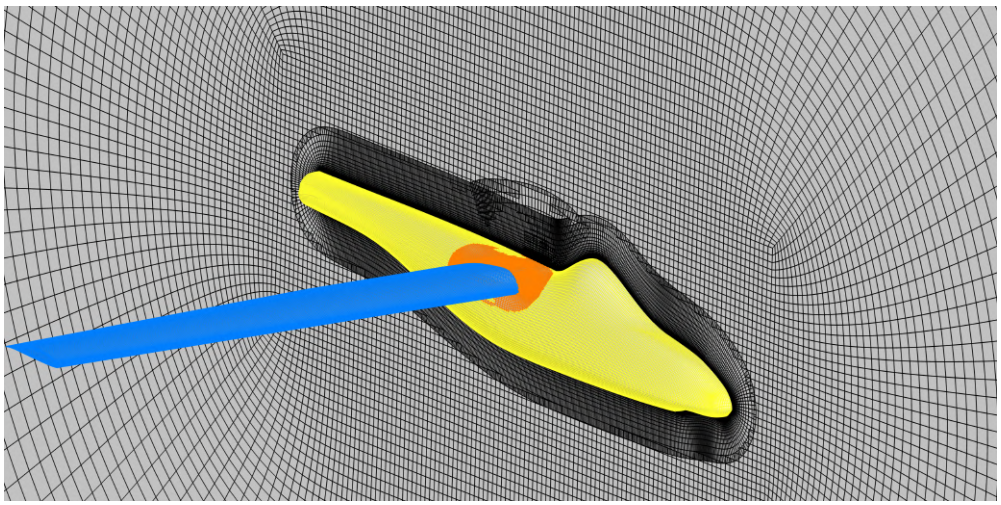

Figure 3.3: Volume mesh of the TEKEVER AR5, showing the collar, fuselage, and wing meshes.

3.2.3 Flow Simulation

Before performing flow simulation it is interesting to understand the main characteristics of the flow solver being employed, ADflow is an open-source computational fluid dynamics solver specifically designed for aerodynamic and multidisciplinary design optimization. It solves the Reynolds-Averaged Navier–Stokes equations efficiently, making it ideal for both aerodynamic and aerostructural analyses [60].

ADflow provides several advantages for optimization. It features direct memory access via an API, allowing the solver to be loaded as a library, which eliminates the need for disk input/output operations and drastically speeds up optimization tasks, particularly when iterating over multiple designs. The solver is highly robust in automation, designed to handle a wide range of operating points without user intervention, enabling fully automated workflows. Another key feature is solution warm-starting, which allows each simulation to begin from the converged state of a previous solution, reducing the overall computational cost. Additionally, ADflow utilizes the adjoint method [53], which makes it efficient at computing gradients of objective functions with respect to design variables, essential for gradient-based optimization algorithms. The solver is also highly flexible, supporting integration with other solvers (structural or propulsion models) and can handle various aerodynamic scenarios, such as multipoint optimizations or parameter sweeps [60]. Finally, the solver is controlled through a Python API, making it easy to script complex workflows and integrate with other tools.

ADflow supports various inviscid flux schemes for flow prediction, including the Jameson–Schmidt–Turkel (JST) scheme with scalar dissipation [53]. It also offers several turbulence models for RANS simulations, with the Spalart–Allmaras model being the default also fully differentiated to ensure compatibility with ADflow's adjoint-based gradient computation, providing accurate sensitivity analysis for optimization tasks [53].

To ensure robust convergence, ADflow employs multiple solver strategies. The Approximate Newton-Krylov (ANK) solver [60] is used in the intermediate phase of convergence, providing robustness for nonlinear flow cases. As the solution nears its final state, the solver switches to the Pure Newton-Krylov solver, which offers rapid, quadratic convergence. This ensures faster results when the solution is close to being finalized.

Finally, to perform the analysis itself, after the mesh is generated, some additional parameters are needed. The aerodynamic problem must be defined including the angle of attack, α, cruise speed, U_∞, and altitude, h, with the values of Table 1.1 and corresponding temperature, density, and pressure automatically computed using the International Stander Atmosphere [61, 62] for a trimmed α of 1.9 $^\circ$.

Moreover, it is important to address the compressibility effect through the computation of the Mach number trough

$$M = \frac{v}{a} \tag{3.5}$$

with the sound speed at the cruise altitude of 339,12 m/s. The Mach number obtained for our UAV is approximately 0.08, therefore, compressive effects are not expected for the low Mach number. However, using ADflow a compressible fluid solver may result in reduced accuracy and efficiency at these low Mach numbers. Therefore efforts have been made to address this issue within the context of an approximate Newton-Krylov solver for the Reynolds-averaged Navier-Stokes equations that are being enjoyed in this work. Firstly, a method for scaling artificial dissipation has been integrated to improve accuracy at low Mach numbers, named within ADflow with *acousticScaleFactor* where the Mach number of the free stream is going to be considered as it is the one that showed most accuracy [63]. It is important to mention that loss in performance can be observed with this method, especially for very low Mach

numbers, however, this is not the case. Secondly, it has been shown that characteristic time-stepping, combined with an approximate Newton method, can accelerate convergence for low Mach number flows by reducing the stiffness in the linear system for each Newton iteration with a preconditioner namely the van Leer-Lee-Roe or Turkel [63]. In ADFlow, the option that gives this functionality is called *ANKCharTimeStepType* and it is intended for cases with freestream Mach numbers lower than 0.4, it is also advised the usage of the van Leer-Lee-Roe option as it usually performs slightly better than Turkel [61].

The main solver parameters of the aerodynamic part of this work are presented in Table 3.1, with all others maintained as their default values [52].

Table 3.1: CFD solver parameters.

Discretization	Central difference with JST scalar dissipation
Equation type	RANS
Equation mode	Steady
Turbulence model	Spalart-Allmaras
Acoustic scale factor	0.08164
Pre conditioner	van Leer-Lee-Roe

In terms of stopping criteria for the CFD solver, the maximum number of iterations was set to 10000 and the L2 residual was set to be reduced by 10^{-5}.

3.2.4 MACH-Aero Optimization Framework

Considering figure 3.4 the framework of MACH-aero is showcased, being the general process is described next.

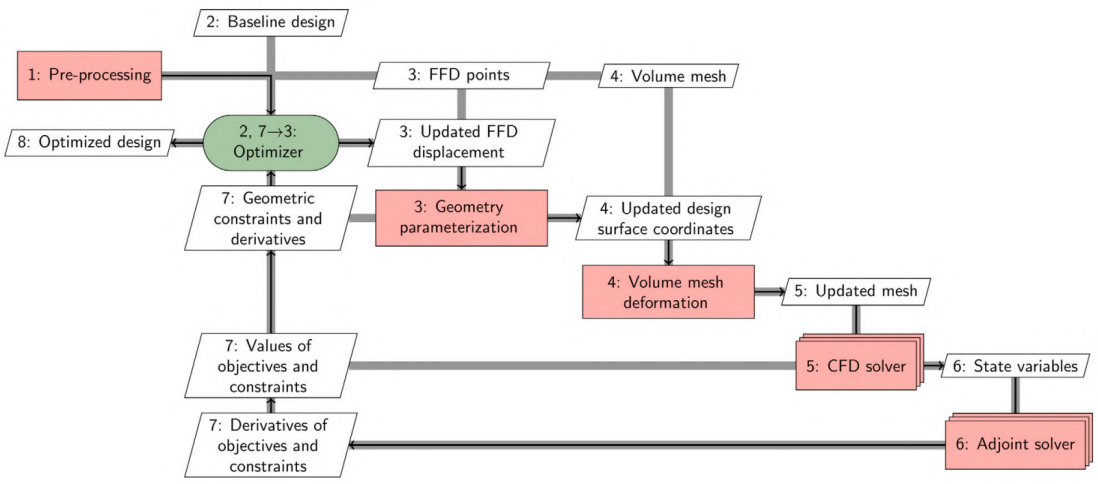

Figure 3.4: MACH-Aero optimization framework [64].

The optimization process employs several tools to efficiently manage the design and modification of aerodynamic surfaces. At the core of this workflow is the optimization tool pyOptSparse, developed by the University of Michigan.

This tool manages the optimization procedure by using an optimization algorithm to determine necessary modifications to the design variables, namely, chord, dihedral, twist, sweep, and shape, based on the objective function, constraints and its derivatives with respect to these variables. It then returns updated design variables essential for generating new shapes.

In parallel with the optimization tool, ADflow is utilized to compute the flow over the aerodynamic surfaces. It solves the governing equations of fluid dynamics to determine the flow field around the geometry, providing essential flow-related outputs, such as pressure and velocity fields. These outputs are critical for evaluating the objective function and its derivatives during the optimization process, ensuring that the modifications made to the design variables lead to improvements in aerodynamic performance.

To efficiently modify geometry without relying on CAD models, the process employs deformative methods, particularly Free-Form Deformation (FFD) [65]. This approach alters the geometry of the aerodynamic surface by surrounding it with a box that can be manipulated according to defined parameters. FFD boxes are created using a pre-built function from pyGeo called createFittedWingFFD, which was modified by [12]. This function generates an FFD box around the entire surface mesh based on surface local normals and a specified displacement, allowing for parameterization of all relevant design variables through division into spanwise sections and segments along the chord, the resulting FFD box for the full TEKEVER AR5 wing can be seen in Figure 3.5 a).

The mapping of each FFD point to a reference axis creates a rigid link that can be controlled through expansion, contraction, and rotation in all direction, allowing for the definition of each design variable.

Although individual point movements can be controlled, this complicates the optimization process by significantly expanding the design space and making it difficult to interpret the final results. Therefore, FFD reduces computational effort by allowing geometry control through a small number of points (parameterization). Those parametric DVs are user defined, their movement and derivatives are handled by pyGeo, being also the bridge between them and the automatic differentiation provided by MACH-Aero. In Figure 3.5 b), some examples can be seen for the twist and taper DV. A small exception exists for airfoil shape optimization, where the control points are allowed to move freely in the vertical direction.

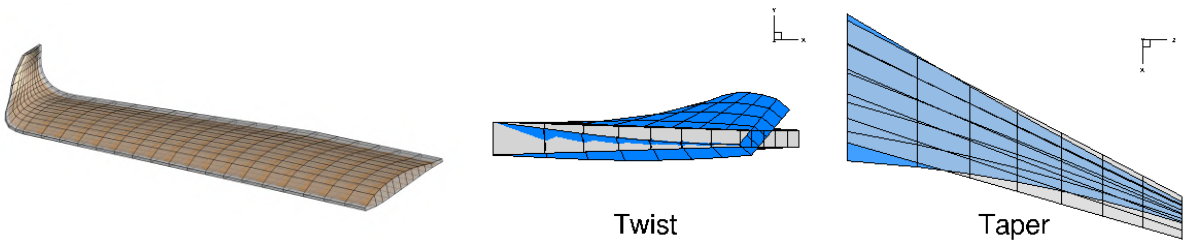

(a) TEKEVER AR5 FFD box.

(b) Parametric twist and taper DVs [57].

Figure 3.5: Wing geometry with FFD boxes.

The overall optimization process consists of several steps, beginning with the initialization of the baseline geometry and the specification of initial design variables. The objective function and constraints are then set up. During the optimization loop, ADflow computes the flow over the geometry to obtain necessary flow-related outputs. The objective function is evaluated based on the current geometry and

flow results, pyOptSparse computes the new DVs values based on the computed gradients [66], and the geometry is modified according to these by pyGeo [67]. A convergence check is performed to assess whether the optimization has reached a satisfactory solution based on defined criteria, such as changes in objective function value.

In each set that the geometry is modified, the IDWarp module is utilized to update the mesh, propagating the geometric deformation throughout the volume mesh[43] as described in section 2.4.2.

3.3 Wing Aerodynamic Grid

The mesh discretization and the domain study for the first geometry that will be used in the aerostrutural optimization are presented.

The grid study was performed in [12] and the main reasoning and steps will now be presented. First, the maximum amount of elements was determined for the existing hardware corresponding to 7-8 million and the convergence study was made by coarsening the grid by a factor of 1.15^3. In all grids, a finer element distribution is evident near both the leading and trailing edges in the streamwise direction, with spacings set at 0.1% and 0.2 % of the local chord. A similar refinement in element size is also present near the wingtip in the spanwise direction. In Figure 3.6, it is possible to see the general mesh structure of these studies.

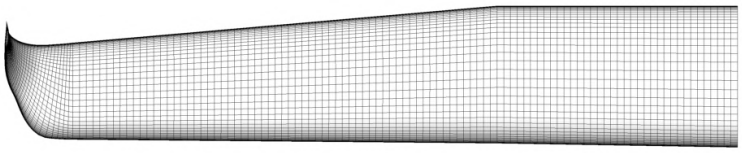

Figure 3.6: Wing surface mesh.

Finally, it was concluded based on [12] that the grid with 1.45 million elements and a base size of 0.0088, despite a 3.9% deviation in drag when compared to the finer grid, was the best option since achieved convergence in only 20% of the time needed for the most refined grid.

Domain size can impact CFD analysis results, so a study was conducted in [12], which led to the belief that increasing the domain size did not significantly impact the computational time due to the geometric expansion employed in the far-field. Hence, selecting a domain with 15 average chords is a good option as it results in the performance parameters being less than 0.5% from the larger domain.

Finally, the $y^+ < 1$ condition mentioned in Section 3.2.3 was checked for the wall spacing of 10^{-5} and verified.

3.4 Wing Aerodynamic Optimization

A demonstration of a case of aerodynamic optimization of the TEKEVER AR5 will be presented next.

3.4.1 Problem Statement

To setup the optimization problem, it is important to define the performance parameters like lift (C_L) and drag (C_D) coefficient, with C_D decomposing into parasite drag from, the friction (due to the existence of boundary layer) and pressure drag (due to the existence of thickness) and induced drag due to lift and vorticity. Moreover, some constraints are also essential, the lift coefficient must be equal to the lift necessary to maintain level flight, $C_{L_{cruise}} = C_{L_{prescribed}} = 0.8932$. The wing area obtained is set to be equal to the original, $S_{proj} = S_{baseline} = 2.169$m. Finally, the thickness must be higher than 90% of the initial one and lower than 200% from structural considerations. As the optimization is the improvement of an existing wing, the twist and chord in the section intersecting with the fuselage must be equal to the original wing to not imply modification of the fuselage. A constraint was applied to decrease the chord along spanwise direction, avoiding oscillation issues.

Table 3.2: Wing geometry control variables.

Variable	**Bounds**	**Control Sections/Points**
Angle of attack	$0°$ to $15°$	-
Angle of twist	$-15°$ to $15°$	28 sections
Chord	15% to 150% of initial value	28 sections
Sweep	$0°$ to $10°$	28 sections
Dihedral	-0.1 m to 0.1 m	28 sections
Airfoil	-0.05m to 0.05m	210 points

In summary the optimization problem can be formally stated as

$$\begin{aligned} \text{minimize} \quad & C_D \\ \text{with respect to} \quad & \alpha,\ \gamma,\ c,\ \Lambda,\ \Gamma,\ \text{airfoil shape} \\ \text{subject to} \quad & C_{L_{cruise}} = C_{L_{prescribed}} \\ & S_{proj} = S_{prescribed} \end{aligned} \tag{3.6}$$

3.4.2 Minimum Drag Wing

Considering the original wing of the TEKEVER AR5 as the starting geometry, the optimization was performed with the new options It was found after 150 iterations for an angle of attack of $0.95°$, the satisfaction of all the constraints and a reduction of -4.76% in C_D a further 0.25% reduction relatively to the optimization performed with the acoustic scale factor option turned off [12]. The resulting geometry is represented in Figure 3.7.

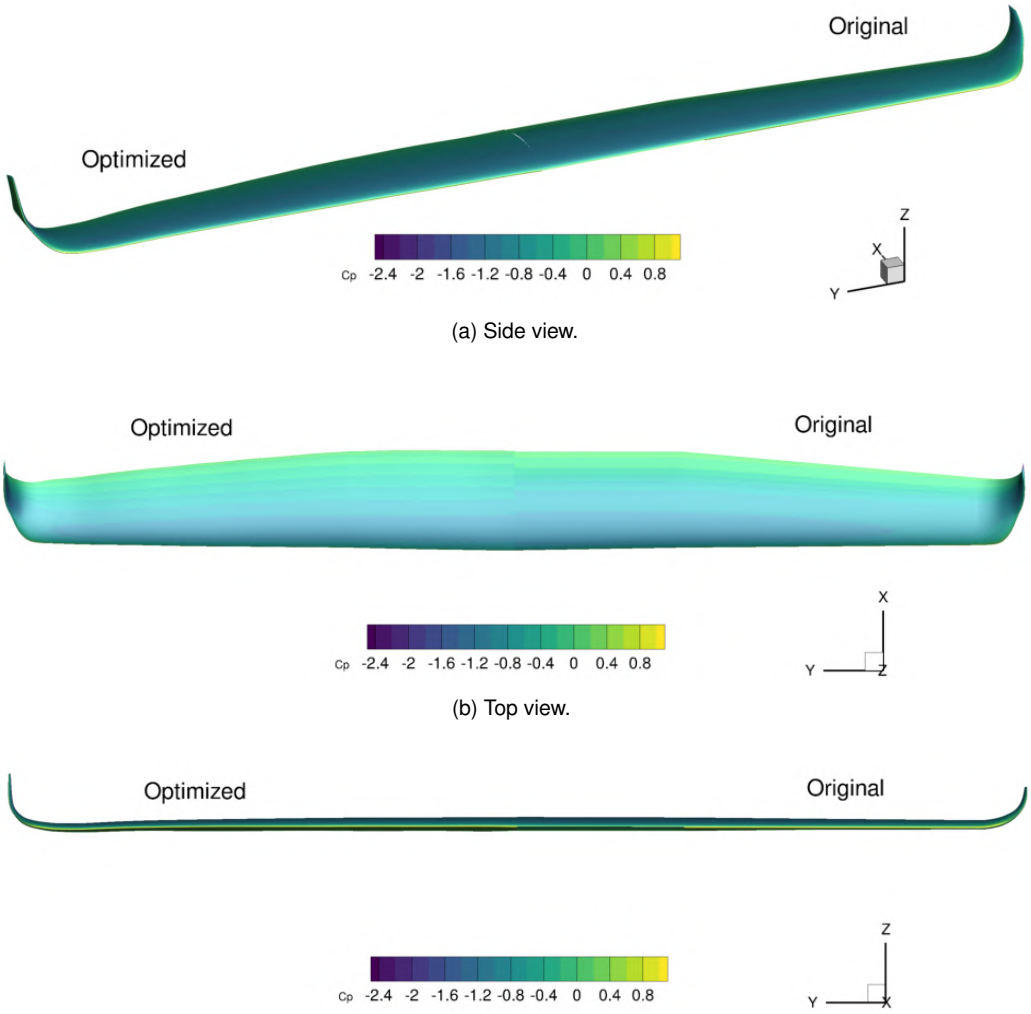

Figure 3.7: Pressure distribution on the TEKEVER AR5 wing and the optimized wing.

In the final design, the dihedral barely changes through the main wing, but had an expressive change in the winglet with a maximum displacement of 68 mm (Figures 3.8c, and 3.7c), as expected since the increase in the winglet size provided a reduction in induced drag of the wing. The chord varied between 1.02 times the original one at the wing tip to 0.95 at the middle section (Figures 3.8b). The sweep variation observed a maximum streamwise displacement of 19 mm at the top of the winglet, however, without an expressive change in the distribution throughout the wing. The twist remained below 1° on the first section reducing near the tip and having a maximum of 12.5° in the final wing section (Figure 3.8a).

Both optimized airfoils are similar to each other, which results in comparable pressure distributions, at the inner sections. However, the twist effect is noticeable near the winglet in the pressure distribution. It is also important to mention that applying the new solver options, including the acoustic scale factor, led to a 6.4% decrease in C_D compared to the original reduction achieved under the same wing and conditions. That is observed due to the elimination of the suction pick in the trailing edge of the wing, as seen in Figure 3.9. As shown in [63] with no scaling, drag diverges as the Mach number is reduced. At low Mach numbers, the drag overprediction for the baseline is caused by a nonphysical suction peak

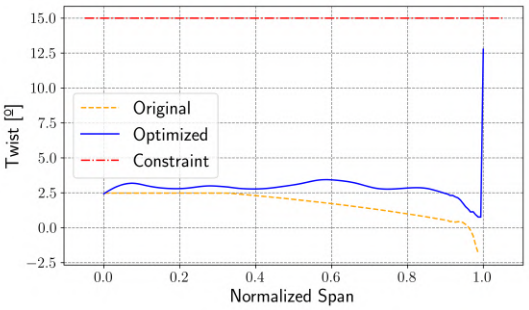

(a) Twist distribution.

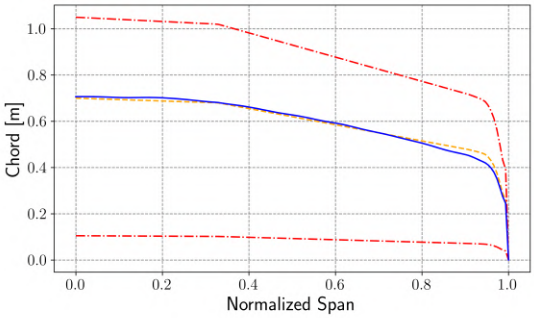

(b) Chord distribution.

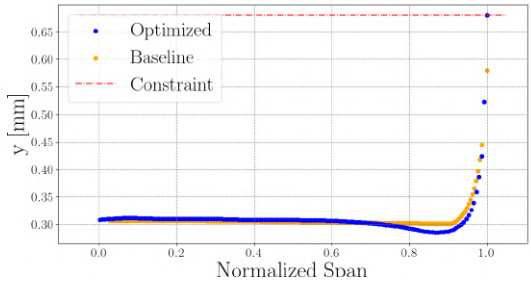

(c) Y coordinate distribution.

Figure 3.8: DVs distribution for the baseline and optimized wing.

on the trailing edge surface. These non-physical pressure fluctuations result from improperly scaled dissipation. By scaling the acoustic contribution, we can remove the trailing edge artifact and obtain more accurate drag values. Furthermore, the lift coefficient, C_L, has not significantly changed due to acoustic scaling, as it is less affected by it, as predicted in [63]. This reinforces the underlying assumption that the non-physical suction peak on the trailing edge is an error and the reason for these different C_D. However, it is important to note that C_L can still be impacted by it if the Mach number is sufficiently low, leading to divergence.

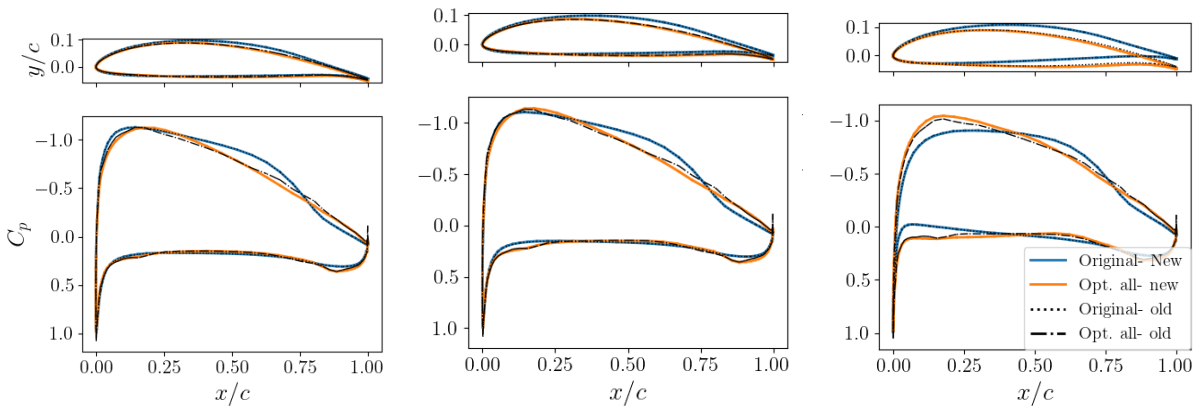

(a) At 1% wingspan.

(b) At 45% wingspan.

(c) At 85% wingspan.

Figure 3.9: Pressure distribution for the original and optimal airfoil in the TEKEVER AR5 in different sections.

3.4.3 Winglet Optimization

The winglet section of the wing is of most importance, allowing for drag reduction through the delay in transition and the reduction in induced drag. In the previous section, it was observed that the maximum change in each DV variable was observed in the winglet region. Alongside with the interest of TEKEVER in understanding the effect of the isolated winglet optimization as no main structural or control components needed to be modified and certificated, it was revealed as interesting to perform the study of the effect of only optimizing the winglet. As no transition model is being applied, the delay in transition for the turbulent state is not being modeled.

The design variables considered are the ones present in Table3.2 but only applied to the last 10 FFD sections, corresponding to the winglet region at the last 10% of wing span. It was found after 89 iterations, for an angle of attack of 1.85° a stall in the optimization with a reduction in C_D of 2.5%. It is important to notice that the diedral DV was max out, representing an increase of 68 mm, as seen in Figure 3.9c, even appearing an down word motion at the the more horizontal winglet section to increase even more the hight difference, showing the desired for an higher winglet. For the remaining DV, overall work was observed to reduce the thickness without violating any of the constraints. Only in the last 10% of the wing span (Figure 3.9), as expected, the dihedral significantly changed, while the remaining DVs kept very close to the original solution for not having much of an impact on the final result.

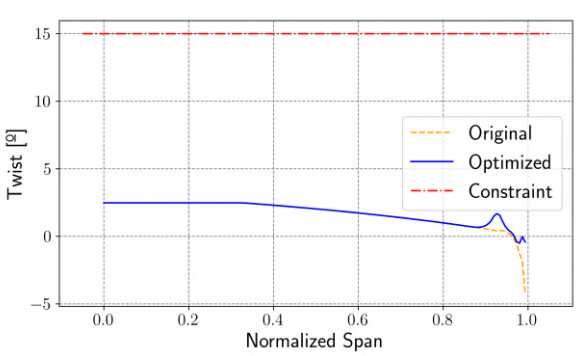

(a) Twist distribution.

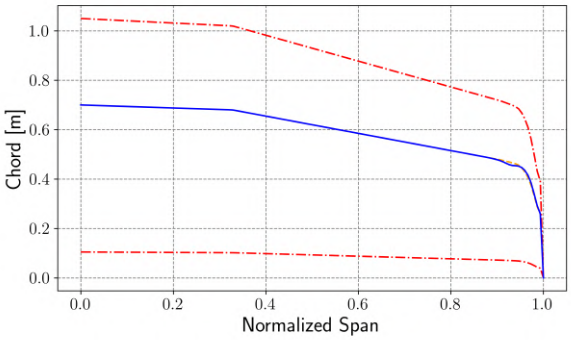

(b) Chord distribution.

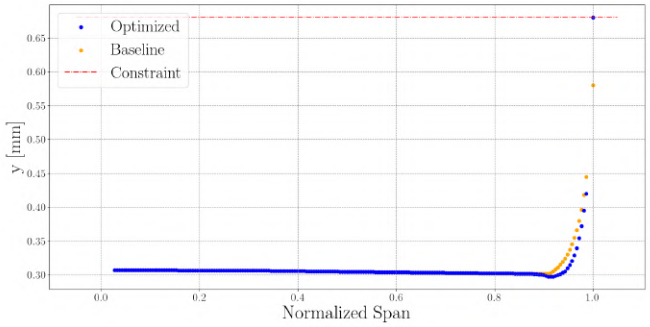

(c) Y coordinate distribution.

Figure 3.9: DVs distribution for the baseline and optimized winglet.

In Figure 3.10, the geometric difference between the two winglets can be observed. In contrast, in Figures 3.11 a) and b) it is possible to observe the different pressure coefficient distribution and the origin of the reduction in drag provided by the new winglet as a C_P suction spot reduction beneath the winglet, which is caused by the wing tip vortex.

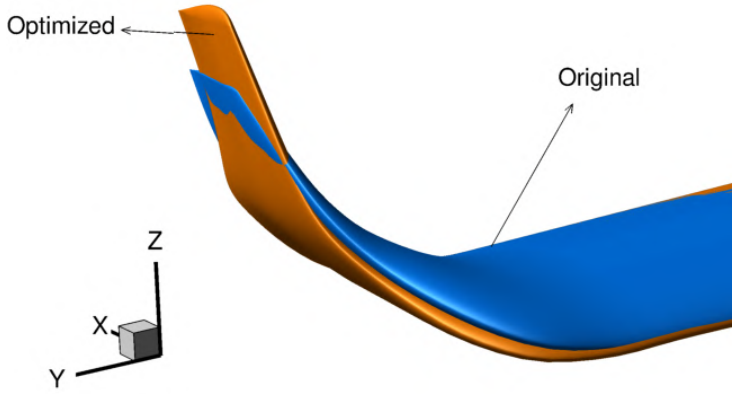

Figure 3.10: Comparison between original and optimized winglet geometry.

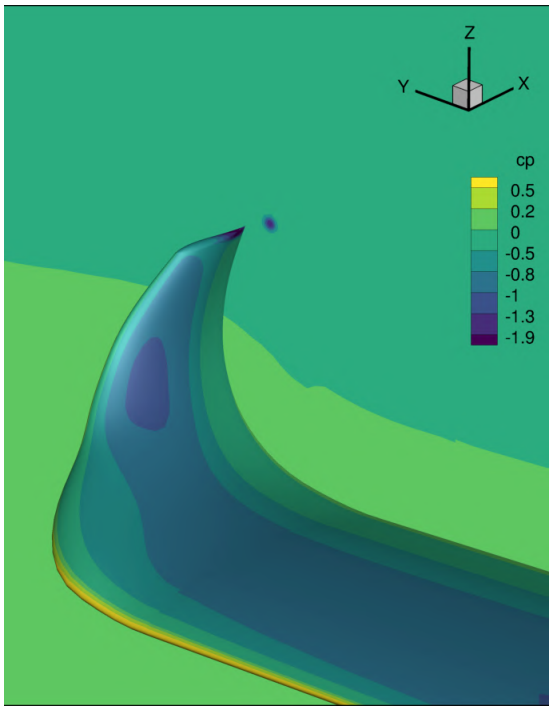

(a) Original winglet.

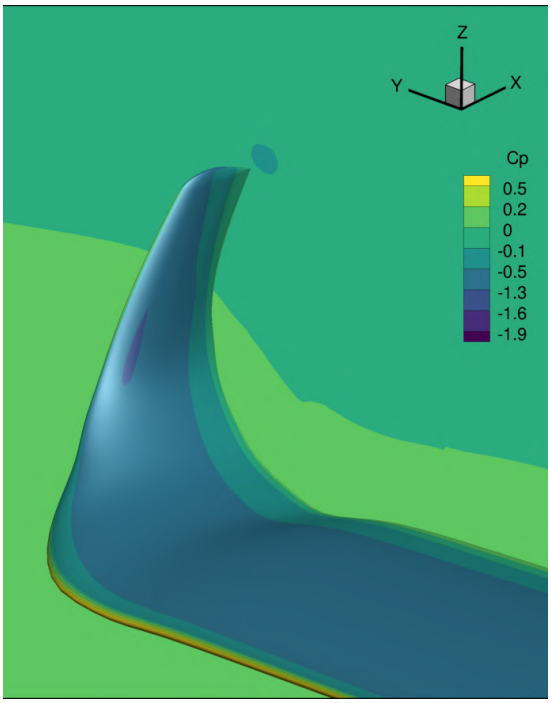

(b) Optimized winglet.

Figure 3.11: Coefficient of pressure distribution at the winglet.

Chapter 4

Strutural Analysis and Optimization

This chapter provides an overview of Computational Structural Mechanics (CSM) and introduces the TACS framework for structural analysis and optimization. It highlights the possibility of composite material properties modeling for specific scenarios. A demonstration of structural optimization of the baseline TEKEVER AR5 wing is provided. It is a follow-up to the comprehensive research found in [13].

4.1 Computation Structural Mechanics Overview

Computational Structural Mechanics is a field that models the behavior of solid structures using numerical methods. Obtaining exact analytical solutions to the governing partial differential equations is often impossible due to the complexity of the geometric or material behavior. Therefore, numerous numerical methods have been developed to solve these equations.

The TACS uses a Finite Element Method (FEM) model [40], which helps to analyze complex systems and geometries by dividing the domain into several elements. The governing equation of the problem is then guaranteed in each element using an approximation of polynomials. The complete problem solution can be obtained by coupling all these elements together [68]. This model has been extensively used and validated for aircraft wing with composite materials, considering the elements that will be used in this work, with a maximum difference between the numerical and experimental results of approximately 20% [69].

4.2 Analysis Technique

In this work, the analysis software employed for the structural analysis and optimization is TACS [40] and it is interesting to address the main theoretical background around it.

4.2.1 Constitutive Equations

To perform a structural analysis, a computational model of the behavior of the material subjected to a given load is needed. The material may have different behaviors depending on the expected deforma-

tion. Nevertheless, the predicted behavior in this work is linear, with small deformations which can be given by the generalized Hokes Law [70],

$$\sigma_{ij} = C_{ijkl} \cdot \varepsilon_{kl} + \sigma^0_{ij} \quad , \tag{4.1}$$

with σ the stress tensor, C the stiffness matrix, ε is the strain tensor and σ^0 the residual stress tensor. Moreover, it is known the stress vector has 6 components where 3 are the axial stress in each direction and the other 3 are the shear stress in the three directions.

Moreover, to characterize the material, it is important to consider how the material's properties change with direction. In this work, most of the materials are orthotopic as it is going to be considered a carbon fiber polymer-reinforced composite material. This is a desired material for aerospace engendering for its high specific strength, fatigue resistance, and a high degree of customization due to the variable fibers orientation [71]. The constitutive equation that relates stress and strain for an orthotopic material [70] can be written as,

$$\begin{bmatrix} \varepsilon_1 \\ \varepsilon_2 \\ \varepsilon_3 \\ 2 \cdot \varepsilon_{23} \\ 2 \cdot \varepsilon_{13} \\ 2 \cdot \varepsilon_{12} \end{bmatrix} = \begin{bmatrix} 1 & E_1 & -\nu_{21} & 0 & 0 & 0 \\ -\nu_{12} & E_2 & -\nu_{32} & 0 & 0 & 0 \\ 0 & 0 & 1 & 0 & 0 & 0 \\ 0 & 0 & 0 & G_{23} & 0 & 0 \\ 0 & 0 & 0 & 0 & G_{13} & 0 \\ 0 & 0 & 0 & 0 & 0 & G_{12} \end{bmatrix} \begin{bmatrix} \sigma_1 \\ \sigma_2 \\ \sigma_3 \\ \sigma_4 \\ \sigma_5 \\ \sigma_6 \end{bmatrix} \quad , \tag{4.2}$$

with the Young's Modulus (E_i) of direction i, ν_{ij} and G_{ij} is the Poisson ratio and the shear modulus in each plane. For the isotropic materials Young's modulus, the Poisson ratios, and the Shear modulus do not depend on the orientation, and lose the index with the G parameter given by $(0.5 \cdot E)/(1 + \nu)$. It is then necessary to know the mechanical proprieties of each material.

4.2.2 Material Characterization

In the context of conventional materials, the coefficients for the matrix are constrained by the manufacturer's specifications. In the case of a composite material, its properties depend on both the matrix and reinforcement, as well as the number of plies and their orientation. This allows for tailoring the material to specific loading scenarios, which further optimizes the system [71]. Figure 4.1 a) presents a schematic of a ply while Figure 4.1 b) shows a schematic of the composite.

Assuming that all fibers are oriented in the same direction and all parallel within a ply, each lamina can be assumed to have orthotropic behavior allowing for the theories of the rule of mixtures to be considered [73]. Assuming also a perfect bond between fibers and matrix, that the fibers are parallel and uniformly distributed, the matrix has no voids or cracks, an initial stress-free state, both the fibers and the matrix are isotropic, have a linear elastic behavior and the loads are either perpendicular or parallel to the fiber direction, the following relations of the rule of mixture are valid [73]:

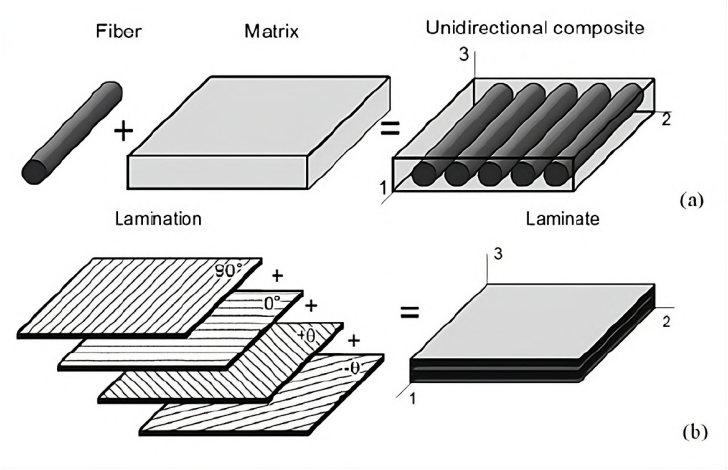

Figure 4.1: Composite material [72].

$$E_1 = E_f V_f + E_m V_m \quad , \quad E_2 = \frac{E_f E_m}{E_f V_m + E_m V_f} \tag{4.3}$$

$$G_{12} = G_{21} = \frac{G_f G_m}{G_f V_m + G_m V_f} \quad , \quad \nu_{12} = \nu_{21} = \nu_f V_f + \nu_m V_m \tag{4.4}$$

with V the volumetric fraction where subscript m describes the matrix and f the fiber.

4.2.3 Failure Criterion

Given the constitutive equation and material priorities, failure criterion is the only thing missing to fully characterize the material's behavior. The stress applied to the material is a complex 3D load that may be hard to evaluate, therefore, there is a need to simplify it with failure criteria. As an orthotropic material, the stress analysis of a structure built with composite has to take into consideration the different properties of the material regarding its direction. For an isotropic material, the most commonly used criterion is the Von Mises, however, for composite materials and their unique characteristics, the Tsai-Wu is one of the most generally used and a satisfactory option [74].

The Tsai-Wu criterion considers failure in different directions due to the orthotropic nature of plies and are given by [70]:

$$FTW = F_1\sigma_1 + F_2\sigma_2 + F_{11}\sigma_1^2 + 2F_{12}\sigma_1\sigma_2 + F_{22}\sigma_2^2 + F_{66}\sigma_{12}^2 \tag{4.5}$$

with F_{ij} experimentally determined material strength parameters obtained from the failure strength in uniaxial tension/compression and shear.

4.2.4 Finite Element Method

It is important to consider the method used for computing the stress of the material in the UAV's structure. The structure is modeled using partial difference equations, and the FEM method is used to solve them. The domain is divided into multiple finite elements to obtain the solution [68]. This

method yields the nodal displacements and rotations, degrees of freedom (DoF), in/around the x, y, and z directions and axes. The number of DoF per node may vary depending on the element formulation. Therefore, knowing that the solution is obtained per interpolation on the nodes, an increased degree of interpolation due to a higher number of nodes per element should give a more accurate solution [68].

Although real structures are 3D, in cases where thin structures like wing skin are analyzed, a simplification can be done by using 2D shell elements to model the middle plane of the skin [40]. Then a system of stiffness matrix developed for each element can be assembled allowing for the system of linear equation formulated to be solved and obtain the nodal displacements and rotations [68]. Finally, strain and stresses are computed based on the displacement field and material constitutive laws.

The TACS software used in this work has three types of elements: higher-order shell elements for linear analysis in the integrated framework, 2D quadrilateral higher-order plane stress elements, and 3D hexahedral elements for both geometrically linear and non-linear analysis [40]. The shell elements take into account the bending effects of the shell as they incorporate the rotation Degree of Freedom in their nodes [69]. Figure 4.2 presents the 6 degrees of freedom mentioned for a typical shell element.

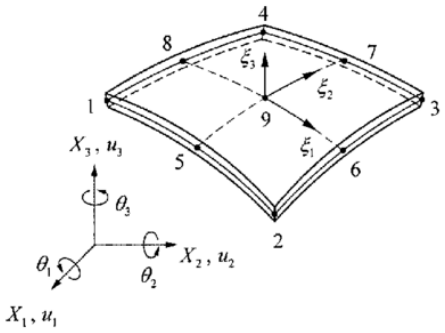

Figure 4.2: Typical 6 DoF shell element [75].

As the wing box is composed of shell structures like the skin and the ribs, shell elements are expected to be used in the analysis [69]. However, it is important to note that, these elements are not suitable for structures with high thickness and curvature radius.

4.2.5 TACS

The TACS software is used to perform structural simulation, being interesting to understand the main caracteristics of the structural solver employed. TACS, the Toolkit for the Analysis of Composite Structures, is a parallel computing framework used for large-scale, gradient-based design optimization of high-performance structures, especially in aerospace engineering. It helps solve complex structural design problems. These problems often involve a large number of design variables, state variables, and load cases. A key feature of TACS is its use of the adjoint method to evaluate gradients for design optimization. This method works well even when there are many design variables, ensuring that it scales effectively with large problems [40].

TACS is known for its near-ideal scalability, meaning it performs efficiently as the number of design

variables, constraints, and processors increases. This is important for high-fidelity structural design optimization, especially when working with large, complex models. The framework is also highly accurate when calculating gradients because it uses hand-coded derivative routines rather than other methods. This approach avoids common numerical issues and ensures computational efficiency [40].

Additionally, TACS handles constraints like material failure with advanced formulations. It also uses aggregation techniques that reduce the number of constraints without sacrificing accuracy, making the optimization process more efficient [40].

4.3 Implementation

The implementation of the structural optimization follows the steps shown by the flowchart in Figure 4.3.

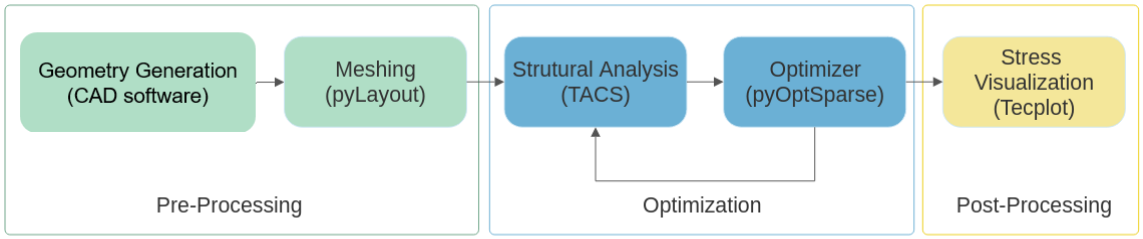

Figure 4.3: Flowchart of the structural optimization framework.

Theses steps are briefly described next.

4.3.1 Geometry Definition

The first step in the analysis is to define the geometry to be analyzed. Specifically, TACS should be provided with information on the node's location, element identification, and the type of elements used.

The process followed to generate the mesh could go through a commercial code or pygeo, the aim is just to create a geometry that will limit the space where structural mesh will be projected and constructed.

4.3.2 Mesh Generation

The generation of a mesh involves a systematic process utilizing the Python package pyLayout. This particular Python module is tailored for the automated creation of parametric structures for wings. By providing a description of the structural layout, pyLayout constructs a finite-element model for a wing-box, reproducing the structural attributes of an actual wing. The requisite description number and position of ribs and spars, and skin. Optional parameters include the order of elements for finite elements, the number of elements span-wise between each rib, the number of elements chordwise between each spar, the count of elements in the thickness, or specifics about the number and arrangement of apertures in ribs, spars or skins [76].

4.3.3 Constraints Formulation

Structural constraints are necessary to limit the maximum allowable stress and strain in a given structure. However, creating a separate constraint for each stress computation point is not practical or computational feasible as would lead to a giant number of contraints and a very expensive adjoint computation. Similarly, constraining only the maximum stress value can lead to problematic optimizer behavior due to the discontinuity in the derivative of the max function. To solve these challenges, TACS offers the constraint aggregation techniques Kreiselmeier-Steinhauser (KS). this technique aims to provide a smooth, differentiable approximation of the maximum value across a set of functions [35]. As a user-defined parameter, a small KSWeight will make the KS function smoother but will also lead to overprediction of the maximum value when there are many large values while using a high value has the opposite effect, the TACS default value is used, as no problems were found with it.

In addition to the base version of the TACS, several constraints were added, as described by [13], to improve manufacturability and make the design more practical. These constraints include an orthogonal plies constraint, which allows the use of cheaper carbon fiber cloth, making the design more cost-effective. A monotonic thickness constraint was also introduced to ensure a consistent thickness throughout the structure, which not only prevents weak points from fiber discontinuities but also reduces the search space, making optimization more efficient. Finally, a tip torsion constraint was added to control the torsion at the wing tip, aiming to achieve a more desirable aerodynamic response. Together, these constraints help ensure the final design is both structurally sound and feasible to manufacture.

4.4 Wing Structural Geometry and Material

In this section, the initial structure of the wing is presented along with the grid independence study. The main roles of the wing structure are to transmit and resist the applied loads, to maintain the aerodynamic shape, and to protect the payload and systems.

The wing geometry of an aircraft is made up of several components that work together to provide rigidity and strength as represented in Figure 4.4. One of the most important components is the spars, which help to provide bending and torsion rigidity to the wing. This component works in conjunction with the skin of the wing to resist shear stress. Ribs are also used to shape the wing and to prevent buckling, which can be a significant problem due to the thinness of the outer skin. Skin is also important to resist the shear stress felt during the flight [77].

In this work, the structural design variables, that define the wing geometry to be analyzed, are going to be the material properties and their thickness in each section of the wing as represented in Figure 4.4.

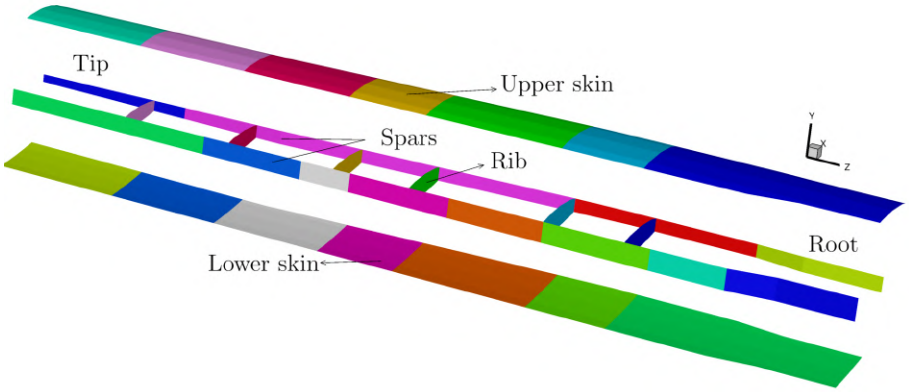

Figure 4.4: Structural section of the wing.

The material will be characterized by a composite sandwich that consist of three layers of dissimilar materials: two stiff Carbon Fiber Reinforced Polymer (CFRP) outer faces and a lightweight core material, as shown in Figure 4.5. This combination of materials provides a balance of stiffness, strength and weight that is ideal for aerospace applications [78]. The material's properties controlled by the optimizer includes the fiber's orientation (θ_i) and the total material thickness, with the fraction of each layer (core and outer layer) fixed.

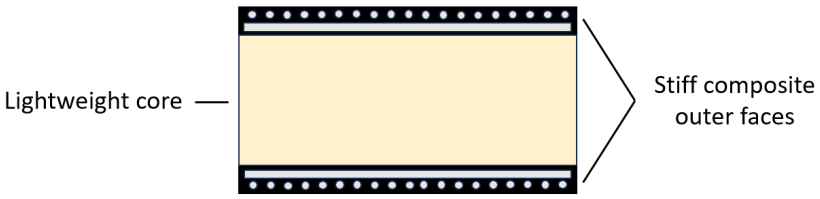

Figure 4.5: Schematic of a sandwich material.

The ratio of CFRP to foam of each component can be found in Table 4.1, considering the span wise direction z.

Table 4.1: Quantity of CFRP (%) in each structural component.

	CFRP(%)
Front spar (0m $\leq$z$<$ 0.5m)	33
Front spar (0.5m $\leq$z$\leq$ 3.62m)	100
Rear spar (0m $\leq$z$<$ 0.5m)	6
Rear spar (0.5m $\leq$z$\leq$ 3.62m)	100
Ribs	6
Skin	20

It is important to highlight that for the core, only the in-plane properties were required because transverse stress is disregarded in the first-order shear deformation theory for laminated plates. Consequently, as the in-plane properties of the foam core are directionally independent, the material can be treated as isotropic. The material proprieties for the Airex foam can be found in Table 4.2, where the spars, ribs and skin are correspondingly constituted by Airex C70.75, C70.90 and C70.55, respectively.

Table 4.2: Airex properties required for TACS [13].

Material	Airex C70.55	Airex C70.75	Airex C70.90
Density [kg m^{-3}]	60	80	100
Tensile modulus in the plane [MPa]	45	66	84
Shear modulus [MPa]	19	26	35
Tensile strength in the plane [MPa]	1.3	2	2.7

For the shell, a CFRP is used with plies of 0 ^{o} and 90^o orientation.

The required material properties for the strutural analysis can be found in Table 4.3, where the density and Young's modulus were obtained from the mix rule.

Table 4.3: CFRP ply proprieties required for TACS [13].

Density[kg m^{-3}]	1483
Young's modulus (fibre direction)[GPa]	127.8
Young's modulus (transverse direction)[GPa]	6.1
Shear modulus [MPa]	3.93
Poisson ratio	0.37
Tensile strength (fibre direction) [GPa]	2.86
Compressive strength (fibre direction)[GPa]	1.45
Tensile and compressive strength (transverse direction)[MPa]	81
Shear strength[MPa]	136

The change in thickness of the different components mainly derives from a change in thickness of the foam and not necessarily of the CFRP shell, since the core has the largest fraction (over 80% for the majority of components).

Moreover, in order to complete the model for the subsequent static analyses, constraints must be applied. The wing root was considered to be clamped, meaning that the nodes in the root plane had their degrees of freedom for both translation and rotation set to zero.

4.5 Wing Structural Grid

The grid independence study was performed in [13] and the main process will be presented here. First, it is important to mention that, as shown in Figure 4.5, the mesh will cover 6 ribs, upper/lower skin, and 2 spars. Due to these components being thin and made with composite materials, 2D shell elements were used for the mesh with 4 and 9 nodes quadrangular ones. The mesh structure is represented in Figure 4.6 .

Like with all mesh independence studies, the objective is to find a mesh where the solution has converged with the least time possible. In this study, the displacement of the mesh in the tip of the wing, and the maximum stress were analyzed.

It is important to mention that no performance benefits were observed using one element over the other for the converged mesh. Despite both elements' mesh converges, the bi-linear one presented a better behavior approximating that point with no oscillations and for that reason was selected. In that way, the most efficient mesh had 145,408 elements with 870,948 DoF with bi-linear elements, which

presented a small difference of 2.7% on the stress and 0% of the displacement of the tip of the finer one, in 1.93 less time.

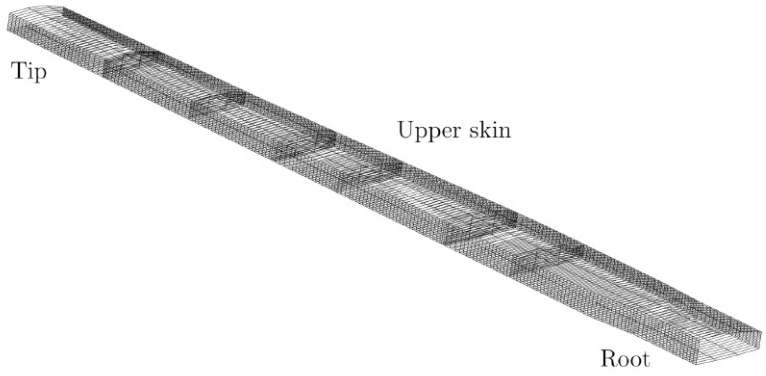

Figure 4.6: Structural mesh.

4.6 Wing Structural Optimization

A demonstration of the structural optimization of the TEKEVER AR5 wing will be presented next.

4.6.1 Problem Statement

The structural optimization aims to reduce the wing weight, W, while maintaining the general aerodynamic shape and structural integrity through the flight envelope (1g and 4g), sustaining the aerodynamic forces (obtained from ADFlow and scaled) and the structure's weight.

To perform the structural optimization of the wing, it is necessary to implement some constraints. Therefore, it is imposed: material failure constraint, $KS(failure)$; Vertical displacement below 12% $KS(displacement)$; Adjacency constraints, to keep the difference in each design variable, $|t_i - t_{i+1}|$; Ply angle continuity, each consecutive material ply angle should be equal for the sake of manufacturing, $\theta_{1,i} = \theta_{1,i+1}$ and $\theta_{2,i} = \theta_{2,i+1}$; Orthogonality between plies to allow the use of carbon fiber cloths with a weaving pattern, $\mid \theta_1 - \theta_2 \mid = 90°$; And maximum torsion for the wing tip.

The design variables nd their bounds can be found in Table 4.4.

Table 4.4: Wing structural variables.

Variable	**Bounds**
Skin and Ribs Thickness	1 mm to 100 mm
Spar Thickness	0.33 mm to 100 mm
Ply Angle	$-90°$ to $90°$

Finally, the complete problem can be defined in standard form as:

$$
\begin{aligned}
\text{minimize} \quad & W \\
\text{with respect to} \quad & \theta_{i,j},\ t_{i,j} \\
\text{subject to} \quad & KS(\text{failure}) \leq 1/(n) \\
& KS(\text{displacement}) \leq 0.13 \ @4g \\
& |t_i - t_{i+1}| \leq \Delta_{\text{max}} \ @4g \\
& t_i - t_{i+1} \leq 1 \\
& \theta_{1,i} = \theta_{1,i+1} \\
& \theta_{2,i} = \theta_{2,i+1} \\
& |\theta_1 - \theta_2 \,| = 90^\circ \\
\gamma < \gamma_{max} \quad .
\end{aligned}
\tag{4.6}
$$

4.6.2 Minimum Mass Wing

Considering the wing of the TEKEVER AR5 as the starting geometry, the structural optimization was performed and a mass reduction of 43.6 % was found after 70 iterations. The resulting geometry is represented in Figure 4.9 with its thickness distribution. It is interesting to notice the original wing box design is quite oversized, with the safety factor rounding a maximum of 0.2 in the root of the wing. Moreover, it is also possible to see that the failure index is not continuous throughout the wing discontinuities, as panels are divided into sections, despite the continuity constraint present in the problem.

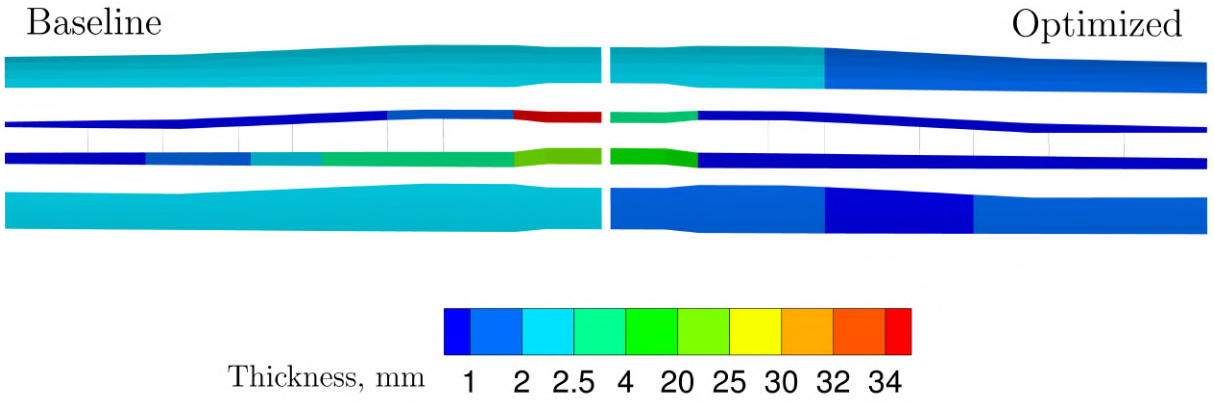

Figure 4.7: Comparison between the baseline and optimized wing panel thickness.

Across the results, it is possible to identify the different constraints activated in the design variables and structure evaluation criteria. According to Figure 4.8, the displacement constraint is active and the maximum allowed displacement occurs in the y-direction at the tip of the wing with a normalized deflection of 0.13 as seen in Figure 4.8 as well as the original wing deflection. It is possible to see that the value is above the constraint line, nevertheless,that does not mean that it is violated, since the function that enforces it, computes the average displacement of the last skin an spar section, therefor, the maximum tip deflection is going to be higher than ht average.

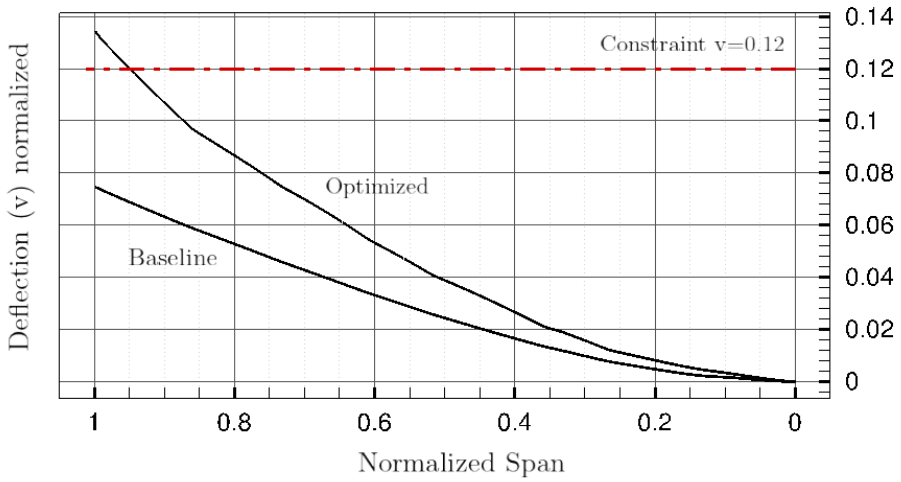

Figure 4.8: Normalized displacement of the wing box in the y direction.

To balance this and the higher lift force closer to the center of the wing, the optimizer prioritizes not decreasing as much the thickness of it near the root (Figure 4.7). Nevertheless, a manufacturing decreasing thickness constraint was established to guarantee a uniform thickness decrease as can be seen in Figure 4.7. In this context, it is pertinent to emphasize that the wing skin serves as the most effective means of reinforcing the structure against bending forces. The optimizer increased its thickness compared to the original wing, despite it already being structurally oversized. Overall is possible to see that the mass reduction happens mainly in the wing skin close to the wing tip, despite the increase in the root.

Looking into Table 4.5 of the DV ply angles, several manufacturing constraints can be highlighted. The different DV regions(Upper and Lower skin, Front and Rear spar) are condensed in a single value, as the ply angle constraint for ease of manufacturing forces it. Moreover, the imposition of unidirectional fiber cloths is also satisfied and the difference in ply angle is 90°. Furthermore, it is noted that the rear spar experiences the maximum change in ply angles (19%) during optimization. This adjustment ensures that as, the wingbox deforms over time, the alignment with the fibers is maintained, enabling the most efficient usage of material.

Table 4.5: Optimized ply angle.

	Range	Upper skin	Lower skin	Front spar	Rear spar
θ_1	0-90°	87.2°	90.0°	87.1°	73.1°
θ_2	0-90°	-2.7°	0.1°	-2.9°	-16.9°

Since is not possible to determine in TACS the aero-elastic phenomena, a maximum increase in tip torsion of 20% relative to the baseline case constraint is added to force an increase in stiffness and delay the divergence effect.

The ribs' thickness was noticeably reduced to their minimum allowable dimensions in each section, as seen in Table 4.6. Since the primary aim of these ribs is to counteract the buckling effect, the inability to predict and constrain this phenomenon partially explains the overly optimistic outcome.

Table 4.6: Optimized ribs geometry.

Ribs	Range	1 (Root)	2	3	4	5	6
θ_1	0-90°	90.0°	88.7°	89.9°	90.0°	89.1°	89.7°
θ_2	0-90°	0.0°	-1.3°	-0.1°	0.0°	-0.9°	-0.3°
Thickness [mm]	1-100 mm	1.0	1.0	1.0	1.0	1.0	1.0

Moreover, the utilization of the law of mixtures to model the material priorities of the sandwich material raises some doubts, as it relies on theoretical constructs rather than empirical data.

Finally, from figure 4.9, it is possible to conclude that the failure inequality constraint remained active if a safety factor is introduced despite all other constraints, having a maximum value of 0.6 near the root representing a 200% increase from the baseline.

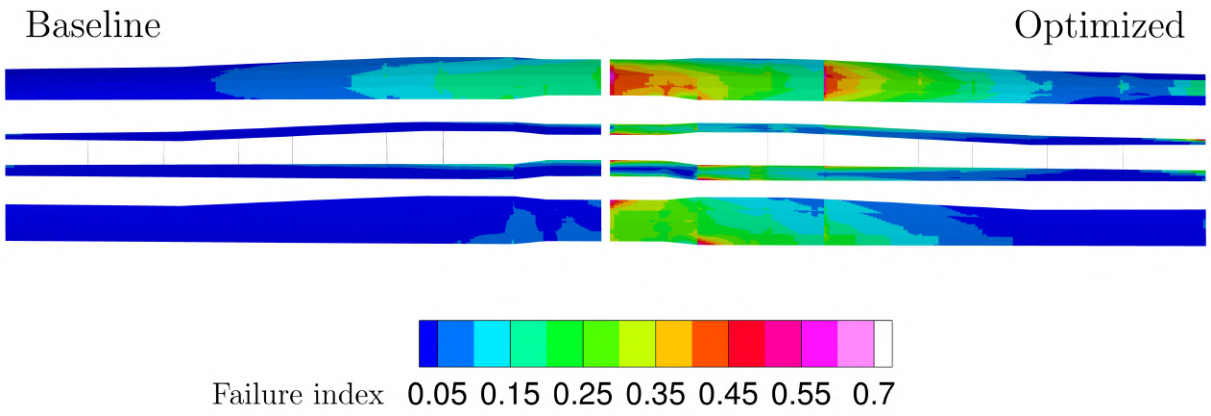

Figure 4.9: Comparison between the baseline and optimized wing failure criteria.

Chapter 5

Aerostructural Analysis and Optimization

This chapter begins with an introduction to the aerotrutural solver and its set up, followed by an interpretation of the output from the aerostructural analysis, and concludes with the setup and execution of the optimization process of the simplified TEKEVER AR5.

5.1 Implementation

The implementation of aerostructural optimization follows the steps shown in Figure 5.1.

To perform an aerostrutural analysis, it is necessary to obtain the aerodynamic and structural performance of wing, which were the main points discussed in Chapter 3 and 4. Therefore, the UAV geometry, basic characteristics and the aerodynamic and structural meshes needed for this work were already presented.

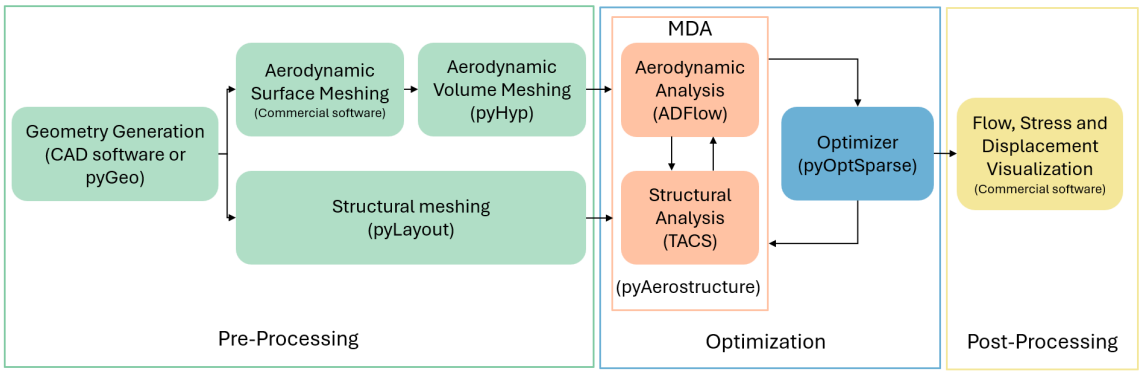

Figure 5.1: Aerostructural optimization framework flowchart.

Figure 5.2 presents the XDSM diagram of the aerostructural optimization with MACH-Aero. The general process corresponds to the implementation of the methods described in Section 3.2.2. It begins with an initial aerodynamic surface mesh and corresponding rigid links, followed by the aerostructural

analysis. This analysis is characterized by a series of iterations between the structural and aerodynamic solutions until a converged solution is reached, where the aerodynamic forces no longer deform the structure, and the structural deformations no longer affect the aerodynamic response. After that, the state variables of the solution are used to compute the coupled adjoint system of equations and the corresponding total derivatives of the objective and constraint functions with respect to the structural and aerodynamic design variables. The optimization algorithm is then run, indicating new values for the structural and aerodynamic variables, which are adjusted by the respective MACH modules: pyGeo modifies the surface through the FFD mesh, which is used by IDWarp to modify the general volume mesh; and TACS adjusts the perceived thickness and ply angles of the material, ultimately producing new structural and aerodynamic meshes to be fed into the aerostructural analysis handled by the pyAeroStruct module. This optimization loop continues until all constraints are satisfied and the optimizer convergence criteria are met.

Moreover, for an aerostrutural analysis, the loads and displacements must be transferred between the structural and aerodynamic mesh being that job performed by rigid links that after the application of some damping, transfers the displacement. Through these points, the forces are also transferred. In Figure 5.3 displays the structural mesh, the aerodynamic shape and the rigid links for the TEKEVER AR5 simplified wing and structure. This rigid links are computed by the shape functions of TACS.

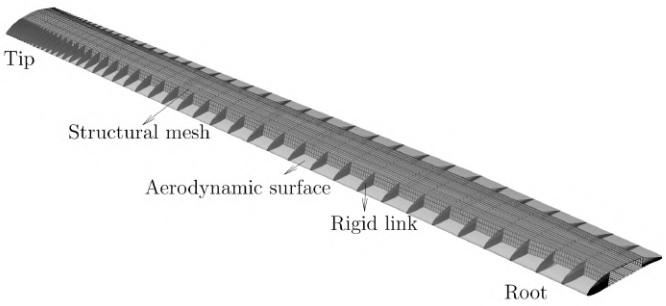

Figure 5.3: Overlay of the sructural mesh, aerodynamic surface and rigid links.

5.2 Aerostructural Simulation

The primary setup option utilized in the aerostructural solver are listed in Table 5.1.

Table 5.1: Aerostructural solver parameters.

MDA Solver	Gauss-Seidel
Max Number of MD Iterations	50
Convergence of the MDA	10^{-5}
Dumping structural displacement	0.1
Adjoint Solver	Krylov subspace approach
Convergence of the MDA sensitivity	10^{-5}

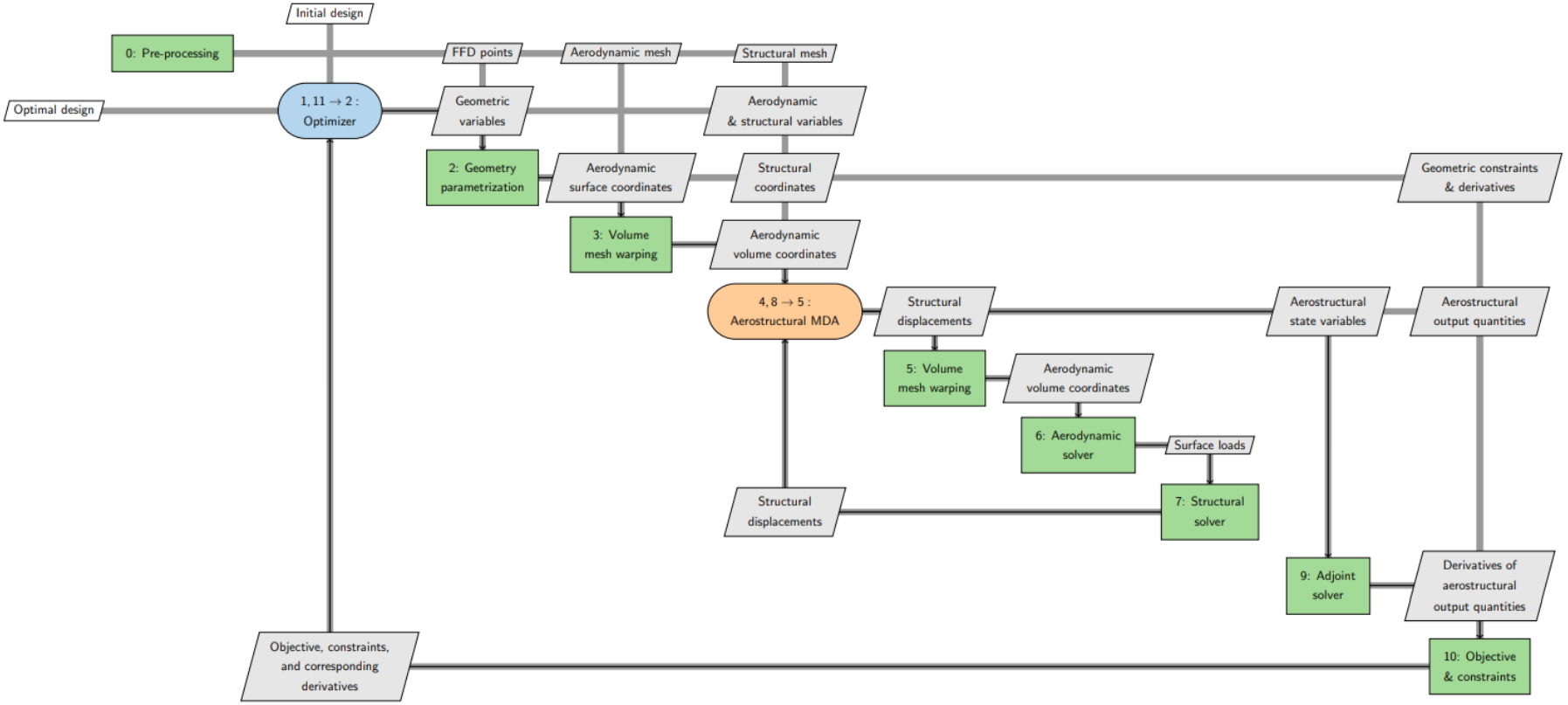

Figure 5.2: XDSM diagram of aerostructural optimization with MACH-Aero [79].

As discussed in Section 2.3, it was decided that the Gauss-Seidel method was the preferred option but not necessarily the fastest option.

The effect of the MDA convergence was studied, with the results summarized in Figure 5.4.

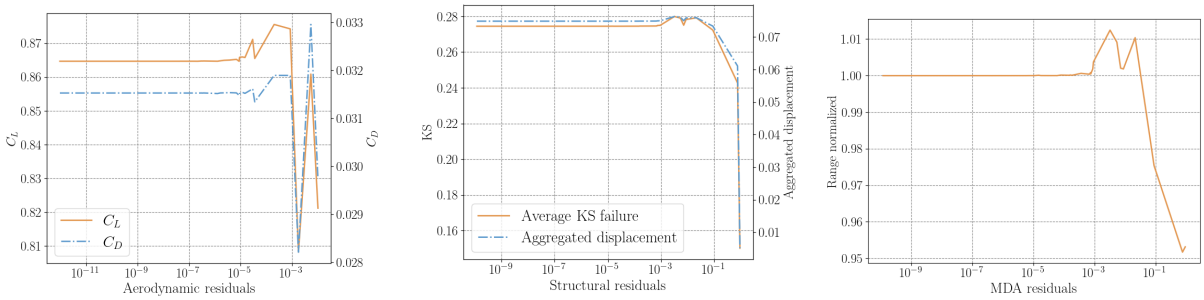

(a) aerodynamic component. (b) structural component. (c) coupled response (Range).

Figure 5.4: Effect of MDA residual convergence tolerance.

It is possible to confirm the suitability of the chosen value of 10^{-5}, that sits in the advised range from 10^{-6} to 10^{-3} [38]. Furthermore, the maximum number of iterations was set high enough (50) to ensure that, within the observed realm of analysis, the stopping criterion would be the solution convergence.

The structural damping factor is applied to the deformation computed by the structural solver when deforming the mesh. It is adjusted automatically, so its value is only used in the first iteration. To prevent failed meshes, a small value is used initially. It was observed that the first aerodynamic mesh always had negative volumes for values greater than 0.2.

The Krylov subspace approach was selected for the adjoint solver, as it converged significantly faster than the Gauss-Seidel method for the TEKEVER AR5 wing, taking only 1/27th of the time. This approach is also recommended in [38] and, being Newton-based, it typically converges more quickly, when it does, however, as worked with already converged MDA solution this did not reveal as a problem.

Finally, the convergence of the sensitivity was chose to match the response that was obtain in the analysis convergence.

5.3 Wing Aerostrutural Analysis

To perform aerostructural optimization, aircraft requirements and performance metrics must be defined. One key metric is the aircraft range, R, the maximum distance it can travel without refueling, which can be calculated using the Breguet equation,

$$\mathrm{R} = \frac{L}{D}\frac{\eta}{sfc \cdot g}\ln\left(\frac{W_0}{W_f}\right), \tag{5.1}$$

where the lift L and drag D depend on the aerodynamic performance, and the initial W_0 and final W_f weight depend on the structural performance. The aircraft velocity is prescribed by the flight operating condition, the engine efficiency η and specific fuel consumption sfc are frozen given the propulsion system, and g is the gravitational acceleration.

Frist of all, it is important to aerostructurally characterize the initial TEKEVER wing. The aerodynamic shape comparison between the rigid and elastic models is illustrated in Figure 5.5, reinforcing the strong fluid-structure interaction where it is possible to see a deflection of 3.3% of wing span under cruise condition and 6.6% during 2g maneuver showcasing, the structural analysis effect on the aerodynamic surface.

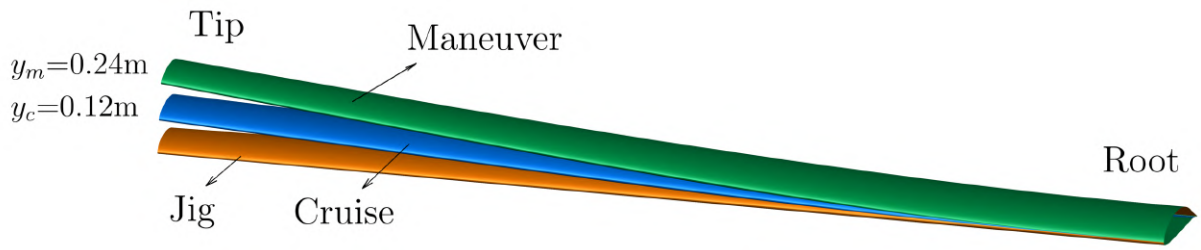

Figure 5.5: Simplified wing jig, cruise and maneuver shape.

The lift coefficient C_L as a function of angle-of-attack α of the simplified AR5 wing without the winglet is shown in Figure 5.6a, for both the rigid model (aerodynamic analysis using the wing jig shape) and the elastic model (aerostructural analysis) the full wing characterization is also presented in that Figure. The wing deformation in the aerostructural analysis results in a change of its aerodynamic shape and incidence angle, causing an slight increase in lift for high angles-of-attack, delaying the stall condition as seen in Figure 5.6a.

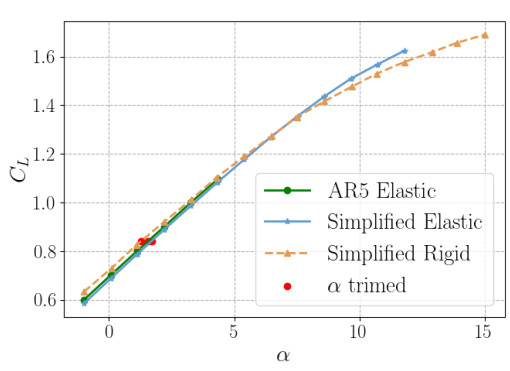

(a) Lift coefficient as function of AoA

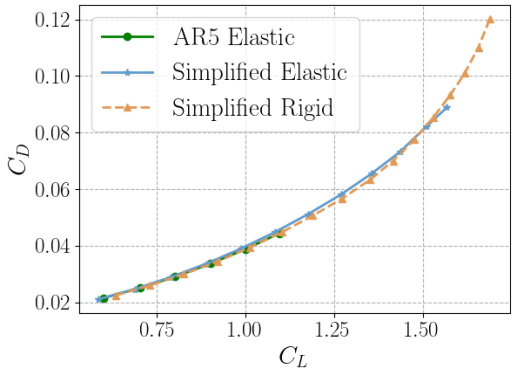

(b) Drag coefficient as function of lift coefficient

Figure 5.6: Wing aerodynamic performance.

Additionally, it also highlights that there is an negative bending-twist behavior in the baseline wing. Furthermore, it is possible to observe the wing C_L linear behavior of the elastic wing until 8° with an $C_{L\alpha}$ of 0.0892 $/^\circ$ in contrast to the rigid wing that present a value off 0.075 $/^\circ$ with $C_{L\alpha=0}$ of 0.687 after that the beginning of the boundary layer separation to occur and loss of linearity. Moreover, it is shown that, in trimmed condition, the actual lift produced is very similar between the simplified and full TEKEVER AR5 wing, with this condition being achieved for very similar angles of attack arround 1.68° for an lift coefficient of 0.842, as shown in Table 5.2.

Table 5.2: Wings characterization.

	Simplified rigid	Simplified elastic	AR5 elastic
Angle of attack, α ($^\circ$)	1.52	1.68	1.54
Drag, D	+0.1%	ref	-1.7%

When looking at Figure 5.6b two main conclusions may be taken. The expected increase in aerodynamic efficiency from reducing C_L, following from the simple structural optimization with reduction in weight and consequent increase in range. Further exploration of the comparison and potential results from the isolated and couple disciplines can be found in Section 5.5.4. Likewise, is possible to see a very small difference in terms of C_D for the three analyzed cases, representing a 1.7% decrease in drag when considering the full wing in relation the simplified one, which can be attributed to the effect that the wiglet has in reducing the induced drag.

Furthermore, as seen in Figure 5.7, the wingtip vortex in the wing with winglet is smaller that its counterpart causing the reduction in drag that can be determined in Figure 5.10. In the single-discipline aerodynamic optimization (Sec:3.4.2) found that most of the aerodynamic gains came from the winglet justifying the additional computational and complexity of adding it.

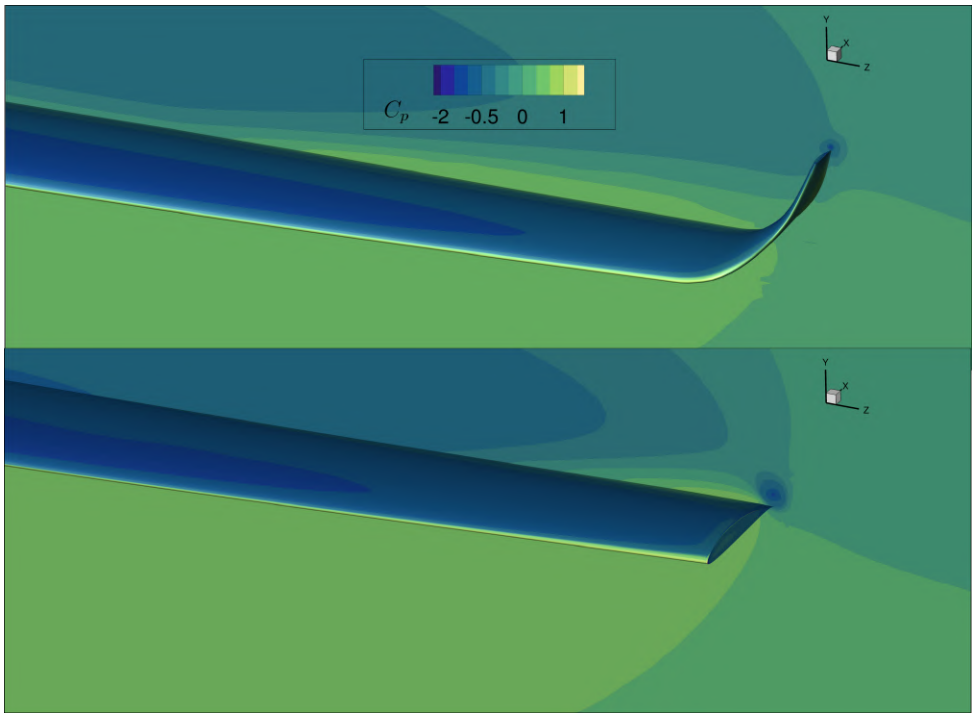

Figure 5.7: Winglet effect on coefficient of pressure.

The implications of the fuselage in the flow over the wing are also interesting to study, and influential on general results and flow over the wing. With that in mind the wing with fuselage shape present in Figure 5.8 were developed and tested.

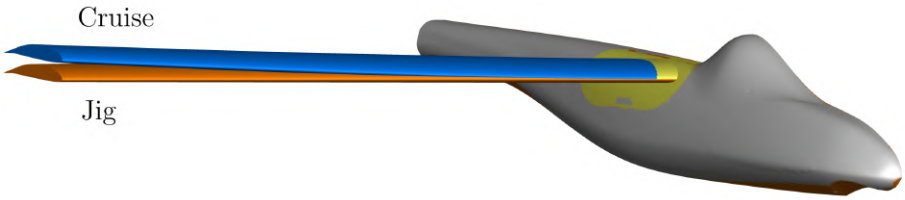

Figure 5.8: Wing and fuselage jig and cruise shape.

The fuselage interference is observed in Figure 5.9a, where the streamlines over the fuselage bend around the canopy, generating curvature in the ones around the root, which results in a smaller chordwise velocity of the flow around the wing root, creating a drastic 25% reduction in lift generated by the wing in that section, as seen by the normalized lift distribution in Figure 5.10a). Moreover, from Figure 5.9b, it is possible to see the drastic difference between the streamlines and C_p distribution over the wing, in fact, it is possible to observe a region with high C_p on the upper surface of the wing in comparison with the simplified wing, which leads to the lift reduction.

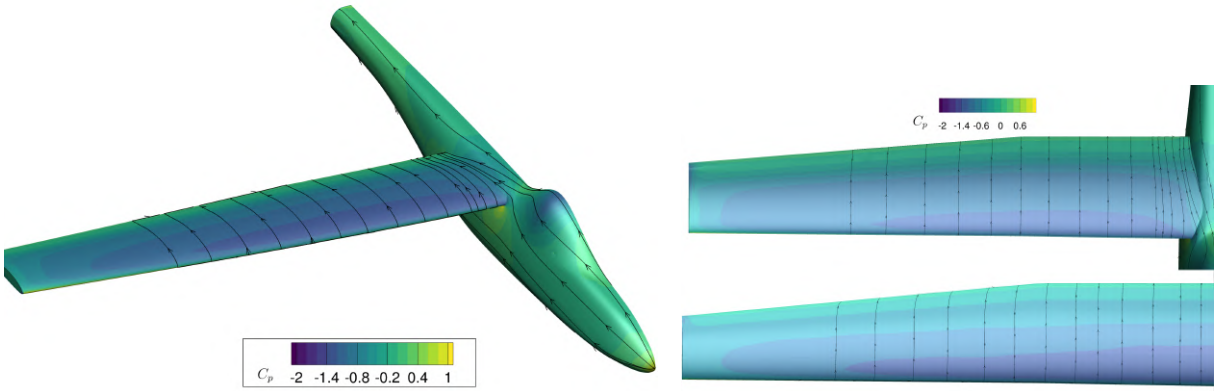

(a) Stream lines arround wing and the canopy.

(b) Effect of fuselage on stream lines over the wing and pressure coefficient.

Figure 5.9: Pressure Coefficient and streamlines around wing and canopy.

The effect previously described translates into considerable differences in the lift and drag distributions, as shown in Figure 5.10.

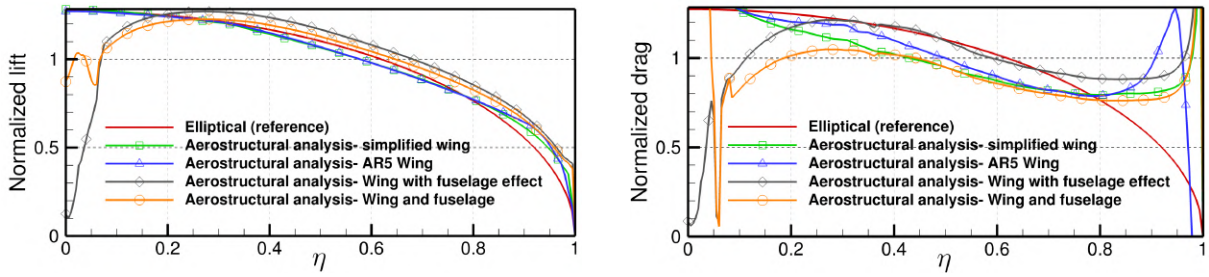

(a) Lift distribution

(b) Drag distribution

Figure 5.10: Comparison between the different fidelity levels of the lift and drag distribution.

Indeed, there is also the effect of the fuselage creating interference drag around the locking point, showcased in Figure 5.10b), As such, it would be interesting that effect could be minimized or just taken into account. There is also the reduction in lifting force in that region in relation to the simple wings analysis, that will affect the preceded optimal solution, considering that in an aerostructural analysis the wing root is of great importance, due to the expected structural discipline influence, it is awaited that the lifting force be concentrated around it. Unfortunately, due to a lack of computational power, to handle the increase in aerodynamic cost this optimization was not possible.

Finally, it is also interesting to characterize the structural response under cruise and maneuver. The initial structural characterization of thickness and material fiber orientation can be found in Figures 5.15 and 5.17. It important to salient as seen in Figure 5.11 a lack of efficiency in the structure, as shown by the very high safety factor for an maximum index failure around 0.18 for the 2 g maneuver (maximum allowed in the TEKEVER AR5 flight envelope), far away from the maximum allowable with a safety factor of 1.5 leaving a lot of room for improvement. Additionally, the generally greater thickness of the panels and spars closer to the root can be highlighted, this is the area they are more critical to due to the large bending moment generated by the wings. Can be also observed the maximum wing displacement is under 7% also leaving some room for flexing more the structure saving on material weight. The aerodynamic loads are obtained for the maneuver flight considering at cruise velocity. Moreover, it is also important to mention the twist verified in the wing tip in both loading cases of -0.2° in cruise to +1° in maneuver from the jig shape form can be explained by the greater momentum generated by the lift surface due not only to an increase in general lift but also by the shifting of the center of pressure due to the very high angle of attack verified in the maneuver condition of 15° .

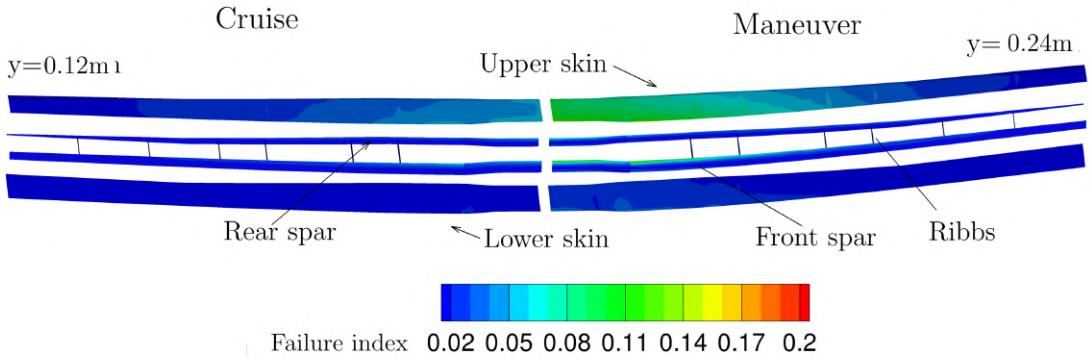

Figure 5.11: Baseline structural loading under cruise and maneuver.

5.4 Design Variables and Constraints

To perform aerostructural optimization, the wing design variables defined in Table 5.3 were used, that allow for the definition of its shape and structure.

Table 5.3: Aerostructural design variables.

Design variable	Description	Quantity	Lower bound	Upper bound	Units
α	angle of attack	1	-4	20	°
γ	twist distribution	5	-15	15	°
c	chord	6	0.5	1.5	%
b	span	1	0.5	2	%
airfoil shape	-	6x4	-0.03	0.03	m
θ_1/θ_2	fibre angle	2N	0	90	°
t	material thickness	N	0.01	0.1	m

Notice that the twist and chord distribution is a function of the wing spanwise coordinate, being defined by splines using the FFD boxes where the number of section was chosen to be the smallest possible [12]. The fibre angles and material thickness are defined for each block i of the N blocks presented in Figure 5.12.

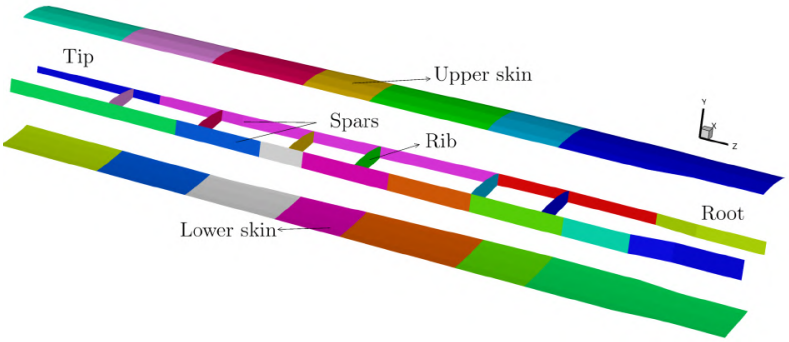

Figure 5.12: Wing structural design variables by blocks.

The design must satisfy five requirements, included in the form of constraints in the optimization: i) the trimming of the aircraft implies that the lift generated must match the UAV weight at level flight, $L = W$; the structure must not fail under a 2-g manoeuvre, $KS(failure) \leq n(2g)$;iii the structure must not deflect more than Δ_{max} ;iv) adjacency constraints to keep the difference in each design block thickness under a maximum threshold, $|t_i - t_{i+1}| \leq \Delta_{\text{max}}$; v) composite ply angle continuity among consecutive blocks for manufacturability, $\theta_{1,i} = \theta_{1,i+1}$ and $\theta_{2,i} = \theta_{2,i+1}$; vi) orthogonality between plies for manufacturability to allow the use of carbon fibre cloths with weaving pattern, $\mid \theta_1 - \theta_2 \mid = 90°$. Moreover, despite existing the capability of aerostructuraly analyze all corners of V-n diagram (velocity vs load factor) with linear structural response, it was decided to only consider maximum load maneuvering and level flight, to save on computational effort.

The wing aerostructural optimization problem is then posed in standard form as

$$\begin{aligned}
\text{maximize} \quad & \text{R} \\
\text{with respect to} \quad & \alpha, \gamma, c, b, airfoilshape, \theta_{1,i}, \theta_{2,i}, t_i \\
\text{subject to} \quad & L = W \\
& KS(\text{failure}) \leq n(2g) \\
& KS(\text{displacement}) \leq \Delta_{\text{max}} \\
& |t_i - t_{i+1}| \leq \Delta_{\text{max}} \\
& \theta_{1,i} = \theta_{1,i+1} \\
& \theta_{2,i} = \theta_{2,i+1} \\
& |\theta_1 - \theta_2| = 90^\circ
\end{aligned} \tag{5.2}$$

5.5 Baseline Wing Optimization

To obtain a better UAV wing, it is important to understand the effect that adding each structural constraint and design variable had in the final result. Finally, it is also important to compare the effect that the aerostrctural optimization with the single disciplines cases and the general aeroelastic response at critical dive speed.

5.5.1 Effect of the Manufacturing Constraints

Starting from the simplified TEKEVER AR5 wing design without winglet, a first optimization was done without the two manufacturability constraints (v) and (vi). Overall, it achieved 0.6% increase in aerodynamic efficiency and a 0.9% increase in range.

Figure 5.23 shows the convergence history of five key parameters in 275 iterations. During the initial iterations, it is clear the need to operate at higher angle-of-attack for trimming (Fig.5.13b), the reduction of (induced) drag (Fig.5.13c) by controlling the lift distribution (Fig.5.14a) with the twist angle (Fig.5.14b), and the search for a lighter structure (Fig.5.13d) while avoiding structural failure (Fig.5.13e).

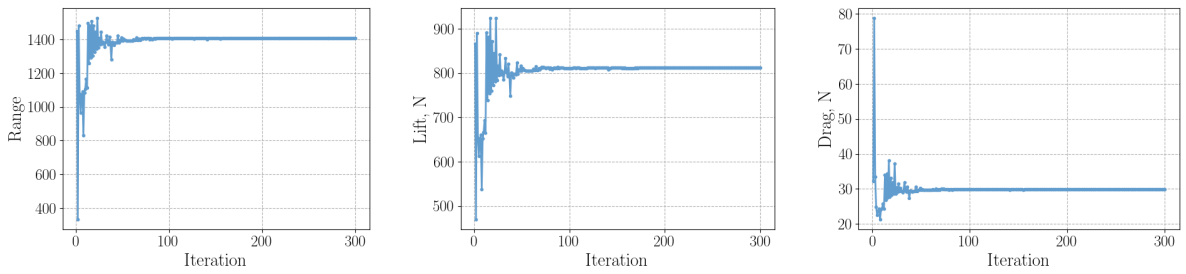

(a) Range (b) Lift coefficient (c) Drag coefficient

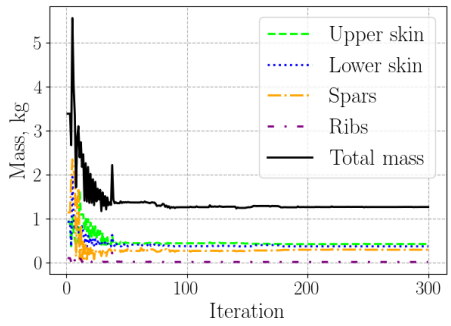

(d) Wing mass

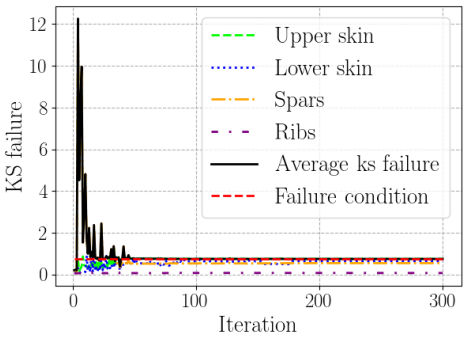

(e) KS failure

Figure 5.13: Optimization history of key parameters.

The optimal twist and lift distributions are shown in Figure 5.14. As expected, the optimizer did not to converge for the ideal aerodynamic solution (elliptical lift distribution) but rather increased the lift produced in the inner portion of the wing and reduced it closer to the tip, contributing to a more beneficial structural loading (less bending moment, thus lighter structure) and an overall better coupled aerostructural solution, this situation reveled in both the constraint and unconstrained cases that appeared with almost exactly the same lift and twist distribution.

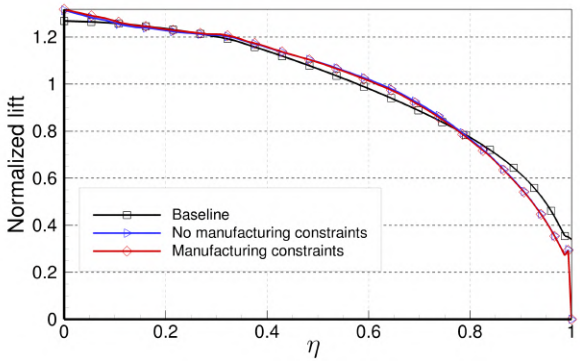

(a) Lift distribution.

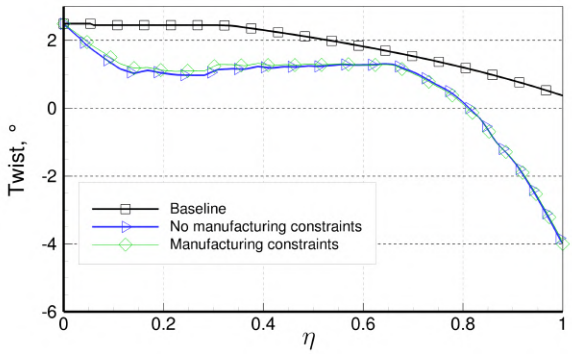

(b) Twist distribution.

Figure 5.14: Aerodynamic lift and twist spanwise distributions with and without manufacturing constraints.

This case led to a improvement of the structural efficiency, as a consequence, of a 51.9% wing weight reduction occurred due to the significant thinning of panels, observed in Figure 5.15, particularly at the front spar and lower skin panels.

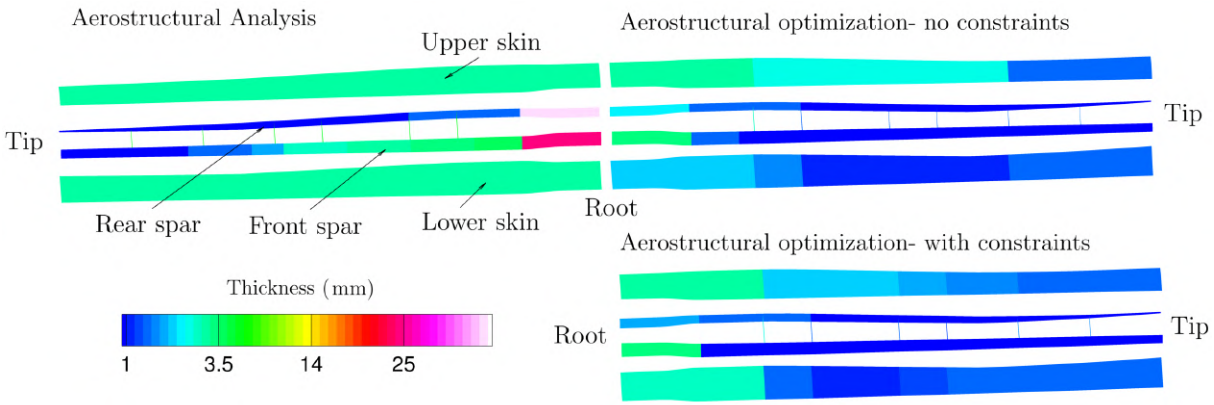

Figure 5.15: Thickness distribution with and without manufacturing constraints.

Referring to Figure 5.16, the optimized wingbox has more regions with a higher failure index, meaning that it is working closer to failure due to the overall thickness decrease, highlighting the baseline wingbox structural oversizing.

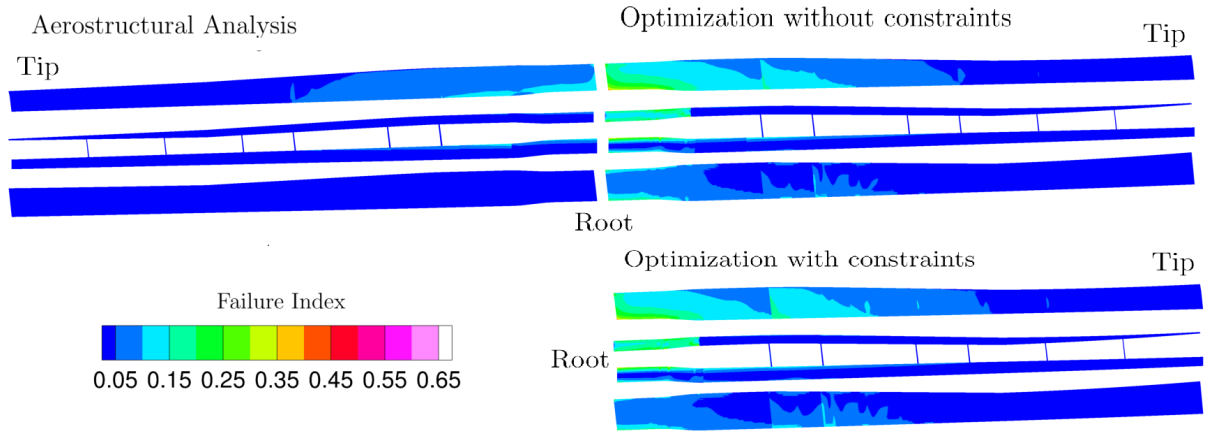

Figure 5.16: KS failure index with and without manufacturing constraints.

The ply angle distribution between the blocks is shown in Figure 5.17. It can be verified that, when the optimizer is given full freedom without the manufacturing constraints, the solution is non-monotonic distribution, which would make manufacturing difficult. Furthermore, the fact that the angle between plies is not 90 degrees makes it impossible to use standard interwoven carbon fiber, increasing the cost of wing manufacturing. To address the issues described, the manufacturing constraints of adjacency ply angles (iv) and orthogonality (vi) were added. Figure 5.17 demonstrates that the new optimal solution is now feasible in terms of manufacturing, being this solution much easier to implement with its orthogonal plies and consistency in ply angles. This change did not affect the general optimized solution and respective structural and aerodynamic response, the failure index (Fig:5.16), final tip torsion (Fig:5.15) and lift distribution (Fig:5.14a) are in dead identical. Moreover, the general thickness distribution (Fig: 5.15) is also similar, whoever a slight bump in the first lower skin panel is observed justifying the small increase in mass. Therefore with these additional constraints, the aircraft increase in range also was reduced to 0.8% gain compared to the baseline (-0.1%).

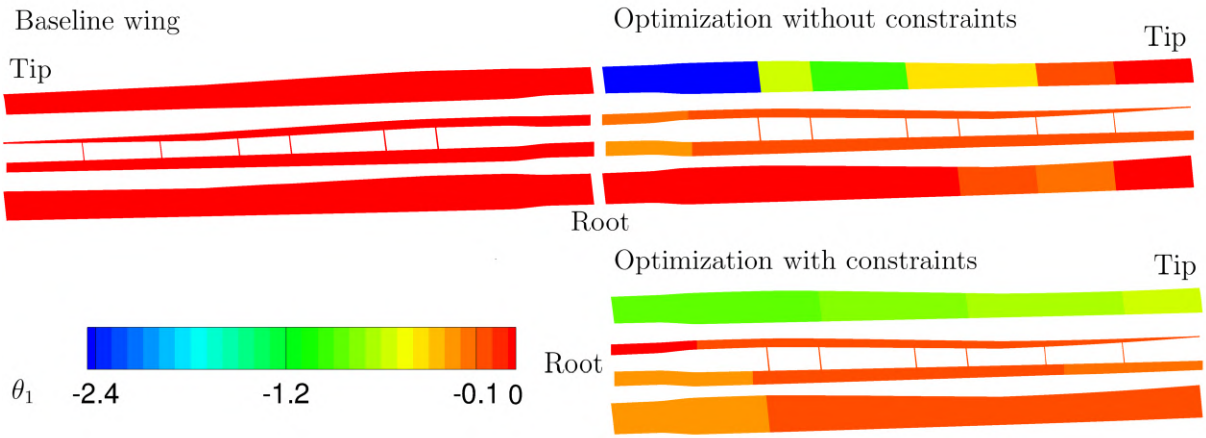

(a) Angle θ_1

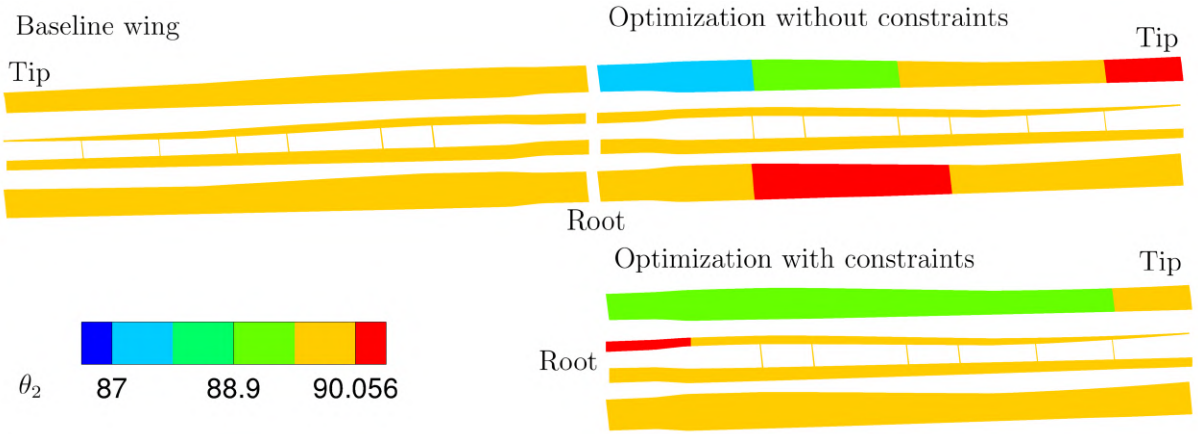

(b) Angle θ_2

Figure 5.17: Optimal distribution of ply angles with and without manufacturing constraints.

5.5.2 Effect off the Maximum Tip Deflection Constraint

Moreover,it was observed a very high deflection and tip torsion for some optimal cases. Therefore it is interesting to establish a tip vertical deflection at 0.13 normalized by the half-span as in [13] to mitigate that situation. This optimization resulted in a 4.2% increase in range from a 10.4% increase in aerodynamic efficiency at an 5° angle of attack and 43% reduction in mass. This result in the loss of 1.6% in range in relation to the not constrained case that was deem necessary to obtain an more practical solution. The wing deflection for the baseline, optimization with and without the maximum displacement constraint are depicted in Figure 5.18. Tt is possible to see that the constraint is active and allowed for a reduction in deflection from 28% of half-span to 13% as desired.

This change in deflection was achieved by a smaller than the unconstrained decrease in panel and spar thickness along the span, specially in the front spar and upper skin panel as seen in Figure 5.19.

This new thickness with a much thicker airfoil (Table 5.4) imposes a much smaller failure index along the panels reducing from a maximum around 0.45 at the optimization without the maximum displacement constraint for a more in line with the remaining cases of 0.35 (Figure 5.29). This reduction in deflection led to a structure with a much higher safety factor, as seen in Figure 5.20.

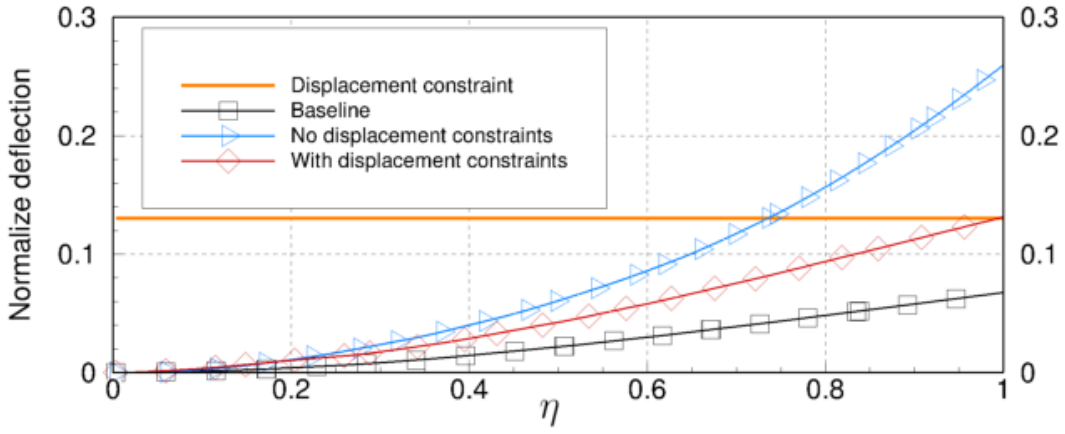

Figure 5.18: Wing deflection comparison for optimized twist, chord, and shape design variables: with and without deflection constraints.

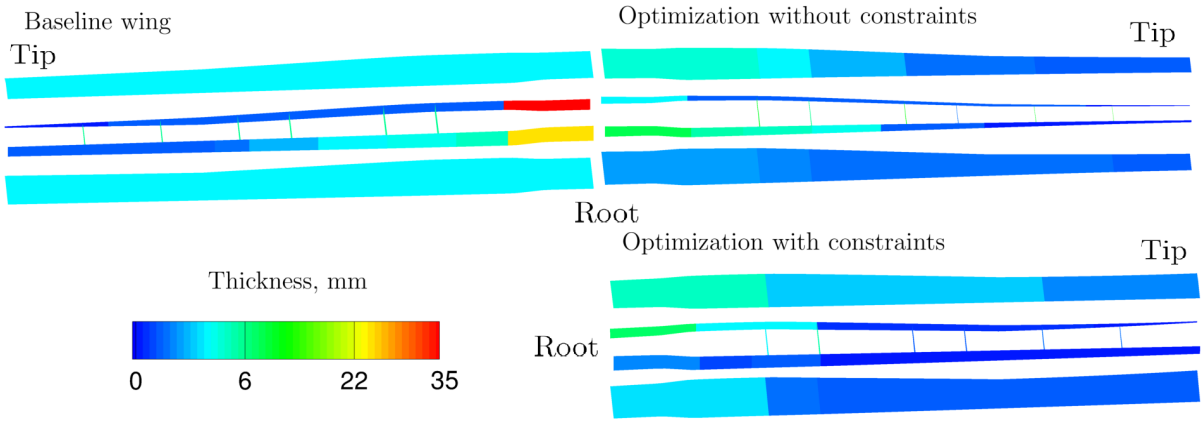

Figure 5.19: Thickness comparison for optimized twist, chord, and shape design variables: with and without deflection constraints.

During the optimization with the constraint, the general aerostructural tendency was captured as it can be seen by Figure 5.21a. In fact, the baseline solution closely follows the elliptical lift distribution, while the unconstrained case deviates significantly to reduce bending moment and mass. The constrained case, however, represents a middle ground between these two solutions. This is because the reduction in mass is less pronounced in the constrained scenario, leading the optimizer to maintain a solution closer to the aerodynamic optimum. This new solution appears much more reasonable, with positive twist near the root and downwash at the tip. This configuration helps achieve the desired lift distribution and improves resistance to aeroelastic divergence. By ensuring that the wing stall occurs first at the root, it allows for earlier detection and maintains control of the UAV through the ailerons. Finally, the chord distribution follows in Figure 5.21c a similar pattern to the unconstrained solution but on a smaller scale, allowing for mass reduction from its smaller size. This also preserves the benefits of this type of chord distribution discussed in Section 5.5.3.

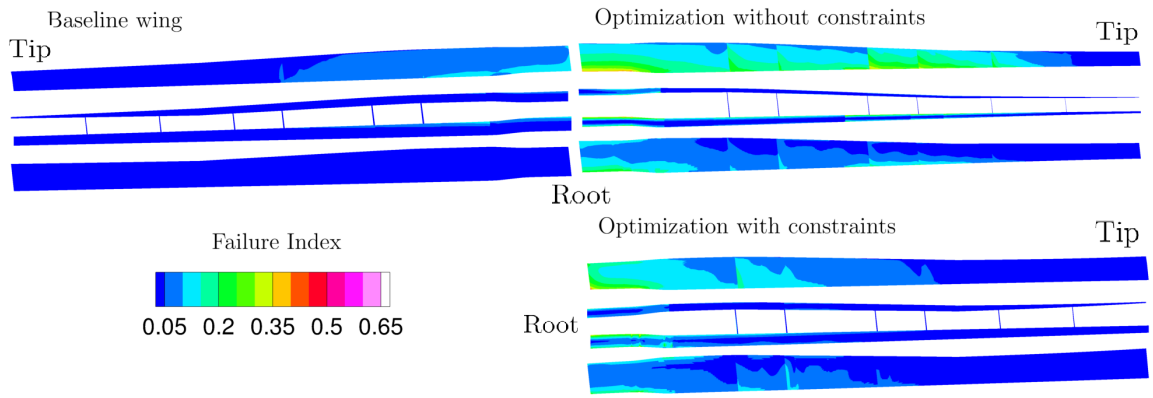

Figure 5.20: Failure index comparison for optimized twist, chord, and shape design variables: with and without deflection constraints.

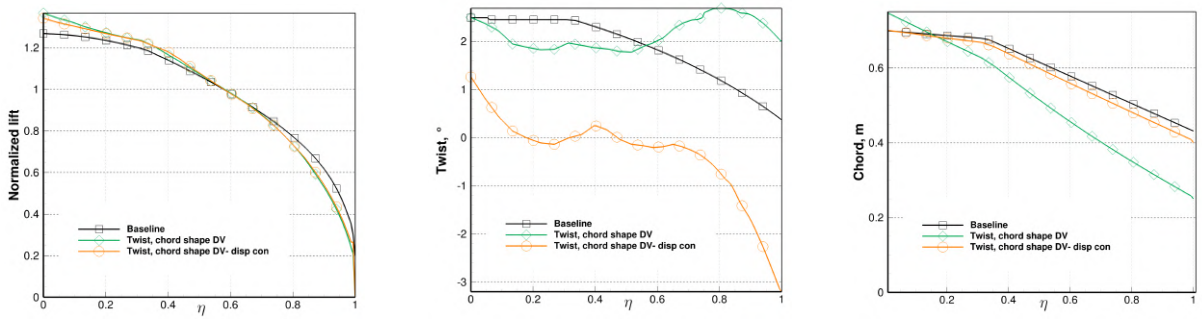

(a) Lift distribution. (b) Twist distribution. (c) Chord distribution.

Figure 5.21: Comparison of the aerodynamic parameters from the optimal solution optimized twist, chord, and shape design variables: with and without deflection constraints.

Finally, in Figure 5.22, it is possible to compare the optimal airfoil shapes obtained for the constrained and unconstrained cases. Even with a simple constraint, significant changes are observed. The airfoil becomes more symmetric and considerably thicker than in the unconstrained solution, especially near the wingtip, as shown in Table 5.4. This thicker airfoil strengthens the wing against bending moments, which drives the optimization toward a design closer to the baseline. At the root, there a small reduction of 8.1%, but at the tip, there is a significant reduction of -14.1%, benefiting from the decreased mass and drag associated with the thinner airfoil.

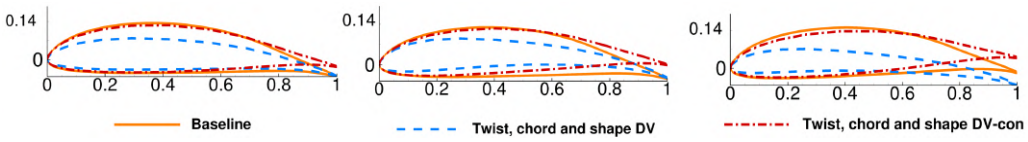

Figure 5.22: Airfoil comparison for optimized twist, chord, and shape design variables: with and without deflection constraints at 10%, 50% and 90% span.

Table 5.4: Thickness comparison for optimized twist, chord, and shape design variables: with and without deflection constraints at 10%, 50% and 90% span.

	Baseline	Unconstrained	Constrained
Thickness at 10% span	ref	-37.0%	-8.1%
Thickness at 50% span	ref	-14.1%	-9.1%
Thickness at 90% span	ref	-46.4	-14.1

5.5.3 Effect of the Aerodynamic Design Variables

Starting from the simplified TEKEVER AR5 wing design without winglet, the effect that each design variable had in the final result was studied. For that, the following combinations cases where performed: twist; chord; span and twist; shape DV; twist, chord and shape; and all DVs to fully characterize the possibilities in the design.

The first optimization was done considering only the chord distribution and angle-of-attack as design variables. Overall, a 0.9% increase in range was achieved, following a 56.6% decrease in wing mass due to the smaller skin panels and the thinner walls, with a 0.9% increase in aerodynamic efficiency.

Figure 5.23 shows the optimization convergence history of five key parameters in 93 iterations. It is clear the need for less lift for trimming (Fig.5.23b), the reduction in drag (Fig.5.23c) by reducing the lift needed and the overall wetted area, and the search for a lighter structure (Fig.5.23d) while avoiding structural failure (Fig.5.23e).

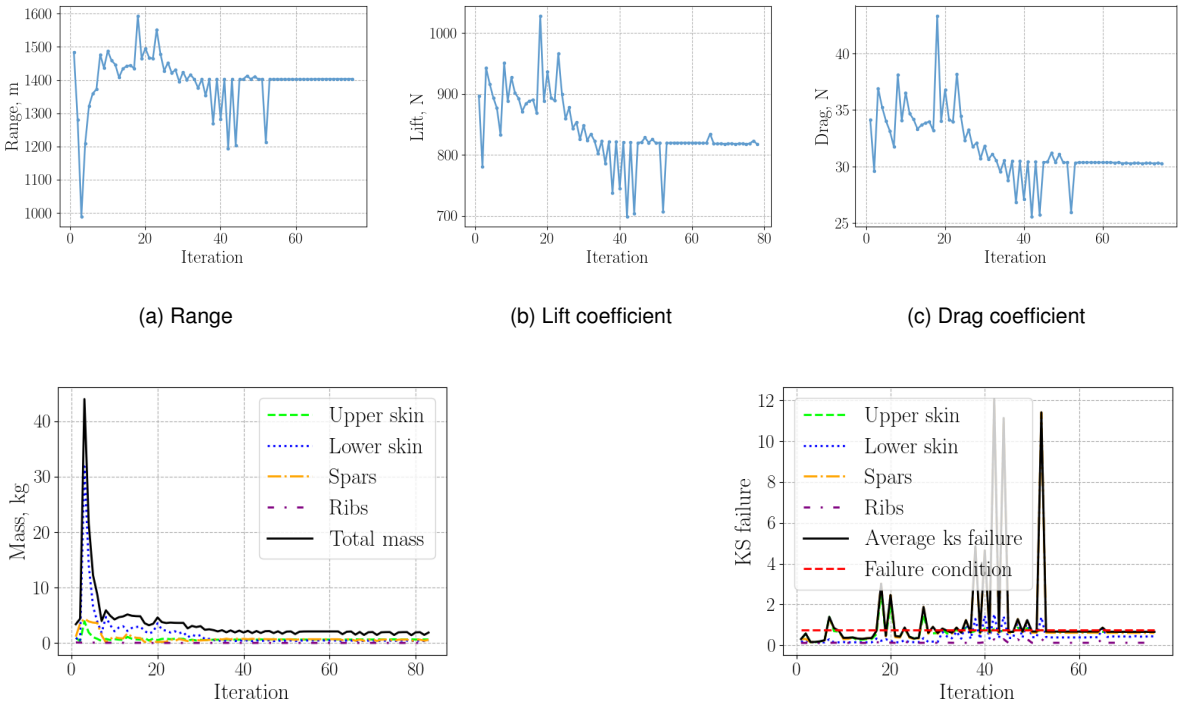

(a) Range

(b) Lift coefficient

(c) Drag coefficient

(d) Wing mass

(e) KS failure

Figure 5.23: Optimization history of key parameters in chord optimization.

The second optimization handled twist and span optimization address as the aerostrutural trade-off

between wing size and its structural weight. The optimizer converged after 282 iterations, with similar history behavior to the previous case. This case led to a 1.17m increase in wing span, which improved the aerodynamic characteristics of the wing, with a 20.9% efficiency increase.

The airfoil shape optimization was considered in the third optimization, achieving an interesting 4.5% increase in range, from a 10.6% increase in aerodynamic efficiency and 42.3% decrease in weight. This time the optimizer took 394 iterations to converge as a result of larger design space (more DVs).

As expected, the last case where all DV are considered, led to the best overall design, with 9.9% range increase, which resulted from a 32.2% improvement in aerodynamic efficiency, despite a 114% increase in wing weight, achieving a massive 1.7 times the initial span. This optimization was computationally costly, stalling and oscillating around the presented range value.

Moreover, as span variation implied drastic modifications of the whole wing design, it was also opted to perform an optimization with all design variables but the span to understand if the result obtain could reveal an interesting possibility. This case lead to 5.8% increase in UAV range from an 14.4% increase in aerodynamic efficiency 47% reduction in mass. This case also stalled.

The optimal lift distributions for all cases are illustrated in Figure 5.24.

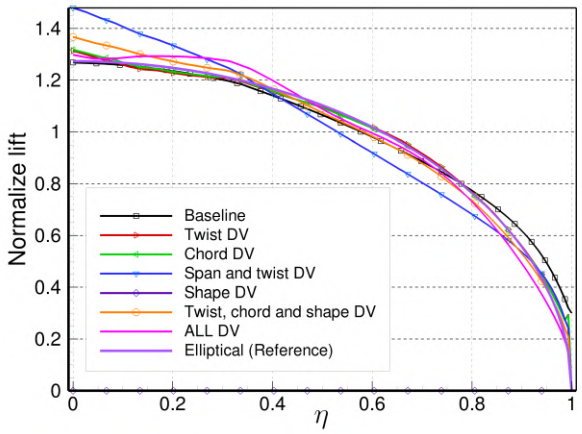

Figure 5.24: Lift distribution for each optimization case.

As expected, the optimizer did not converge on the ideal aerodynamic solution (elliptical lift distribution) for any situation. Instead, it produced a slight increase in lift near the wing root and a reduction near the tip for more efficient structural loading. That effect is seen in the all optimization, however, it is more relevant when the span is changed where it drastically increased the lift produced in the wing section closer to the root and reduced it closer to the tip, to support the increased bending moment of the arm of an larger span. However, compared with the case with more aerodynamic variables as in the all DVs case, the optimizer opted for sacrificing some of that structural efficiency in favor of a general more efficient wing. When considering the optimization with all design variables except the span, the same effect is seen but at a smaller degree. As will be discussed, this solution suffers from a very large wing deflection, benefiting from an solution with less force near the tip being the second to generate more lift near the root.

In the optimization considering only the chord DV, the primary achievement that contributed to the

increase in range was the reduction in weight, which was the strategy explored by the optimizer. With weight reduction, less lift was needed and, therefore, less wing area was required, which further contributed to the weight reduction with chord minimization as can be seen in Figures 5.25a and 5.25b where an 8% reduction in chord is seen spanwise. The reduction in lift is achieved for the shorter chord since the angle of attack is maintained, as seen in Table 5.5.

Table 5.5: Angle of attack for trimed flight in each optimization case.

Case	angle of attack, α
Baseline	1.7°
Twist	2.39°
Chord	1.72°
Twist and Span	0°
Airfoil Shape	2.25°
Twist, Chord, Airfoil Shape	2.52°
All DV	3.14°

In the remaining cases, behavior followed always the same logic of balancing the increase/decreases in chord with weight and tending to achieve a more elliptical lift distribution. In general is observed a longer chord at the root and smaller at the tip, reducing lift in the tip and increasing it closer to the root, concentrating also the wing weight in that region. Moreover, it is the expected general behavior for achieving close to elliptical distribution and the aerodynamic optimum. It is also important to note that when all design variables (DVs) are active, there is a trend toward reducing the chord across the entire wingspan. This decrease in chord helps to balance the increase in lift, minimizing area gain. Among the design variables, chord is the only one that allows for a significant reduction in weight and friction drag while lowering lift. The increase in angle of attack (Tab:5.5) that would lead to an increase in lift is balanced by the general negative twist distribution (5.26a). This reduction in chord can bring problems in the turbulence modeling predictions by lowering the local Reynolds number, decreasing the validity of the initial assumption that all the wing would be turbulent.

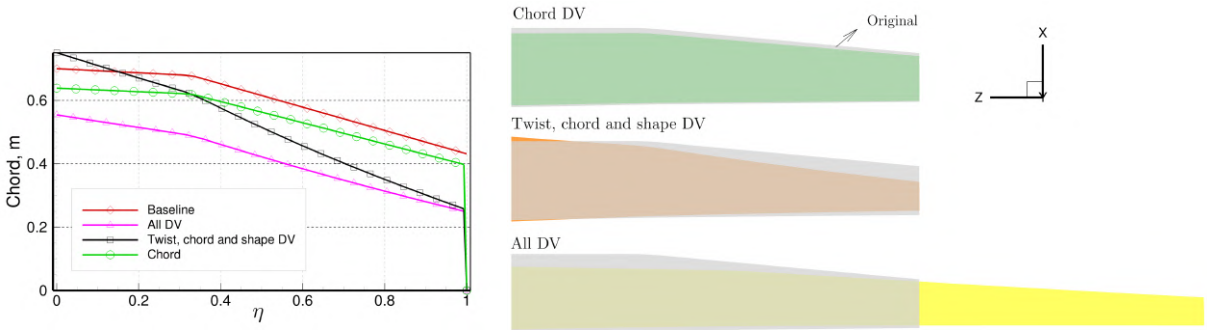

(a) Chord distribution for all optimization cases. (b) Overlap of baseline and optimal wing to compere the chord distribution.

Figure 5.25: Effect of chord distribution for each optimization case.

The elastic wing twist generally follows a consistent path, as shown in Figure 5.26a, where the twist

decreases along the span.

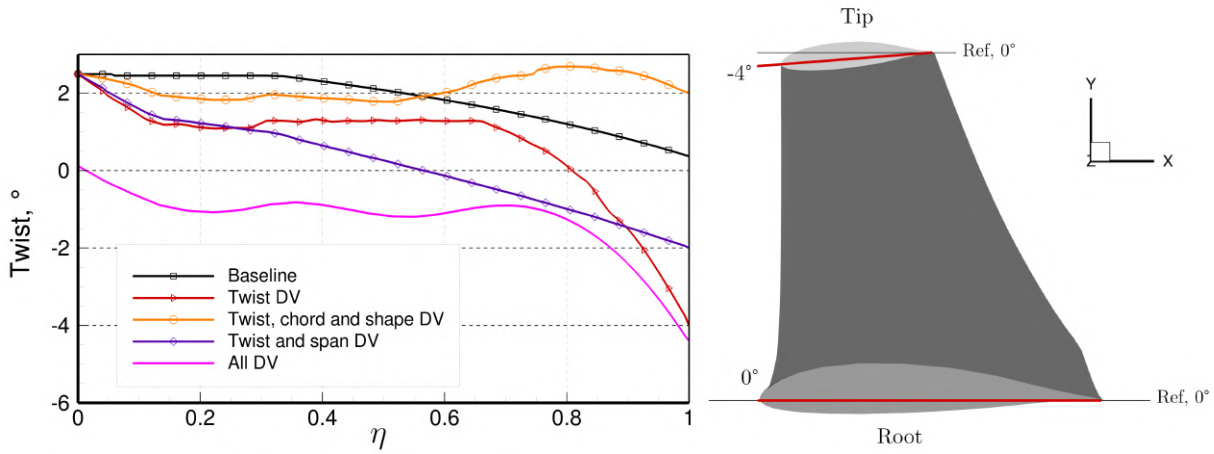

(a) Twist distribution for all optimization cases.

(b) Root and tip twist for the all DVs case.

Figure 5.26: Effect of twist in aerostructural optimization.

This twist behavior is beneficial for both aerodynamic and structural performance by being another tool to shift lift toward the root of the wing. As seen in the case of chord optimization, the goal is to reduce lift at the tip and increase it near the root, which improves both aerodynamic efficiency as the baseline solution in the section closer to the tip is placed above the elliptical optimal and structural load distribution. The twist reduction observed along the span supports this objective, especially near the tip, where the twist decreases more sharply. When span is included as a design variable, the effect becomes more pronounced. A larger span increases the wing area, which requires a lower overall lift per section and lower angle of attack to keep the aircraft in trim, as seen at Table 5.5, where is observed for the twist and span DVs case an reduction of angle of attack to zero. Since the root twist is fixed (saving the optimization from double control at the root), the reduction in effective angle of attack occurs mostly along the span, especially beyond the 70% mark, further concentrating lift near the root. This is also structurally advantageous as helps to prevent the aeroelastic divergence effect.This large increase in span i possibly being exacerbated by the lack of winglet to control induced drag.

In cruise conditions, a maximum tip twist of about -4° was observed for both twist optimization alone and for all design variables. In the case of twist optimization, that was the only way of reaching the aerostructural objectives leading to the minimum observed. When span was optimized, the increased span allowed for greater deflection during maneuvers, which further emphasized the need to shift lift toward the root. Moreover, the applied washout, besides its advantages in drag reduction, is also a desirable safety feature to ensure that the root section stalls before the outer section, were control surfaces are located, avoiding the loss of aileron authority. Figure 5.26b shows the wing shape in the all DVs case, from the perspective of looking in from the tip to the root in the span direction, where the mention negative twist around the tip and very close to zero at the root can be seen.

The twist, shape and chord optimization case presents an outlier case, as shown in Figure 5.30, where the wing undergoes significant deflection, possibly unrealistic. The chord distribution the most root heavy which helps redistribute lift inboard and makes the usage of twist unnecessary to achieve the

desire aerostructural response.

It is important to mention that despite the large negative twist angles, the angle of attack in general increased (Table 5.5). Indeed, specially when locking to the all DVs case,it represents not only a very negative twist distribution, but also the highest angle of attack, shifting the effective angle of attack closer to the remaining cases. The general increase in angle of attack balances some of the lift degradation behavior observed by the optimizer attempting to achieve the best aerostrctural solution.

The effect of the airfoil shape design variable can be seen in Figure 5.27, where the aerostructural optimization highlights the trade-off between reducing airfoil thickness for aerodynamic benefits and increasing it for structural reasons.

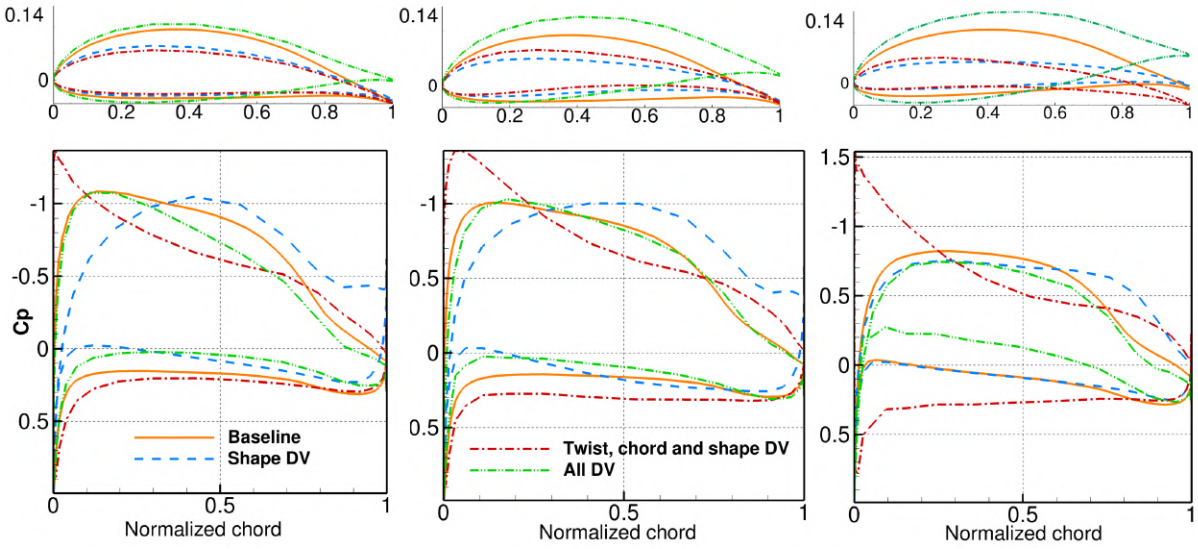

Figure 5.27: Airfoil shape and coefficient of pressure distribution at 10%, 50% and 90% of the span in each optimization case.

The optimizer, in general, favored reducing the original thickness as much as possible, while still ensuring the structure could handle the loads. This thinning resulted in a higher suction peak at the front of the airfoil, which is generally undesirable, especially near the wingtip and control surfaces. Such thin airfoils tend to stall quickly with little warning, as the transition from the linear part of the lift curve (C_L vs α) to stall is very abrupt.

In the shape DV case, thinner airfoil shape resulted in reduced drag due to less frontal area, and lower lift requirements due to a decrease in overall mass. This reduction in lift and drag came from making the profile thinner and symmetric, shifted the center of pressure backward, as seen in the C_P distribution. As expected, the thickness reduces with wing span, starting at the root with a 32% reduction and achieving a 50% reduction at the tip.

The twist and effective angle of attack variations in other cases also affected the C_P distribution. The previously discussed reduction in lift near the tip, achieved by applying negative twist, can be clearly seen in the C_P distribution graph, with a smaller area near the tip due to this effect, specially seen in the all DVs case, where the thickness and general distribution is the same as the baseline case, but with a negative twist.

In the combined twist, chord, and shape optimization case, the optimizer achieved maximum thinning of the airfoil (46% reduction at the tip, 14% mid-span, and 37% near the root). This configuration provided the best overall performance in terms of range when the span DV was not active. However, as mentioned earlier, this case exhibited unrealistic structural behavior, with excessive wing deflection, indicating the wing became too flexible to handle the loads effectively. Nevertheless, the sharp C_P increase in relation to the remaining cases are explained by the thin airfoil at an higher effective angle of attack from the continuum positive twist distribution around the 2° (Fig. 5.26a) align with the similar wing angle of attack to the remaining cases (Tab. 5.5).

When all DVs are active, the airfoil shape and pressure distribution, showed a very small thickness reduction, so that sufficient bending stiffness is still obtained. Furthermore, the overall shape was maintained, with the only difference in the C_P graphs coming from the different effective angle of attack.

In all cases without the span DV, there was a significant thinning of the wing panels, particularly at the front spar and lower skin, as shown in Figure 5.28. Interestingly, the thickness of the upper skin section near the root generally increased, indicating that the optimizer not only reduces thickness where possible but also reinforces critical areas in response to significant changes in aerodynamic load. This differs from the results seen in structural optimization alone, as discussed in Section 4.6.2. This effect on the upper panel, likely arises from the primary loading on that panel being compressive, combined with the material's lower strength in compression compared to tension (as seen in the lower skin panel). As a consequence, a 63.6% wing weight reduction was achieved for the chord case, 50.6% in the twist case and 47% in the twist, chord and shape case. All cases, at the tip region, went to the minimum thickness allowed, as the main structural loading occurs at the wing root.

On the other hand, an increase in weight were observed when the span was able to change. A significant thickening of panels was observed (see Figure 5.26a), particularly at the rear spar and lower skin panels near the root that, combined with the increase in length, led to 130% and 114% wing weight increase for the span and all DVs case respectively. Moreover, from a lack of buckling constraints, the rib thickness was almost always reduced to the minimum allowed, 1mm. It is also important to mention that the monotonic thickness decreasing constraint is active allowing for eliminating discontinuities that could harm the manufacturing process of the wing and even impose week point when they were established.

The drastic improvement of the structural efficiency is attested by the KS index failure increase shown in Figure 5.29, where the optimized wing box exhibits more regions with a higher failure index, meaning it works closer to failure due to the overall thickness decrease. It is observed than the structure still behaves with a very large safety factor, with the limiting factor being the efficient aerodynamic response, and not the failure constraints. The most requested case was the twist, chord and shape case with higher failure index and a more loaded structure. The regions of high failure index, presented a lot of deflection that may be problematic. In general, the cases with the span DV presented a similar structural result as the remaining, despite the higher bending moments, due to the generally higher panel thickness even higher than the baseline solution.

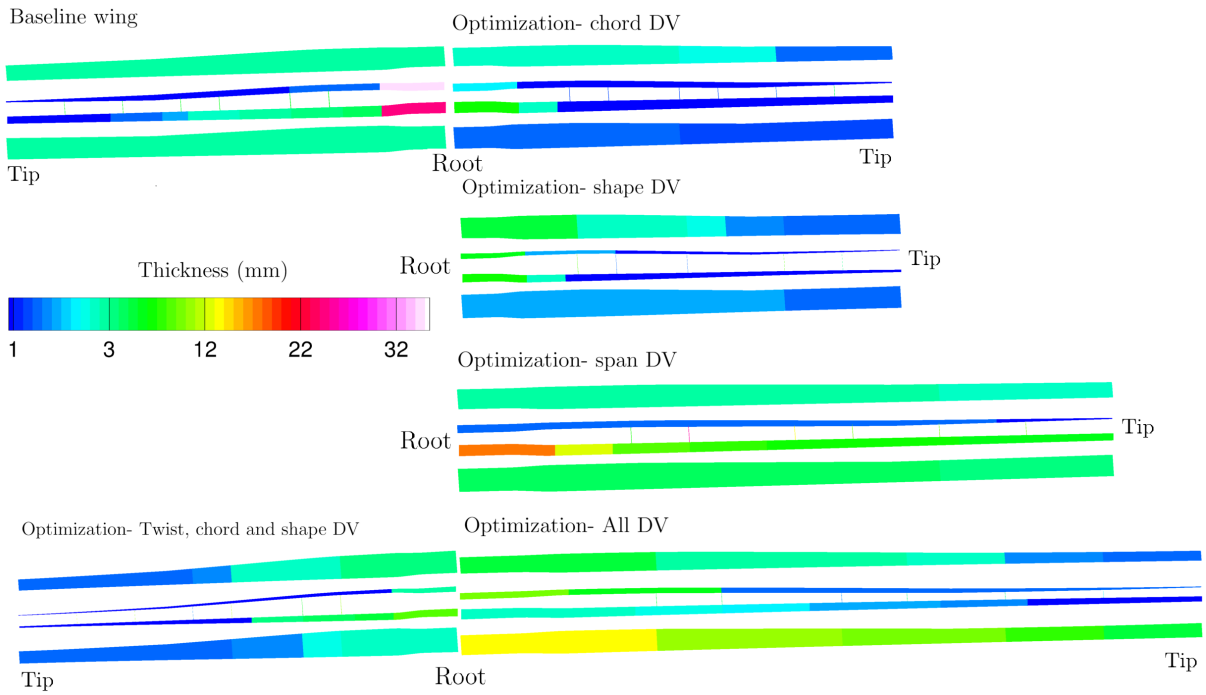

Figure 5.28: Thickness distribution in each optimization case.

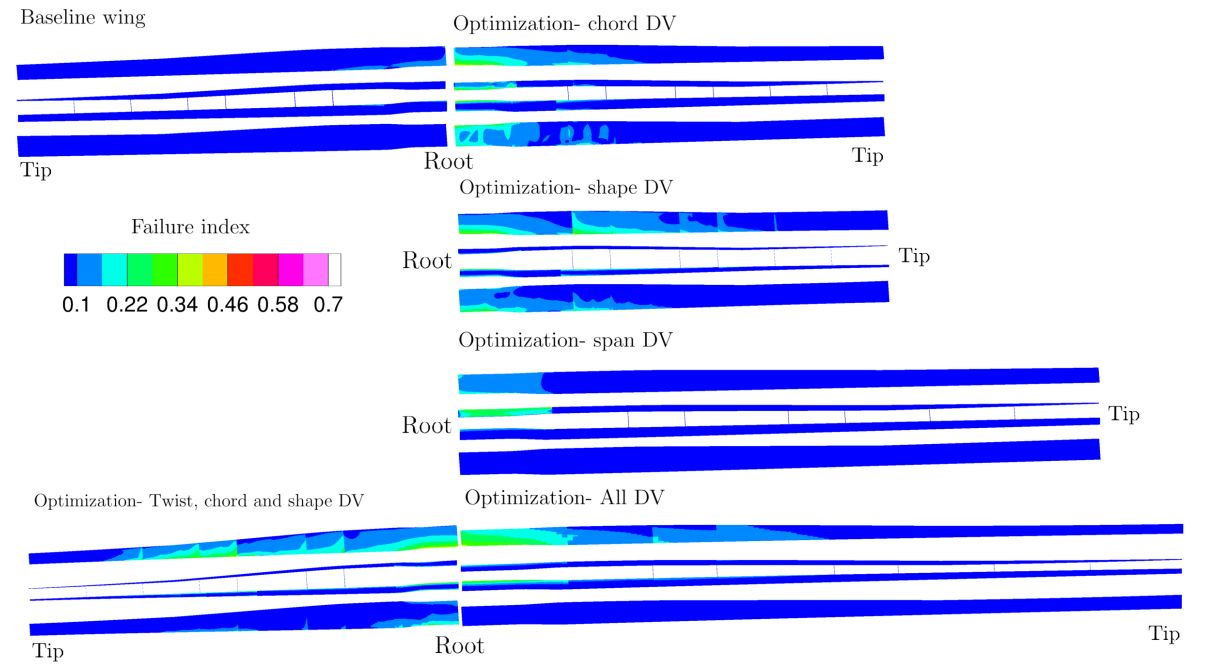

Figure 5.29: KS failure index in each optimization case.

The normalized deflection achieved was not always the same, as seen in Figure 5.30 which does not rely allow for a direct comparison for the reason that led to the weight reduction, leaving the doubt of optimizer having achieved an local minimum that allow for different wing normalized deflection scenarios. Nevertheless, the results are consistent with failure index, indeed, the maximum normalized deflection happened for the cases off thinner airfoils and maximum values of failure, in shape and twist, chord and shape DVs with 0.28 and 0.27 tip normalized deflection, then for the all DVs (0.17), chord DV (0.15),

twist DV (0.11) and finally, twist and span DVs with a 0.095 deflection, all in relation to the baseline 0.08 normalized deflection. Therefore, a maximum tip displacement constraint will be employed. That constraint was tested for the simplified wing for one of the most critical cases, the twist, chord and shape DV optimization with the results being presented in Section 5.5.1.

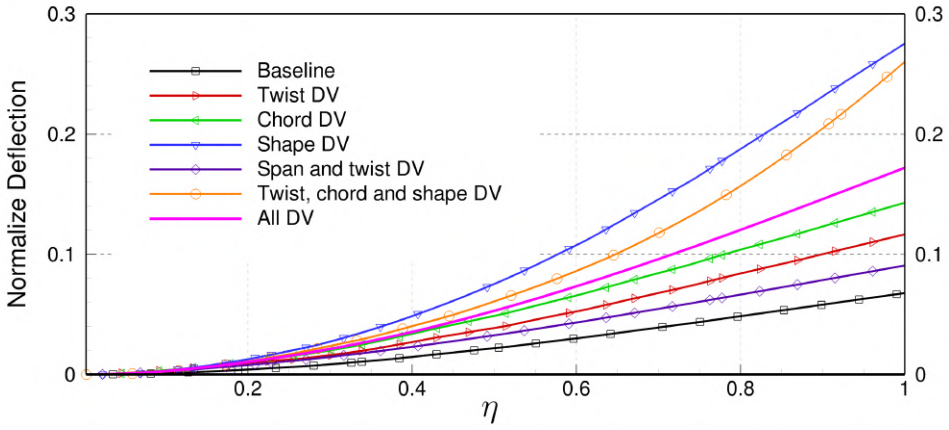

Figure 5.30: Normalized deflection in each optimization case.

The ply angle distribution is shown in Figure 5.31, which demonstrates that the optimal solution is feasible in terms of manufacturing.

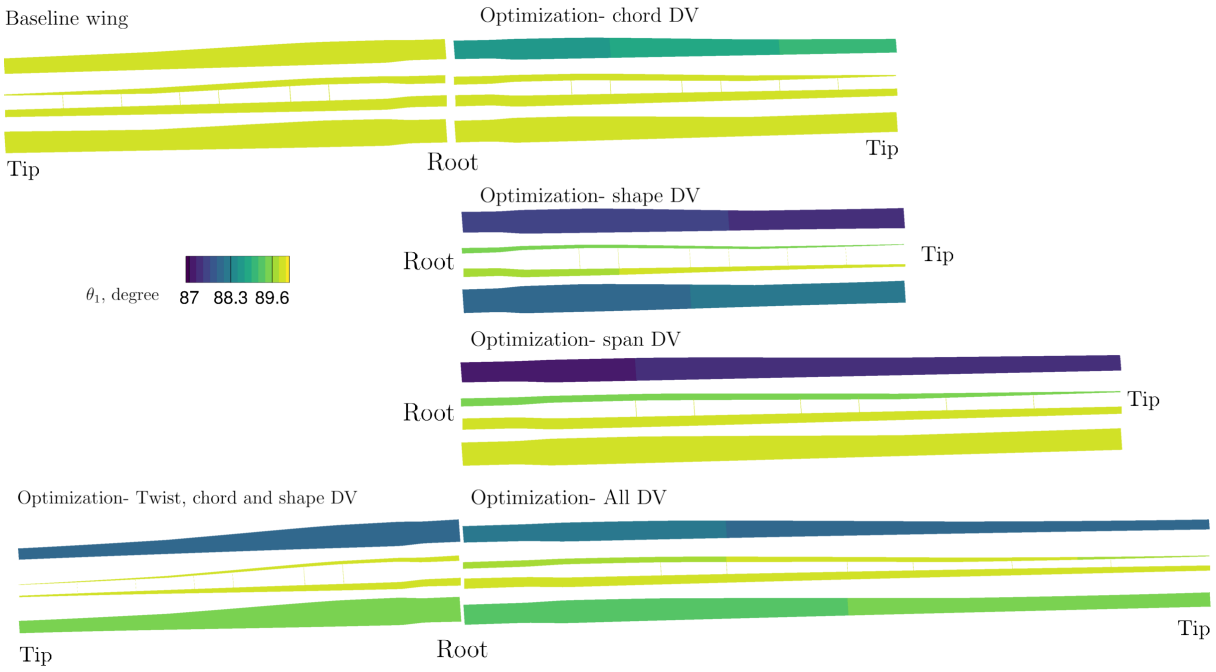

(a) Angle θ_1

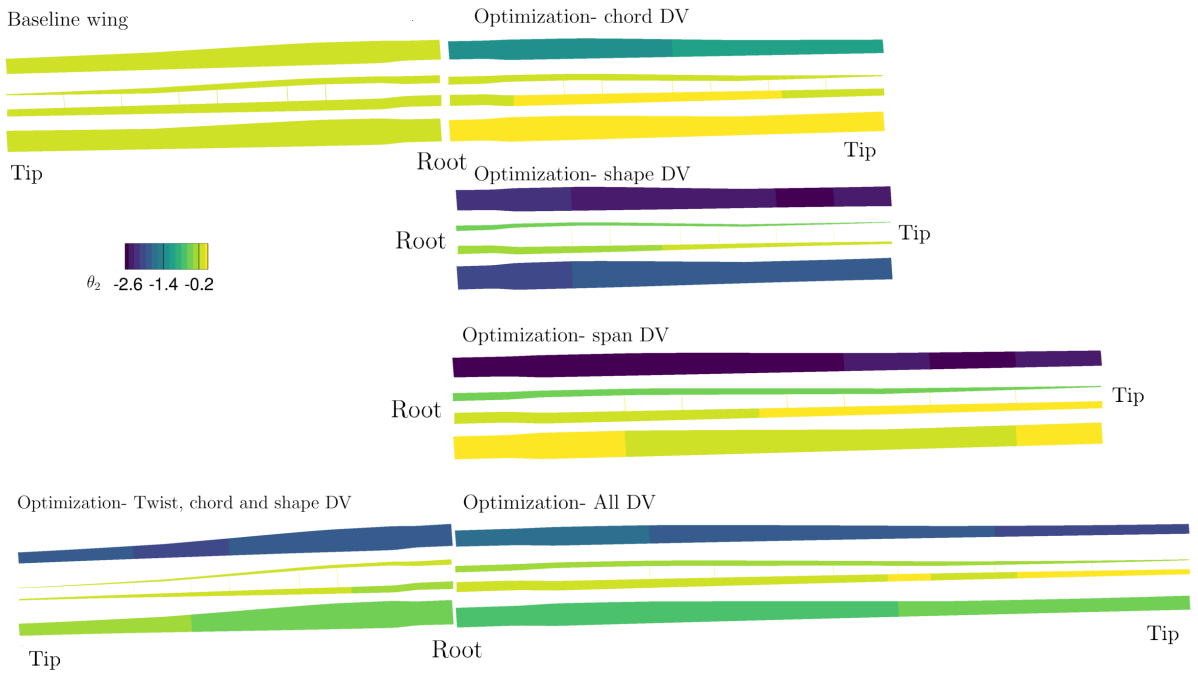

(b) Angle θ_2

Figure 5.31: Optimal distribution of ply angles in each optimization case.

The continuity of the fiber is verified, as well as the orthogonality, which benefits the design process. Furthermore, it can be observed that the biggest shifts in ply angles always occur in sections where the safety factor is smaller, indicating the need for general improvements. For example, in the shape DV case, where we see high failure indices in the upper and lower panels, the ply angles also affect both parts. During flight, the two significant efforts are around bending the wing in the direction of increasing the tip height and twisting the airfoil. Therefore, the fibers should be aligned to resist these efforts, since we have an orthotropic material, which is particularly strong in the fiber direction. It is expected that the fibers be mostly aligned with the span direction to resist the bending effort, but also slightly tilted to handle the shear force from the twisting of the wing. The ribs maintained the initial ply angles for all cases. It is important to mention that the ply angle is highly constrained, which almost always leads to achieving a uniform angle throughout the wing part, with very few changes along the span.

5.5.4 Effect of the Aerostructural Analysis

The aerostructural analysis and optimization of a wing is a highly computationally intensive task, often resulting in process times that exceed those of isolated disciplines by more than an order of magnitude. While there are techniques to mitigate this effect, such as implementing partial convergence during the initial iterations of the aerostructural analysis of aerodynamic and structural components [38], the task remains challenging. Each aerodynamic and structural analysis requires a single convergence of the governing equations for its respective discipline, whereas aerostructural analysis necessitates multiple partial convergences and at least one full convergence, along with additional time for load and displacement transfers. Moreover, the design space is much larger and unforeseeable interaction

between the DV became a problem. There is an important limitation in the mesh deformation technique being employed, large ones will lead to negative volumes in the mesh which will break the MDA, Therefor, artificial tight bounds need to be defined and even then, it may be difficult to obtain an optimal solution in a vast of design space. As such, there is the need to understand if this has a significant impact in the final solution in terms of accuracy and optimization gains. Finally, a complex couple adjoint system of equation must be solved, with a vast number of constraints from both cases, that is once again computationally complex, as the adjoint method of computing derivatives, do no scale well with the number of constraints.

However, there is also a large penalty when considering isolated optimization, especially in the sense of accuracy and potential optimization. In fact, the deflection of the wing affects the shape and lifting surface and, naturally, the optimal shape in flight, due to a structural response. In the same way, structural response design is limited to that initial situation, and not the optimal during flight, becoming also hard to foresee the aerostructural response will lead to divergence or control reversal. In this work no attention will be payed to the latter one. Therefore, it is interesting to compare the analysis solution obtained of the coupled and uncoupled situation for the same meshes and initial conditions and their computational effort.

There is not any significant difference for the angles of attack analyzed in the macro proprieties, just a slight increase in angle of attack to obtain the same lift, that leads to a small change in drag between the jig and elastic analysis as seen in Figure 5.6 and Table 5.6. Nevertheless, that impact is very small as the forces are not very high to deform the structure with, a maximum deflection in the wing tip around 4% (Figure 5.11) which manifests as identical lift and pressure distribution (Figures 5.34a and 5.35). However, there is a great difference when considering the computational resources. From Table 5.6, it is possible to see the impact of all analysis considering a Central Processing Unit (CPU) with 12 threads and clock speed of 4.5GHz. The structural analysis has a very low cost in the overall process, being concluded in just seconds, while there is a large cost for performing aerodynamic and aerostructural analysis, as multiples iteration between this two disciplines are needed. It is also important to observe that at Table 5.6 is present a best case scenario as it presents the values for the trimmed aircraft (low angle of attack), run time drastically increases with the angle off attack when the aerostructural interaction is more appreciated, and the flow solver has to resolve a a more complex flow.

Table 5.6: Summary of results for the type of analysis.

Analysis mode	Angle of attack	Drag, N	CPU time	RAM usage
Aerodynamic	-9%	+0.1%	-66%	-20%
Structural	-	-	-99.95%	-60%
Aerostructural	ref	ref	ref	ref

Moreover, it is also important to characterize the structural, aerodynamic and aerostructural optimizations in terms of computational effort and general performance improvement. It is important to select the DVs used in each optimization: to compare the structural part of the problem, a structural optimization is consider, and a twist DV aerostructural one both with panel thickness and ply angles. To interpret the

aerodynamic part of the problem, the twist, chord and shape DVs are consider in the aerodynamic and aerostructural optimizations.

The overall cost differs significantly across the analyses. The structural optimization converged in just 1.2 hours, while the aerodynamic optimization took nearly 26 hours. Finally, the aerostructural optimization considering twist, chord and shape stalled after approximately 140 hours. This outcome is expected because, in aerostructural analysis, everything requires more time: multiple aerodynamic and structural analyses had to converge at each Gauss-Seidel iteration for the two conditions being analyzed (cruise and maneuver); Additionally, there was a significant increase in the number of constraints being evaluated, such as lift and drag during cruise, and the failure indices of the upper and lower skins, front and rear spars, and ribs, all of which had to be evaluated considering both disciplines. This created complex adjoint situations that required many iterations to converge, leading to an exponential increase in time for the aerostructural case. Furthermore, memory usage also doubled compared to the previous analyses, due to the simultaneous evaluation of the two conditions. The summary of results are presented in Table 5.7.

Table 5.7: Summary of results for the type of optimization.

Optimization mode	mass	L/D	Run time	RAM usage, GB
Aerodynamic	-	+3.1%	26h	16
Structural	-70%	-	1.2h	8
Aerostructural	-44%	+14%	140h	40

Additionally, the accuracy of the prediction and the capturing of the aerostructural trade-offs is very visible in the optimal solution, which leads to drastically different approaches from the optimizer. Indeed, the structural optimization without a deflection constraint will achieve a much more efficient structure, as seen in the comparison between the failure index and the thickness distribution present in Figures 5.32 and 5.33, having a much further reduction in mass of 70%, 20% more than in the twist DV aerostructural one, with almost all the panels going to the minimal thickness allowed. As the general load distribution is similar, the general thickness distribution is maintained in both situations, with the thicker part being the spars, followed by the upper skin as indicated by the failure index distribution as the most requested structural components (Fig. 5.33).

Moreover, Figure 5.33 also presents the effect of using the manufacturing constraints for booth fidelity optimizations, indeed, the effect is very similar in this regard.

Even thou the maximum failure index is never surpassed during the maneuver, in the structural optimization never surpassing 0.55 while in the aerostructural capped at a lower value, as a thinner, and more prone to fail structure, will have a lot of deflection (0.19 normalized deflection) with double of aerostructural case (0.11 normalized deflection), that would negativity impact the aerodynamic solution. Therefore, the structural solution itself, besides being too optimistic considering the high deflection, is not relay feasible since the wing could not produced the lift being required, highlighting one of the main advantage of the aerostructural optimization with the automatic trade-off between the deflection and structural efficiency until a certain point and its consideration of the aerodynamic optimal in the overall

solution. This advantage, needs to be taken with some care and it will be discussed next.

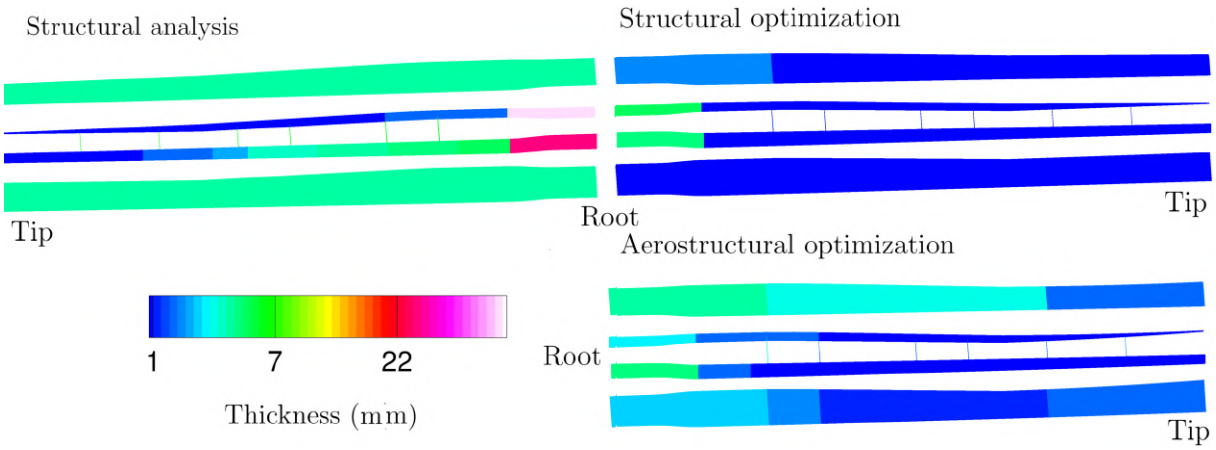

Figure 5.32: Thickness of structural material for aerodynamic/aerostructural analysis and optimization.

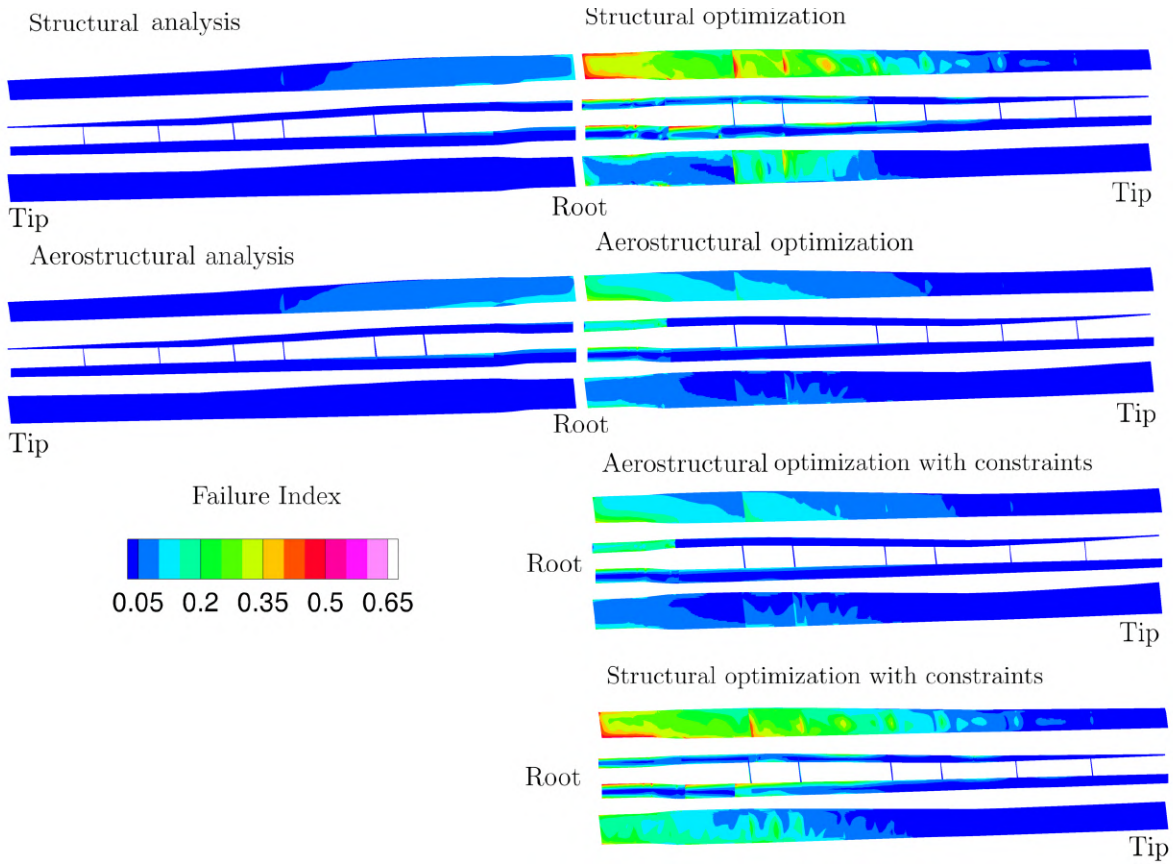

Figure 5.33: Failure index of the wing for aerodynamic/aerostructural analysis and optimization.

This consideration of the aerodynamic aspect of the solution is also evident. From Figure 5.34b, it is clear that there is a drastic difference in lift distribution between the aerostructural and aerodynamic optima. Indeed, the ideal elliptical distribution is almost achieved during the aerodynamic optimization, but no longer holds as priority, shifting toward a more structurally optimal configuration to further reduce weight (Figure5.34b), resulting in a more efficient structural response by reducing the bending moments caused by larger moment arms. This scenario highlights another key advantage of using coupled anal-

ysis for optimization.

In contrast, the lift distributions between the aerodynamic and aerostructural analyses are very similar, almost indistinguishable, when considering cruise flight. This is because, at that load level, the structure is stiff enough to deform very little, with deflections normalized under 4% (Figure 5.34a). Thus, it is reasonable to assume the aerodynamic solution remains valid, with minimal structural deformation.

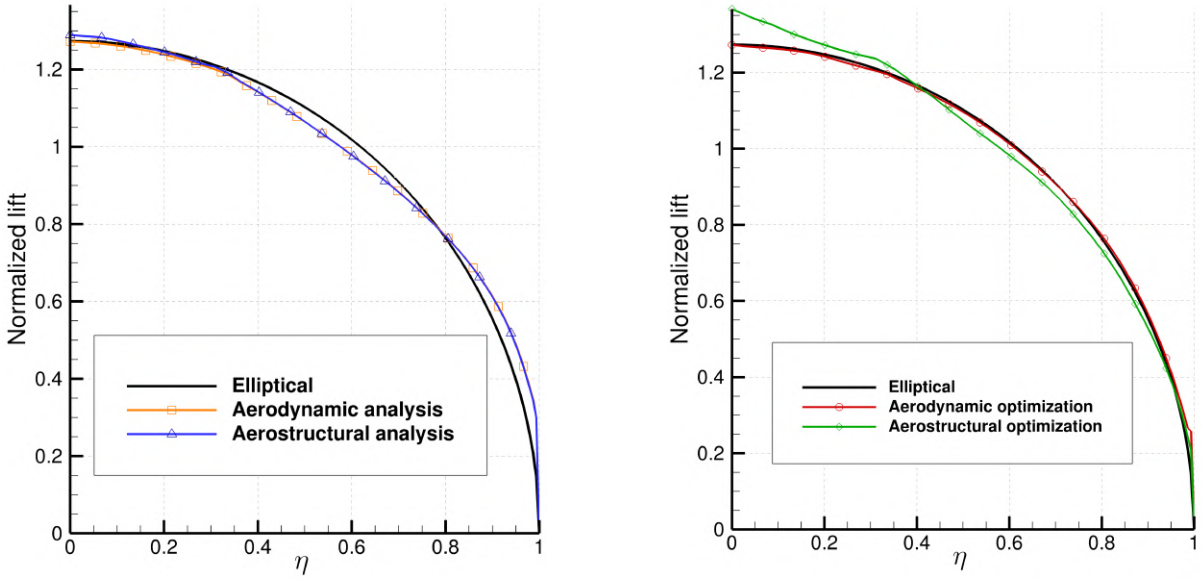

(a) Analysis.

(b) Optimization.

Figure 5.34: Lift distribution of the wing for aerodynamic/aerostructural analysis and optimization.

It is also interesting to observe that there is a clear tendency for the airfoil to always thin under optimization needing to be constrained during the aerodynamic optimization, by an arbitrary thickness condition to prevent critical structural components from becoming too thin. This limitation is difficult to predict during the isolated optimization, where the threshold is not readily apparent, demonstrating the significant impact of including the structural weight in the objective function.

As shown in Figure 5.35, when the airfoil is allowed to thin, provides advantages such as reduced pressure drag and mass at the expense of structural bending stiffness. This results in an increase in deflection, reaching concerning values (around 0.28 normalized deflection) in contrast to the remaining cases (Figure 5.30). At this level of wing flexibility, aeroelastic phenomena may become hazardous, as evidenced by the upward wing twist seen in this optimization case in Figure 5.36, which contrasts with the other cases where shape is not allowed to change. Consequently, a deflection constraint was introduced, as discussed in Section 5.5.1, to improve structural stiffness. However, the thickness was still not directly limited, leaving it to the optimization process to find a feasible solution under the new constraints. Moreover, in Section 5.5.1, it was observed that even with the deflection constraint, there was a maximum thickness reduction of 14%, which was 4% greater than the 10% constraint established in the aerodynamic optimization. On the other hand, at the root, the aerostructural optimizer was only able to reduce the thickness by 8%, exceeding the constraint by 2%. Furthermore, it is important to note that during aerodynamic optimization, the airfoil's thickness was reduced to the minimum allowed,

confirming the aerodynamic advantage of a much thinner solution when structural constraints are less stringent.

Finally, it is also noteworthy that the same behavior observed in the overall characteristics of the aerodynamic versus aerostructural analyses (with similar lift and drag during cruise) is reflected in the C_P distribution, which shows no significant differences between the two while in the optimization, the effect of the thinner airfoils is present.

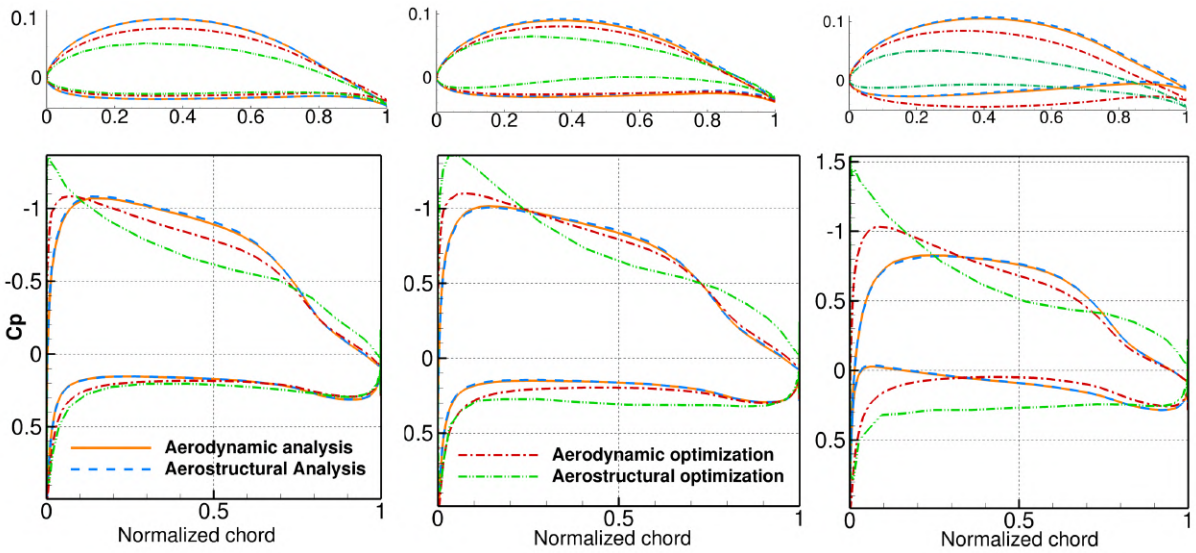

Figure 5.35: Coefficient of pressure and correspondent airfoil shape at 10%, 50% and 90% of the wing for aerodynamic and aerostructural analysis and optimization.

When comparing the twist distribution between the two fidelity cases presented in Figure5.36, one can appreciate the final advantage of aerostructural analysis: the ability to optimize the actual wing twist after accounting for the deformation caused by the moments generated by the airfoil, which induce wing twisting. By examining the twist distributions from both the aerodynamic and aerostructural analyses, a tendency towards negative wing twist is observed. This explains the increase in the angle of attack, as seen in Table 5.2. The difference in angle of attack (0.2°) combined with the effective twist distribution of the elastic wing achieves the same effective angle of attack as the jig aerodynamic analysis, resulting in the same amount of lift required at trim. For this angle of attack and load factor, the wing undergoes noticeable structural deformation. Focusing now on the optimization results, the influence of the structure on twist becomes even clearer. The substantial difference between the design geometry's twist and the effective twist experienced by the wing in flight highlights this. This is especially evident in cases where the structure exhibits unusual behavior, showing that it struggles to resist the twisting moment to the desired extent. As a result, the outer section of the wing experiences positive twist, leading to an even worse behavior during maneuvering passing from the the tip twist of 2° during cruise to 9° at maneuver.

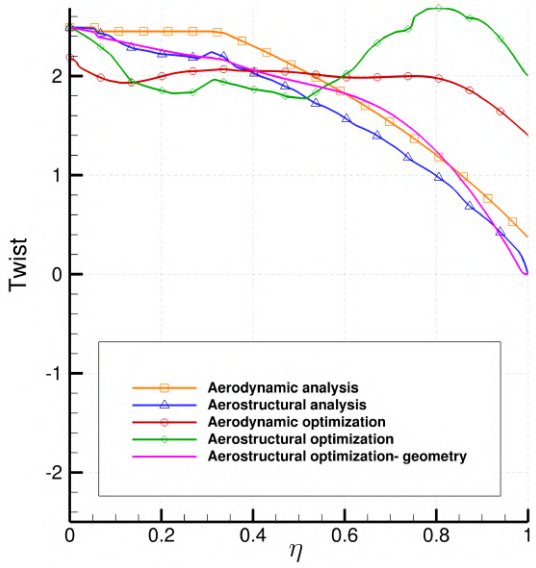

Figure 5.36: Twist distribution of the wing for aerodynamic/aerostructural analysis and optimization.

From these comparisons, an additional conclusion can be drawn: the aerodynamic and structural optima differ significantly from the aerostructural optimum. While conducting aerostructural optimizations is resource-intensive, the resulting improvements are substantial enough to demonstrate that such optimizations are necessary for achieving better overall performance compared to optimizing each discipline separately.

Moreover, due to these significant differences, starting from the aerodynamic and structural optima does not lead to better results. In fact, when this approach was tested, it caused issues during the multidisciplinary analysis (MDA) convergence, as the structure experienced excessive deformation, which led to mesh failure during the aerodynamic analysis. Typically, the conventional approach begins with the individual discipline optimum, and while this might be effective for simpler geometries such as a rectangular wing, it was not suitable for the initial TEKEVER AR5 wing. The TEKEVER AR5 wing already represents a solid starting point, so this method proved less beneficial.

Additionally, an optimization using the original structure and the optimized aerodynamic mesh was tested, but it did not result in any improvements in terms of the final solution time. Therefore, this approach was ultimately not considered in the final solution.

5.5.5 Final Remarks

To conclude the main findings from the analysis presented in the previous subsections, it's important to highlight the key insights before proceeding to the next step. Table 5.8 summarizes the most critical performance parameters for all solutions, providing a clear overview of the results.

Table 5.8: Optimization results for the simplified TEKEVER AR5 wing as starting geometry.

Case	Mass	Lift	Drag	L/D	UAV Range
Twist with manufacture constraint	-50.6%	-2.1%	-2.6%	+0.6%	+0.8%
Chord	-56.6%	-2.3%	-3.1%	+0.9%	+1.0%
Twist and span	+131.7%	+5.3%	-13.0%	+20.9%	+6.3%
Airfoil shape	-42.3%	-1.6%	-11.0%	+10.6%	+4.5%
Twist, chord, airfoil shape	-47.0%	-1.9%	-14.3%	+14.4%	+5.8%
Twist, chord, airfoil shape with disp constraint	-43.9%	-1.8%	-11.0%	+10.4%	+4.2%
All design variables	+114.0 %	+4.5%	-20.9%	+32.2%	+9.9%

From all cases performed, the optimizations led to a large decrease in mass, from 42% to 56%, while also allowed for an improvement in aerodynamic efficiency, from 0.8% to 32.2%. A natural tendency emerged from the discipline interaction that resulted in an aerostrcutural optimal lift and thickness distribution. As expected progressively better results were shown with the inclusion of additional design variables resulting in an overall 9.9% increase in range. The more constrained cases achieved allways poorer results. Those constraints mainly served practical purposes, such as ease of manufacturing and aircraft trimming. An exception appeared in the airfoil thickness that revealed to play a crucial role in bending stiffness, which required adding a displacement constraint to control it.

Moreover, the solution was less limited by failure constraints than initially expected. In all cases, the maximum value of 0.67 (from the 1.5 safety factor) was not reached, with the highest value achieved being around 0.45 in the cases involving twist, shape and chord design variables.

Several key insights also arose from the aerostructural analysis. The wing showed a tendency to negatively twist at low angles of attack, reducing lift, while exhibiting the opposite behavior at high angles of attack, which could lead to potential issues.

Additionally, some considerations must be made regarding the two most promising solutions. Despite being thinner and more flexible, the optimized solution did not degrade in terms of aero-elastic phenomena, as evidenced by the analysis conducted at diving speed and maximum allowed loading factor, with the resulting wing tip twist summarized in Table 5.9.

Table 5.9: Wing tip torsion at cruise and dive speed.

Cases	Tip twist		
	1 g	2 g	Δ
Baseline	0.2	1.2	1
Twist, chord and shape DVs with disp constraint	-3.1	-2.8	0.3
All DVs	-4.1	-5.1	1

For the all DVs case, the observed reduction in wing tip twist during cruise results in favorable behavior under maximum velocity and maximum load conditions: the slight negative twist in the wing helps delay aeroelastic phenomena such as wing divergence. Furthermore, the general relationship between the center of pressure, elastic center, and torsional rigidity is preserved, as evidenced by the consistency in twist variation under identical loading conditions. For the case where the span is fixed, a very small difference is observed in tip torsion, despite the negative tendency for twist to increase with higher loads. However, this increase is much smaller than in the baseline case, suggesting that torsional rigidity is maintained or even improved. This indicates that the new design will not negatively impact the UAV's aeroelastic performance, especially within its flight envelope.

Noteworthy, the greatest improvements were achieved with the span as design variable. However, despite its clear benefits, this case presented a significant practical issue from the resulting 1.7 fold increase, as corroborated by the manufacturer that is also designing a new large span UAV. Such an increase would imply a complete redesign and re-certification of the UAV to a more strict regulamentation. Manufacturing a wing of such size would also require significantly more space, materials and labor, along with harder to produce molds and substantial logistical challenges in transportation inside the factory. Additionally, the larger span also complicates transportation and could deter potential buyers, as it affects runway requirements for takeoff and landing. This leads to the conclusion that while the span increase offers substantial performance gains, it may only be practical for the design of a completely new product, as the associated costs for modifying an existing UAV would be prohibitive.

Given these constraints, the focus naturally shifts to designs that exclude span as a design variable. This alternative was also explored and showed promising results, achieving a 4.2% increase in range, the highest possible without modifying the span, while maintaining good structural integrity. This result is notable because, when the same optimization was performed within individual disciplines, none achieved similar success. The aerodynamic optimization, for instance, was unable to improve the lift-to-drag ratio due to higher lift requirements. On the other hand, the structural optimization, when unrestricted, led to a further mass reduction, considering mass alone only yielded a 3.36% increase in range. Finally, the solution which excludes span as a DV offers a balanced and feasible approach, making it a strong candidate for guiding the next version of the TEKEVER AR5.

Chapter 6

Conclusions and Future Work

6.1 Achievements

This thesis focused on the aerostructural optimization of the TEKEVER AR5 UAV wing, aiming to improve performance by coupling aerodynamic and structural disciplines. The study used the MACH-Aero framework from the University of Michigan's MDO Lab, confirming that it is well-suited for this UAV's characteristics. Key optimization methods included the gradient-based SLSQP optimizer and the adjoint method for gradient calculations, with the MDF framework and Gauss-Seidel algorithm ensuring effective multidisciplinary design and analysis, respectively.

Initial aerodynamic optimization, using the ADFlow solver, led to a 4.76% reduction in drag, primarily due to airfoil thinning, which was constrained by structural concerns and an winglet wight increase. A specific winglet optimization further reduced drag by 2.5%, achieved through small adjustments in twist, chord, and large increase in winglet dihedral values. This demonstrated the significant impact of winglet design on overall aerodynamic efficiency.

The structural optimization, performed with TACS, achieved a 43.6% reduction in wing mass, but at the cost of a 1.75 fold in wing deflection. This result highlighted the need for additional constraints, particularly to limit displacement and control wing torsion. Furthermore, aeroelastic concerns arose, particularly regarding wing twist and the behavior of a more flexible wing under aerodynamic loads.

In the aerostructural optimization, coupling aerodynamic and structural factors led to significant improvements in both mass reduction and aerodynamic efficiency. The most promising scenarios achieved UAV range increase from 4.2% (twist, shape, and chord DV with displacement constraints) to 9.9% (all design variables including span). These improvements resulted from a 43.9% reduction in mass and an increase in span, which also led to a 114% increase in deflection. The optimization revealed an optimal lift distribution, with negative aeroelastic twist helping to delay divergence and improve stall behavior.

Adjustments to the airfoil shape contributed up to a 4.5% increase in lift, but also required deflection constraints to prevent excessive wing flexibility. Thickness and ply angle variables were adapted to improve structural performance, with more significant thickness reductions near the wingtip and increases near the root. These adjustments balanced aerodynamic gains with structural integrity, showcasing the

effectiveness of the aerostructural approach.

The study concluded that manufacturing constraints had a minimal effect on the final solution, reducing range by only 0.1%, while the deflection constraint was more impactful, reducing range gains by 1.6% but ensuring structural integrity. When comparing aerodynamic, structural, and aerostructural optimizations, the aerostructural approach proved superior, despite taking 4.1 times longer. The final solution differed substantially from individual discipline optimizations, offering a more balanced design that improved range, reduced mass, and enhanced aerodynamic efficiency.

In summary, the aerostructural optimization of the TEKEVER AR5 UAV wing resulted in a significantly lighter, more efficient design, achieving notable range increases while maintaining structural integrity. The process demonstrated the value of coupling aerodynamic and structural disciplines, leading to an optimal design that relaxed traditional constraints and provided substantial performance gains.

6.2 Future Work

To enhance the findings of this thesis on the TEKEVER AR5 UAV, several avenues for future work are recommended.

First, addressing the limitations of the current mesh deformation algorithm is crucial. Implementing more advanced deformation techniques would help produce usable volume grids under large deformations, thus expanding the optimization space and improving convergence during multidisciplinary analysis and larger shape deformations.

Incorporating a transition model that accurately captures the laminar-to-turbulent flow dynamics would provide more precise aerodynamic results, facilitating better optimization outcomes specially when considering the winglet. Furthermore, future analyses should include the complete UAV geometry, accounting for the fuselage and tail to better understand the interactions between these components and achieve a comprehensive aerostructural optimum.

Structural considerations should also be expanded. Adding buckling constraints to the ribs would enhance overall design reliability. Detailed structural analyses that factor in the UAV's propulsion system are essential, as the propellers impacts the optimal wing shape and its structural behavior. Improving material characterization through experimental testing would refine the material properties used in simulations, leading to more accurate predictions of performance. Additionally, incorporating aeroelastic constraints would help prevent potential divergence and flutter, rather than merely verifying their tendency.

Finally, to overcome the limitations imposed by computational power, increasing access to more robust computing resources is essential. This would allow for a thorough multipoint analysis of critical flight conditions, enabling the optimization process to fully account the complete flight envelope and ultimately yielding a more refined UAV design.

Bibliography

[1] P. Höhrová, J. Soviar, and W. Sroka. Market Analysis of Drones for Civil Use. *LOGI – Scientific Journal on Transport and Logistics*, 14(1):55–65, 2023. doi: 10.2478/logi-2023-0006.

[2] L. Parada. Conceptual and Preliminary Design of a Long Endurance Electric UAV. Master's thesis, Instituto Superior Técnico, Portugal, 2016.

[3] A. Kalashnikova. Business Potential Analysis of UAV Applications. Master's thesis, Lappeenranta University Of Technology, Finland, 2018.

[4] M. G. Levy. Drones Have Transformed Blood Delivery in Rwanda, 2022. URL `https://www.mdpi.com/2073-4395/9/6/308`. Accessed on 10-09-2023.

[5] A. Hanif, X. Han, and S.-H. Yu. Independent control spraying system for UAV-based precise variable sprayer: A review. *Drones*, 6(12):383, 2022. doi: 10.3390/drones6120383.

[6] S. A. H. Mohsan, N. Q. H. Othman, Y. Li, M. H. Alsharif, and M. A. Khan. Unmanned aerial vehicles (UAVs): Practical aspects, applications, open challenges, security issues, and future trends. *Intelligent Service Robotics*, 16(1):109–137, 2023.

[7] Fact.MR. Fixed Wing Drone Market, 2022. URL `https://www.factmr.com/report/fixed-wing-drone-market`. Accessed on 10-09-2023.

[8] Grand View Research. Commercial drone market size, share and trends analysis report by product, by application, by end-use, by propulsion type, by range, by operating mode, by endurance, by region, and segment forecasts, 2023 - 2030, 2023. URL `https://www.grandviewresearch.com/industry-analysis/global-commercial-drones-market`. Accessed on 10-09-2023.

[9] J. Alvarado. Drone Market Report: Where the Drone Industry Will Grow the Fastest by 2030, 2022. URL `https://dronelife.com/2022/09/26/droneii-drone-market-report-where-the-drone-industry-will-grow-the-fastest-by-2030/`. Accessed on 10-09-2023.

[10] J. E. K. Hoogervorst. Wing Aerostructural Optimization Using The Individual Discipline Feasible Architecture. Master's thesis, Delft University of Technology, The Netherlans, 2015.

[11] Tekever. Tekever AR5, 2023. URL `https://www.tekever.com/models/ar5/`. Accessed on: 03-12-2023.

[12] R. Gameniro. Wing Aerodynamic Design for a MAME UAV using High-Fidelity Numerical Tools. Master's thesis, Instituto Superior Técnico, Oct Portugal, 2023.

[13] V. Silva. Wing Structure Design for a MAME UAV using High Fidelity Numerical Tools. MSc Thesis in Aerospace Engineering, Instituto Superior Técnico, Oct Portugal, 2023.

[14] MDO Lab of University of Michigan. Mach-Aero Documentation. `https://mdolab-mach-aero.readthedocs-hosted.com/en/latest/index.html`, 2024. Accessed: 8-02-2024.

[15] D. P. Raymer. *Aircraft Design: A Conceptual Approach*. America Institute of Aeronautics and Astronautics, 1989. ISBN 0-930403-51-7.

[16] J. Mariens. Wing Shape multidisciplinary design optimization. MSc Thesis in Aerospace Engineering, Delft University of Technology, Oct Netherlands, 2012.

[17] J. A. Martins, T. Brooks, J. Gray, P. He, J. Hwang, J. Jasa, G. Kenway, G. Kennedy, Z. Lyu, C. Mader, N. Secco, and A. Yildirim. Plenary presentation on Multidisciplinary Design Optimization of Engineering Systems. In *Meeting of the Young Researchers of LAETA*, Instituto Superior Técnico, Lisbon, Portugal, May 2022. URL `http://www.umich.edu/~mdolaboratory/pdf/2022-05-06-LAETA-plenary.pdf`.

[18] J. R. R. A. Martins and A. Ning. *Engineering Design Optimization*. Cambridge University Press, 2022. ISBN 9781108833417.

[19] N. P. Bons, X. He, C. Mader, and J. R. Martins. Multimodality in aerodynamic wing design optimization. *AIAA Journal*, 57(3):1004–1018, 2019. doi: 10.2514/1.J057294.

[20] U. Siller, C. Voß, and E. Nicke. Automated multidisciplinary optimization of a transonic axial compressor. In *47th AIAA Aerospace Sciences Meeting Including The New Horizons Forum and Aerospace Exposition*, Orlando, Florida, Jan, 2009.

[21] NASA. Aerodynamic and Structural Efficiency - Integration of Flight Control with Aircraft Multidisciplinary Design Optimization, 2023. URL `https://sbir.nasa.gov/content/aerodynamic-and-structural-efficiency-integration-flight-control-aircraft-0l`. Accessed on 03-12-2023.

[22] G. Schuhmacher, F. Daoud, Ö. Petersson, and M. Wagner. Multidisciplinary airframe design optimisation. 1:44–56, 01 2012.

[23] G. Venter and J. Sobieszczanski-Sobieski. Multidisciplinary optimization of a transport aircraft wing using particle swarm optimization. *Structural and Multidisciplinary Optimization*, 26(2):121–131, 2004. doi: 10.1007/s00158-003-0318-3.

[24] N. P. Bons, X. He, C. A. Mader, and J. R. R. A. Martins. Multimodality in Aerodynamic Wing Design Optimization. *35th AIAA Applied Aerodynamics Conference*, 2017. doi: 10.2514/6.2017-3753.

[25] N. Wu, C. A. Mader, and J. R. R. A. Martins. A gradient-based sequential multifidelity approach to multidisciplinary design optimization. *Structural and Multidisciplinary Optimization*, 65:131, 2022. doi: 10.1007/s00158-022-03204-1.

[26] J. R. R. A. Martins, T. Brooks, J. Gray, P. He, J. Hwang, J. Jasa, G. Kenway, G. Kennedy, Z. Lyu, C. Mader, N. Secco, and A. Yildirim. Multidisciplinary Design Optimization of Engineering Systems, 2022. URL `http://www.umich.edu/~mdolaboratory/pdf/2022-05-06-LAETA-plenary.pdf`.

[27] P. He, C. A. Mader, J. R. R. A. Martins, and K. J. Maki. Dafoam: An open-source adjoint framework for multidisciplinary design optimization with openfoam. *AIAA Journal*, 58(3):1304–1319, 2020. doi: 10.2514/1.J058853.

[28] Z. Lyu, Z. Xu, and J. Martins. Benchmarking optimization algorithms for wing aerodynamic design optimization. In *Proceedings of the 8th International Conference on Computational Fluid Dynamics, Chengdu, Sichuan, China*, jul 2014.

[29] A. El Ibrahim, S. A. Karim, and Gov. Aero structural optimization for sailplane wing in pre-liminary design. *Journal of Advances in Technology and Engineering Research (JATER)*, 4(1):37–47, 2018.

[30] F. Duddeck. Multidisciplinary optimization of car bodies. *Structural and Multidisciplinary Optimization*, 35:375–389, 2008. doi: 10.1007/s00158-007-0130-6.

[31] X. G. Song, L. Wang, S. H. Baek, and Y. C. Park. Multidisciplinary optimization of a butterfly valve. *ISA Transactions*, 48, 2009. doi: 10.1016/j.isatra.2009.01.009.

[32] R. Perez, H. Liu, and K. Behdinan. *Evaluation of Multidisciplinary Optimization Approaches for Aircraft Conceptual Design*. New York, USA, Sept. 2004. doi: 10.2514/6.2004-4537.

[33] A. C. Gray and J. R. Martins. Geometrically nonlinear high-fidelity aerostructural optimization for highly flexible wings. In *AIAA Scitech 2021 Forum*, page 0283, VIRTUAL EVENT, Jan. 2021.

[34] M. Zimmnau, F. Schültke, and E. Stumpf. UNICADO: multidisciplinary analysis in conceptual aircraft design. *CEAS Aeronautical Journal*, 14:75–89, 2023. doi: 10.1007/s13272-022-00620-3.

[35] A. C. Gray. Geometrically Nonlinear High Fidelity Aerostructural Optimisation for Highly Flexible Wings. Master's thesis, Delft University of Technology, The Netherlands, 2023.

[36] J. Jasa, J. Hwang, and J. Martins. Open-source coupled aerostructural optimization using python. *Structural and Multidisciplinary Optimization*, 57:1815–1827, Feb 2018. doi: 10.1007/s00158-018-1912-8.

[37] N. Bons, J. R. R. A. Martins, F. Odaguil, and A. P. C. Cuco. Aerostructural wing optimization of a regional jet considering mission fuel burn. *ASME Open Journal of Engineering*, 2022. doi: 10.1115/1.4055630.

[38] G. K. W. Kenway, G. J. Kennedy, and J. R. R. A. Martins. Scalable parallel approach for high-fidelity steady-state aeroelastic analysis and adjoint derivative computations. *AIAA Journal*, 52(5): 935–951, 2014. doi: 10.2514/6.2019-1702.

[39] S. Brown. Displacement Extrapolation for CFD+CSM Aeroelastic Analysis. 1997. doi: 10.2514/6.1997-1090.

[40] G. J. Kennedy and J. R. Martins. A parallel finite-element framework for large-scale gradient-based design optimization of high-performance structures. *Finite Elements in Analysis and Design*, 87: 56–73, 2014. ISSN 0168-874X. doi: 10.1016/j.finel.2014.04.011.

[41] G. Kennedy and J. Martins. Parallel solution methods for aerostructural analysis and design optimization. In *13th AIAA/ISSMO Multidisciplinary Analysis Optimization Conference*, Fort Worth, Texas, September 2010. AIAA-2010-9308.

[42] G. P. Guruswamy. A review of numerical fluids/structures interface methods for computations using high-fidelity equations. *Computers & Structures*, 80(1):31–41, 2002. doi: 10.1016/S0045-7949(01)00164-X.

[43] N. Secco, G. Kenway, P. He, C. Mader, and J. Martins. Efficient Mesh Generation and Deformation for Aerodynamic Shape Optimization. *AIAA Journal*, 2020. doi: 10.2514/1.J059491.

[44] E. Luke, E. Collins, and E. Blades. A fast mesh deformation method using explicit interpolation. *Journal of Computational Physics*, 231(2):586–601, 2012. doi: 10.1016/j.jcp.2011.09.021.

[45] S. Batay, A. Baidullayeva, Y. Zhao, D. Wei, A. Baigarina, E. Sarsenov, and Y. Shabdan. Aerostructural design optimization of wind turbine blades. *Processes*, 12(1):22, 2024. doi: 10.3390/pr12010022.

[46] J. Park, B. G. Knight, Y. Liao, M. Mangano, B. Pacini, K. J. Maki, J. R. R. A. Martins, J. Sun, and Y. Pan. CFD-based design optimization of ducted hydrokinetic turbines. *Scientific Reports*, 13(1): 17968, October 2023. doi: 10.1038/s41598-023-43724-4.

[47] J. R. Martins, R. J. Alonso, and J. J. Reuther. A coupled-adjoint sensitivity analysis method for high-fidelity aero-structural design. *Optimization and Engineering*, 6:33–62, 2005. doi: 10.1023/B:OPTE.0000048536.47956.62.

[48] J. R. R. A. Martins and G. Kennedy. Enabling large-scale multidisciplinary design optimization through adjoint sensitivity analysis. *Structural and Multidisciplinary Optimization*, 64(5):2959–2974, November 2021. ISSN 1615-1488. doi: 10.1007/s00158-021-03067-y.

[49] D. C. Wilcox. *Turbulence Modeling for CFD*. DCW Industries, La Canada, CA, 3 edition, 2006. ISBN 1928729088, 9781928729082.

[50] R. J. David Corson and F. Shakib. Industrial application of rans modelling: capabilities and needs. *International Journal of Computational Fluid Dynamics*, 23(4):337–347, 2009. doi: 10.1080/10618560902776810.

[51] Z. Lyu, G. K. Kenway, and J. R. R. A. Martins. RANS-based aerodynamic shape optimization investigations of the common research model wing. In *52nd Aerospace Sciences Meeting*, Oct .

[52] MDO Lab of University of Michigan. ADFlow Options. URL `https://mdolab-adflow.readthedocs-hosted.com/en/latest/options.html`. Accessed: 2024-04-03.

[53] G. K. W. Kenway, C. A. Mader, P. He, and J. R. R. A. Martins. Effective Adjoint Approaches for Computational Fluid Dynamics. *Progress in Aerospace Sciences*, 110:100542, 2019. ISSN 0376-0421. doi: 10.1016/j.paerosci.2019.05.002.

[54] S. M. Mousavi, N. SHAFIEI, and A. DADVAND. Numerical simulation of subsonic turbulent flow over NACA0012 airfoil: Evaluation of turbulence models. *Sigma Journal of Engineering and Natural Sciences*, 35(1):133–155, March 2017.

[55] P. Spalart and S. Allmaras. A one-equation turbulence model for aerodynamic flows. In *30th Aerospace Sciences Meeting and Exhibit*. American Institute of Aeronautics and Astronautics, Jan 1992. doi: 10.2514/6.1992-439.

[56] O. Tong. Verification and Validation of the Spalart-Allmaras Turbulence Model for Strand Grids. Master's thesis, Utah State University, USA, 2013.

[57] MDO Lab of University of Michigan. MACH-Aero Documentation, 2023. URL `https://mdolab-mach-aero.readthedocs-hosted.com/en/latest`. Accessed: 2024-04-03.

[58] MDO Lab of University of Michigan. PyGeo Documentation, 2023. URL `https://mdolab-pygeo.readthedocs-hosted.com/en/latest/index.html`.

[59] L. Eça, F. Pereira, and G.Vaz. Viscous flow simulations at high reynolds numbers without wall functions: Is $y+ \approx 1$ enough for the near-wall cells? *Computers & Fluids*, 170:157–175, 2018. doi: 10.1016/j.compfluid.2018.04.035.

[60] C. A. Mader, G. K. W. Kenway, A. Yildirim, and J. R. R. A. Martins. Adflow: An open-source computational fluid dynamics solver for aerodynamic and multidisciplinary optimization. *Journal of Aerospace Information Systems*, 17(9):508–527, 2020. doi: 10.2514/1.I010796.

[61] MDO Lab of University of Michigan. ADFlow Documentation, 2024. URL `https://mdolab-adflow.readthedocs-hosted.com/en/latest/index.html`. Accessed: 2024-04-03.

[62] M. Cavcar. The international standard atmosphere (ISA). *Anadolu University, Turkey*, 2000.

[63] S. Seraj, A. Yildirim, J. Anibal, and J. Martins. Improving the performance of a compressible rans solver for low and high mach number flows. In *Eleventh International Conference on Computational Fluid Dynamics (ICCFD11)*, Maui, HI, USA, July 2022. ICCFD11-2022-1702.

[64] Aerodynamic design optimization: Challenges and perspectives. *Computers and Fluids*, 239: 105391, 2022. doi: 10.1016/j.compfluid.2022.105391.

[65] T. W. Sederberg and S. R.Parry. *Free-Form Deformation of Solid Geometric Models*. Association for Computing Machinery, New York, NY, USA, 1986. ISBN 0897911962. doi: 10.1145/15922.15903.

[66] E. Wu, G. Kenway, C. A. Mader, J. Jasa, and J. R. R. A. Martins. pyoptsparse: A python framework for large-scale constrained nonlinear optimization of sparse systems. *Journal of Open Source Software*, 5(54):2564, 2020. doi: 10.21105/joss.02564.

[67] G. Kenway, G. Kennedy, and J. Martins. In *13th AIAA/ISSMO Multidisciplinary Analysis Optimization Conference*, Fort Worth, Texas, 2010. American Institute of Aeronautics and Astronautics. doi: 10.2514/6.2010-9231.

[68] J. Fish and T. Belytschko. *A First Course in Finite Elements*. John Wiley & Sons, 2007. ISBN 978-0-470-03580-1.

[69] G. Kanesan, S. Mansor, and A. Abdul-Latif. Validation of UAV wing structural model for finite element analysis. *Jurnal Teknologi (Sciences & Engineering)*, 71(2), 2014. doi: 10.11113/jt.v71.3710.

[70] J. N. Reddy. *Mechanics of Laminated Composite Plates and Shells: Theory and Analysis*. CRC Press, 2003. ISBN 0-5493-1592-1.

[71] P. D. Mangalgiri. Composite materials for aerospace applications. *Bulletin of Materials Science*, 22 (3):657–664, 1999. doi: 10.1007/BF02749982.

[72] Jansons, V. Kulakov, A. Aniskevich, and Lagzdiņš. Structural composites from aerospace to civil engineering applications. *Innovations and Technologies News*, 17:3–12, jan 2012.

[73] D. R. Askeland, P. P. Fulay, and W. J. Wright. *The Science and Engineering of Materials*. Cengage Learning, 6th edition, 2010. ISBN 9780495296027.

[74] K. Ali, s. IJsselmuiden, M. Abdalla, and Z. Gürdal. Design of variable stiffness panels for maximum strength using lamination parameters. *Composites Part B Engineering*, 42(3):546–552, 2011. doi: 10.1016/j.compositesb.2010.11.005.

[75] S.-C. Han, K.-D. Kim, and W. Kanok-Nukulchai. An element-based 9-node resultant shell element for large deformation analysis of laminated composite plates and shells. *Structural Engineering and Mechanics*, 2004. doi: 10.12989/sem.2004.18.6.807.

[76] R. Gameniro. Aero-Structural Optimization of Sailplane Wings, school = Portuguese Air Force Academy, year = Portugal, 2011, month = Oct. Master's thesis.

[77] T. H. Megson. *Aircraft Structures for Engineering Students*. Butterworth-Heinemann, 6 edition, 2011. ISBN 978-0-75066-7395.

[78] Y. Feng, H. Qiu, Y. Gao, H. Zheng, and J. Tan. Creative design for sandwich structures: A review. *International Journal of Advanced Robotic Systems*, 17(3), 2020. doi: 10.1177/1729881420921327.

[79] N. Bons and J. Martins. Aerostructural wing design exploration with multidisciplinary design optimization. In *AIAA Scitech 2020 Forum*, 01 2020. doi: 10.2514/6.2020-0544.